Available online at www.sciencedirect.com
SCIENCE DIRECT®
Physics Reports 400 (2004) 149–208
PHYSICS REPORTS
www.elsevier.com/locate/physrep

Mixed-valence manganites: fundamentals and main properties

Lev P. Gor'kov[a,b], Vladimir Z. Kresin[c,*]

[a] *National High Magnetic Field Laboratory, Tallahassee, FL 32310, USA*
[b] *L. Landau Institute for Theoretical Physics, Russian Academy of Sciences, 117334 Moscow, Russia*
[c] *Lawrence Berkeley Laboratory, University of California, Berkeley, CA 94720, USA*

Accepted 4 August 2004
editor: A.A. Maradudin
Available online 25 September 2004

Abstract

The study of manganites has been undergoing intensive development, especially following the discovery of colossal magnetoresistance (CMR). The most fundamental property of these materials is a strong correlation between their transport and magnetic properties. A transition to the ferromagnetic (and metallic) state occurs at a finite doping level and represents a special type of transition which should be described in terms of percolation theory. The same applies for the transition at the Curie temperature. As a result of the percolation theory approach, the view of these materials, both above and below the transition point, is that of inhomogeneous media consisting of tiny islands of interweaving sub-phases. These basic ideas have been now verified experimentally by neutron data, X-ray analysis, Mössbauer spectroscopy, heat capacity and magnetization measurements, etc. The phase diagram as a function of doping displays a peculiar electron-hole asymmetry; this asymmetry as well as other features (e.g., the optical properties) can be explained in the framework of a generalized two-band picture. We trace how the ground state evolves with doping and give a self-consistent analysis of various thermodynamic, optical and transport properties of metallic manganites, isotope effect, etc. It is predicted that giant oscillations in the Josephson current of a S–AFM–S junction will occur as a function of weak external magnetic fields. The contact phenomena are also described.

PACS: 75.30.Vn; 61.72.Ww; 71.30.+h

Keywords: Manganites; Percolation; Doping phases

* Corresponding author.
E-mail address: vzkresin@lbl.gov (V.Z. Kresin).

0370-1573/$ - see front matter © 2004 Elsevier B.V. All rights reserved.
doi:10.1016/j.physrep.2004.08.003

Contents

1. Introduction. A little history

This review article is concerned with the properties of the so-called manganites. This family of materials is named after the manganese ion which is a key ingredient of the compounds. Their chemical composition is $A_{1-x}R_xMnO_3$; usually A ≡ La, Pr, Nd and R ≡ Sr, Ca, Ba. These materials were first described in 1950 by Jonner and van Santen. Unlike in the usual ferromagnetics, the transition of manganites to ferromagnetic state (at $T = T_C$, T_C is a Curie temperature) takes place at finite "doping", $x \neq 0$, and is accompanied by a drastic increase in conductivity. This transition from an insulating to a metallic and magnetic state is one of the most remarkable fundamental features of these materials.

One year later, Zener (1951) explained this unusual correlation between magnetism and transport properties by introducing a novel concept, so-called "double exchange" mechanism (DE). Zener's pioneering work was followed by more detailed theoretical studies by Anderson and Hasegawa (1955) and de Gennes (1960).

Despite some early progress, a number of fundamental questions had remained unanswered. A revival of interest in the manganites and their properties came about after the remarkable discovery of the colossal magnetoresistance effect (CMR) by Jin et al. (1994). The very name of the phenomenon originates from the observation of a thousand fold (!) change in the resistivity of the La–Ca–Mn–O films near $T = 77\,K$ in the presence of applied magnetic field, $H \approx 5\,T$.

It is worth mentioning that the discovery of CMR in the magnetic oxides (manganites) was preceded by the discovery of the high temperature superconductivity in the cooper oxides (cuprates) by Bednorz and Mueller (1986). Despite of the obvious difference in the two phenomena (superconductivity vs ferromagnetism), there is some analogy between the two classes of materials. Both classes are doped oxides. The parent (undoped) compounds (e.g., the cuprate $LaCuO_4$ or the manganite, $LaMnO_3$) are antiferromagnetic insulators. It is "doping" that leads to the insulator-metal transition for both systems. Of course, there are profound differences between these compounds, but discovery and the following intensive study of the high T_C cuprates was a factor, very beneficial for the progress in understanding of manganites. It is also worth noting that the discovery of the CMR-effect was made possible with the use of high quality thin films. The preparation of such films (von Helmholt et al., 1993; Chahara et al., 1993) was based on a method developed for high temperature superconducting oxides.

This paper is not a comprehensive review describing all aspects of physics of manganites. Since the discovery of manganites, in 1950, there has been about 3000 papers published on the subject. The field is broad and remains very active (see, e.g., review by Coey et al., 1999). We focus here on some fundamentals related to dynamics of doping and transitions from insulating to metallic phases, or between various metallic structures. Therefore, in the discussion below we concentrate mainly on the low temperature properties and on the nature of the ground state. We describe also the properties of the metallic ferromagnetic phase. Because of the CMR phenomenon, this phase has undergone a most intensive experimental study.

To conclude these introductory remarks, in that follows, we keep in mind mostly the composition $La_{1-x}Sr_xMnO_3$ where the basic physics is most transparent. The reason for that will be discussed later. Here we just state the fact that of all compositions this one gives the better approximation to the cubic symmetry.

As was noted above, the intensive research in the area of magnetic oxides continues, and we formulate some open questions which will be, hopefully, resolved in the near future.

2. Electronic structure and doping: qualitative picture

2.1. Structure

Let us start from an undoped (parent) compound, $LaMnO_3$. It has a perovskite structure. The ideal case, cubic perovskite structure (Fig. 1) is a convenient starting point for the analysis (see, e.g., Coey et al., 1999). The Mn^{3+} ions are located at the corner, and the La ion at the center of the unit cell. In reality, such structure is distorted (a detailed description see Pickett and Singh (1996), Coey et al. (1999)). The system may undergo structural transitions accompanied by lattice distortions. If we focus on the Mn^{3+} ion, it is important to remember that each such ion is caged by the O^{2-} octahedron (Fig. 2); locally this forms MnO_6 complex with the Mn ion in the symmetric central position surrounded by six light oxygen ions. The arrows (Fig. 2) describe one of the lattice modes.

As was noted above, the $LaMnO_3$ crystal contains Mn^{3+} ions. Such valence state of Mn is determined by the simple neutrality count, since La ion has "+3" valence state, and each oxygen ion is in the O^{2-} valence state.

Recall that electrons of a free Mn atom form the incomplete d-shell $(\ldots)3d^5 4s^2$; $(\ldots) \equiv 1s^2 2s^2 2p^6 3s^2 3p^6$ (see, e.g., Landau and Lifshitz, 1977). Therefore, the Mn^{3+} ion, $(\ldots)\ 3d^4$, contains four d-electrons.

The five-fold orbital degeneracy is split by the cubic environment into two terms, t_{2g} and e_{2g}. The t_{2g}-level contains three electrons that form the so-called "t-core". The last d-electron (e_{2g}-electron) is well separated in energy and forms a loosely bound state (see Fig. 3). This e_{2g} electron plays a key role in conducting and other properties of manganites (see below) as well as in determining its magnetic order. The analysis of its behavior in the lattice becomes then a major subject of the microscopic theory. The Hund's rule demands that the three d-electrons forming the "t-core" have the same spin-orientation; as a result, the localized "t-core" has the total spin $S = 3/2$. The e_{2g} electron is also affected by the same strong Hund's interaction. Therefore, its spin must be polarized along the same direction as for the t-core.

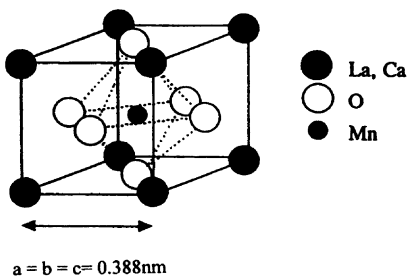

Fig. 1. Parent compound $LaMnO_3$; unit cell.

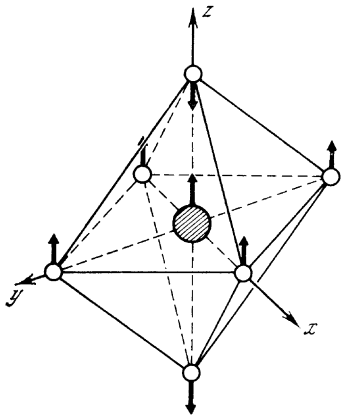

Fig. 2. MnO_6 octahedron.

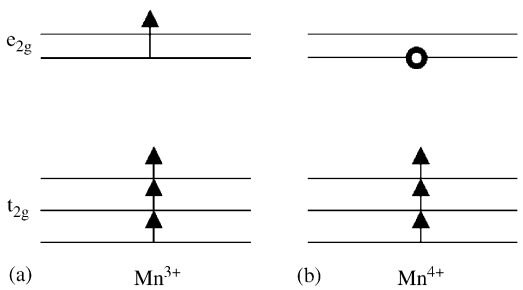

Fig. 3. (a) d-shell of the Mn^{3+}; total spin of the t-core is $S = 3/2$; e_{2g} degenerate level is splitted for clarity; (b) Mn^{4+} ion; o-hole; the $La^{3+} \rightarrow Sr^{2+}$ substitution leads to the $Mn^{3+} \rightarrow Mn^{4+}$ transition.

It is very essential also that the e_{2g}-term is a double degenerate one. As a result, we meet with the situation in which the well-known Jahn–Teller effect becomes an important factor that may lead to a lattice instability.

2.2. Doping

We described above the basic structure of the parent compound $LaMnO_3$. So far we have been focused on the structure of the unit cell. Experimentally $LaMnO_3$ is an insulator and its transition to the conducting state is provided by doping. The doping is realized through a chemical substitution, e.g. $La^{3+} \rightarrow Sr^{2+}$, that is, by placing a divalent ion into the local La^{3+} position. As was mentioned above, in what follows we consider the Sr-doping (unless it is stated otherwise). Reason for this choice is given below, Section 6.3. The substitution $La^{3+} \rightarrow Sr^{2+}$ leads to the change in manganese-ion valence: $Mn^{3+} \rightarrow Mn^{4+}$. The four-valent Mn ion loses its e_{2g} electron (Fig. 3). The missing electron can be described as a creation of a hole. At doping the Sr^{2+} ion goes into the center of the cubic cell (cf. Fig. 1). As to the hole itself, it is spread over the unit cell, being shared by eight Mn ions.

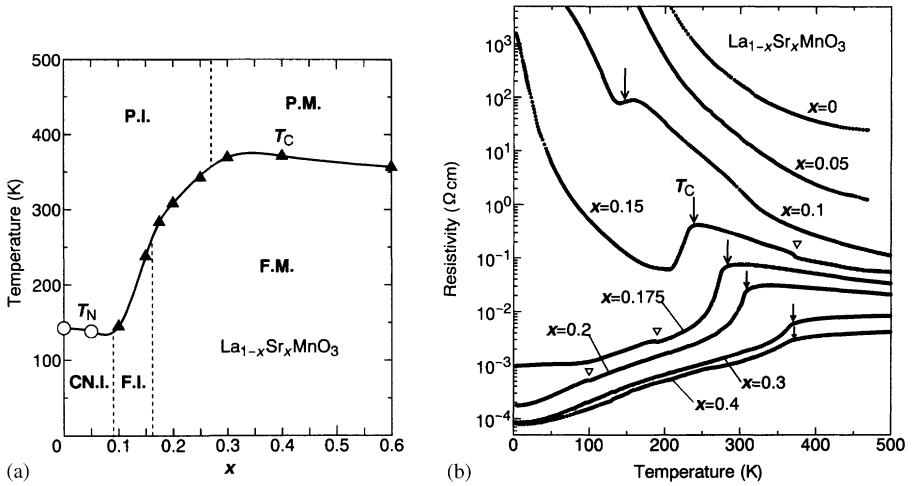

Fig. 4. Phases of manganites ($La_{1-x}Sr_xMnO_3$): (a) Phase diagram: T_N—Neel's temperature, FM—ferromagnetic metal, AI—antiferromagnetic insulator (A-phase), FI—ferromagnetic insulator, PI—paramagnetic insulator, PM—disordered paramagnetic with large resistance; (b) evolution of the dependence $R(T)$ with doping (Urishibara et al., 1995).

As a result, one obtains a crystal $La_{1-x}Sr_xMnO_3$, where a number of La centers are randomly substituted by the Sr-ions. Even in the presence of some holes, the crystal, at first, continues to behave as an insulator. In other words, each hole remains being localized on the scale of at least one unit cell. In this concentration range localization corresponds to formation of local polarons. Such insulating state is preserved with an increase in doping up to some critical value $x = x_c \approx 0.16$–0.17.

At $x = x_c$ the material makes a transition into the conducting (metallic) state (see, e.g., Urushibara et al., 1995, and Fig. 4) which persists with further doping up to $x \approx 0.5$–0.6, depending on the chosen composition.

It is remarkable that the transition at $x = x_c$ is also accompanied by appearance of the ferromagnetic state. The correlation between conductivity and magnetism is the fundamental feature of manganites, and we address this problem below. Note that the conductivity of the best samples of the Sr-doped films at low T is of order $\sigma = 10^4$–$10^5\,\Omega^{-1}\,\mathrm{cm}^{-1}$, that is, we are now dealing with a typical metallic regime.

So far, we have been concentrated on manganites in the low temperature region and evolution of their properties with doping. Take now the sample in the metallic ferromagnetic state (FM) with a fixed carrier concentration, e.g. $x = 0.3$, and then increase the temperature. Such FM state persists up to the Curie temperature $T_C \cong 170\,\mathrm{K}$. Above this temperature the compound makes the transition into paramagnetic state with much higher resistivity. Once again, one sees that there is a correlation in electronic property that manifests itself in an almost simultaneous change (at $T = T_C$) in both, conductivity and magnetization.

2.3. Magnetic order

We shall not dwell here upon the crystallographic changes in manganites. Most interesting low temperature phases changes, as a matter of fact, often involve both lattice and magnetism. The type of magnetic structure, however, is foremost determined by the doping level. The parent compound, $LaMnO_3$, belongs to the so-called antiferromagnetic insulating phase (AI). Distracting for a moment from peculiarities

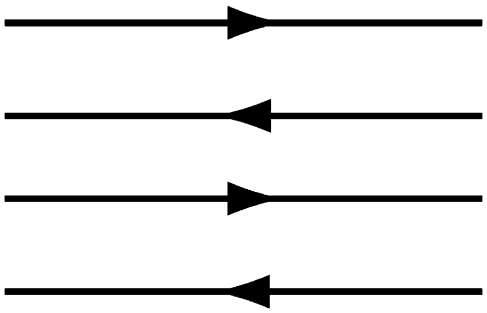

Fig. 5. A-structure.

of the O-octahedra arrangement, the antiferromagnetism in the AI-phase bears the layered character (Fig. 5). In other words, the ferromagnetic ordering in layers is combined with an antiferromagnetic order in the direction perpendicular to the layers. The Neel temperature (see Fig. 4a) for this antiferromagnetic phase is $T_N \cong 150$ K which is relatively low. We will discuss these unusual properties in more details later (see Section 6).

As was noted above, the doping leads eventually to an appearance of the 3D ferromagnetic (F) state (for $x \geqslant 0.16$; the underlying lattice also changes slightly). This state persists up to $x \approx 0.5$ for $(LaSr)MnO_3$ and then the crystal while continuing to be in the metallic state, can change its magnetic structure, which becomes *metallic* A-state. The magnetic order in this state is similar to the one of the parent (underdoped) compound (Fig. 5), but it has a metallic conductivity. Such compound is a natural spin valve system. Indeed, as is known, the "giant" magnetoresistance effect (GMR) has been observed by using a special artificial multilayer structure. Contrary to it, the metallic manganites with magnetic A-structure are natural 3D systems which display the GMR phenomenon. In addition, this material can be used for making the new type of the Josephson junction (SAS). We will discuss all these properties below (Sections 6.1 and 8.2).

2.4. Double exchange mechanism

Here we qualitatively discuss the nature of the observed ferromagnetic spin alignment. As was noted above, the concept, so-called "double exchange" (DE) mechanism was introduced by Zener (1951) almost immediately after the discovery of manganites.

If one of the Mn^{3+} ions becomes ($Mn^{3+} \rightarrow Mn^{4+}$) four-valent (as a result of the doping, that is, e.g., the $La^{3+} \rightarrow Sr^{2+}$ substitution), a hole appears on this site. It allows for another e_{2g}-electron localized initially at the neighboring Mn^{3+} ions to jump on the new vacant place (such a hopping corresponds to the hole moving in the opposite direction). But, as was noted above, the e_{2g}-electron is spin-polarized (Fig. 3) because of the Hund's interaction with its t-core. The total spin of each t-core is equal to $S = 3/2$, but their mutual orientations on different sites were independent. Relative orientation of spins of the e_{2g}-electron and the "vacant" t-core is the crucial factor for the hopping because of the strong Hund's interaction. Indeed, imagine that the direction of the spin of the core for the Mn^{4+} ion is opposite to that one for the e_{2g} electron of the neighboring Mg^{3+} ion. Then the hopping is forbidden. At the same time such hopping as any increase in a degree of delocalization is energetically favorable. In other words, it gives a gain in

the kinetic energy, and the ground state of the ferromagnetically ordered system (all spins are polarized along one direction) lies below the paramagnetic state. As a result, the t-cores become ferromagnetically coupled, and this, in its turn, favors hopping of the e_{2g}-electrons.

This simple picture describes qualitatively the origin of the ferromagnetism in the manganites and demonstrates the direct interdependence between hopping and ferromagnetic ordering.

Namely, this correlation leads to the observed interplay between conductivity and magnetism. A quantitative analysis requires a rigorous treatment of hoping along with the Hund's interaction and will be described below (see Section 5).

It is important to emphasize that the charge transfer in the conducting ferromagnetic manganites is provided by spin-polarized electrons. Such a conductor is different from an usual metal where spins of conduction electrons have both direction. Because of such spin specifics the conducting state in manganites is called "half-metallic".

2.5. Colossal magnetoresistance (CMR)

The huge magnetoresistance effect has been observed in the ferromagnetic metallic films $La_{0.67}Ca_{0.33}MnO_3$ (Jin et al., 1994). The magnetoresistance is defined as

$$\Delta R/R_H = [R(T, H) - R(T, 0)]/R(T, H) \ . \tag{2.1}$$

The magnetoresistance has a sharp peak near $T \cong 190\,\mathrm{K}$, that is, near the Curie temperature for the Ca-doped manganites, and the change in resistivity caused by an applied magnetic field ($H \approx 5\,\mathrm{T}$) is very large, $\Delta R/R_H \approx -1.3 \times 10^3$(!).

Such a drastic change in resistivity is caused by the aforementioned correlation between magnetic ordering and conductivity and, therefore, is directly related to the double-exchange mechanism realized in manganites. Indeed, below the Curie temperature T_C conductivity has a metallic band mechanism (see below, Section 5), whereas above T_C mechanism of its conductivity bears a polaronic hopping character. The presence of an external magnetic field is a favorable factor allowing to establish ferromagnetic ordering at temperatures higher than T_C ($H = 0$). The magnetic order triggers the conductivity increase (through the double exchange mechanism), and this leads to a large resistivity change $\Delta R_H = R(T, H) - R(T, 0)$. The shift is negative, i.e., indeed, corresponds to the transition into ferromagnetic metallic state.

The presence of localized states above T_C was theoretically considered by Millis et al. (1995, 1996a, b), and by Millis (1998), and observed experimentally by X-rays and photoemission spectroscopies (Booth et al., 1998; Mannella et al., 2004).

It is interesting that the large peak in the magnetoresistance was first observed long time ago by Volger (1954) in $La_{0.8}Sr_{0.2}MnO_3$. A drastic enhancement of the effect was achieved by using thin films and proper composition (Jin et al., 1994).

The "colossal" magnetoresistance effect (CMR) greatly exceeds in its value the so-called "giant" magnetoresistance effect (GMR), see, e.g., review by Parkin (1995). The GMR effect is observed, mainly, in artificial multilayers systems with alternating magnetic structure and is used in many applications. It reaches a value $\Delta R_H/R_H \cong 50\%$. The scale of the CMR phenomenon is much larger. The nature of the CMR and GMR phenomena are entirely different. It is interesting, nevertheless, that, as mentioned above, the metallic manganite with the A-structure (say, in $La_{2-x}Sr_xMnO_3$ with $x > 0.5$) forms a natural GMR system and this might lead to the GMR effect in manganites. We will discuss this case below (see, Section 5).

We enumerated above qualitatively some fundamentals in manganites. Almost each feature mentioned in this section, of course, deserves a more detailed theoretical discussion. We will discuss many of them in next chapters.

3. Percolation phenomena

3.1. Low doping. Transition to the ferromagnetic state at low temperatures

Substitution $La^{3+} \rightarrow Sr^{2+}$ creates a hole located inside of one unit cell. The Coulomb attraction prevent the hole from larger delocalization, namely, from a spreading through the whole lattice. An increase in doping leads to an increase in the number of such unit cells containing holes. In addition, if the Sr-substitution occurs for two or more neighboring units, a larger cluster forms covering two and more unit cells with holes delocalized along such bigger clusters. From the Zener's double-exchange mechanism we expect that spins of the Mn ions have the ferromagnetic alignment inside of each cluster (see Section 2.4).

Random character of the Sr-substitution leads to statistical (chaotic) distribution of these clusters. As a result, growth of the clusters can be treated by means of percolation theory (see, e.g., Shklovskii and Efros, 1984; Deutcher, 1987; Stuffer and Aharony, 1992).

As just noted above, increase in the doping level of the $La_{1-x}R_xMnO_3$ crystal ($R \equiv Sr, Ba, \ldots$) leads to increase in the clusters' size and their overlap. Finally, at some critical value of $x = x_c$ (percolation threshold) the system forms the so-called "infinite" cluster piercing the whole sample. In other words, at $x = x_c$ one first sees the appearance of connected islands of a *macroscopic* metallic ferromagnetic phase. As other phase transitions, the percolative insulator–metal transition in manganites can be characterized by some critical indexes (see below). This theoretical approach to the transition in manganites was first introduced and developed by the authors (Gor'kov and Kresin, 1998, 1999, 2000; see also Gor'kov, 1998; Dzero et al., 2000). At present, the metal–insulator transition in manganites is commonly analyzed as a percolation phenomenon (see, e.g., Jaime et al., 1999; Dagotto et al., 2001).

The approach based on the percolation concept implies that the system is intrinsically inhomogeneous. The inhomogeneity may manifest itself through "phase separation". The phenomenon of "phase separation" corresponds to the simultaneous existence of the mutually penetrating sub-phases. As was noted above (Section 1), the progress in theory of manganites was strongly influenced by the preceding discovery and studies of high temperature superconductivity in the cooper oxides. For instance, the concept of phase separation (coexistence of insulating and metallic sub-phases) was first suggested by Gor'kov and Sokol (1987) in relation to the high T_C superconducting oxides. The idea received further development and experimental attention in many papers (for review see, e.g., Sigmund and Mueller, 1994).

Similar phase separation occurs for the doped manganites with increase in doping. The static electronic phase separation in manganites was first analyzed by Nagaev (1994, 1996), and then by Gor'kov and Kresin (1998) and by Mori et al. (1998). A. Moreo, E. Dagotto and their collaborators used numerical simulations (Monte Carlo technique) in order to study the phase diagram and formation of clusters. The results are described by Dagotto et al. (1998), Yunoki et al. (1998a, b), Yunoki and Moreo (1998), Burgy et al. (2001) and in the reviews by Moreo et al. (1999) and by Dagotto et al. (2001).

The percolation can be interpreted as a more subtle case of phase separation where "phases" coexist on a mesoscopic scale or even as interweaving clusters. Macroscopic properties are determined, mainly, by one sub-phase, where there are also inclusions of another phase. For example, properties of manganites at $x < x_c$ are dominated by the antiferromagnetic insulating phase ("insulating matrix") in which "metallic" clusters start to form at $x \neq 0$. The amount of the metallic phase is growing as $x \to x_c$.

At $x > x_c$ metallic paths are formed and gradually become more and more dominant, but the insulating regions are also present.

3.2. Percolation threshold

Experimentally, the metallic behavior of a compound at low T sets in at the critical value $x = x_c \approx 0.16$ (Urushibara et al., 1995). At cooling the temperature, at which conductivity sharply increases, almost coincides with the onset of the ferromagnetism, especially in good quality samples. For example, for the $La_{0.67}Ca_{0.33}MnO_3$ sample ($T_C = 274\,K$) studied by Heffner et al. (1996) these temperatures coincide to within 1 K (see also Schiffer et al., 1995 and review by Coey, 1999). Such closeness of the onset temperatures is a strong indicator in favor of the double-exchange mechanism.

Let us discuss the threshold value $x_c \approx 0.16$. Recall that material may be prepared by various methods but always at high temperatures. As a result, positions of atom R, which substitute for a parent atom, are completely random. Divalent atom R, locally creates a "hole" localized on adjacent Mn sites. The Coulomb forces in the dielectric phase keep the "hole" close to the negative charge at R^-. When the concentration is small, average distances between R-ions are large, the holes remain isolated forming trapped states (polarons), see Section 7.5.

Consider the concentration at which the nearest neighbors R-atoms start, in accordance with percolation picture, to form infinite clusters piercing the whole crystal. More often than not one attacks percolation in one of two discrete mathematical models on the cubic lattice: the "site" and "bonds" problems. Picture of a hole localized at single center would correspond to the so-called "site" problem (contrary to the "bond" problem) of the percolation theory. The critical concentration x_c^s for the "site" problem depends on the type of lattice and for simple cubic structure is equal $x_c = 0.31$ (see, e.g., Shklovskii and Efros, 1984). However, this is not our case. While ionic substitution takes place at the center of the cubic unit, the formed hole is spread over several Mn sites around the R ion. At the same time, the charge transfer due to forming the larger cluster occurs only along Mn–O–Mn bonds. Hence, the picture of a critical cluster, constructed from the R^- ions is not correct; such initial (nucleating) cluster is not a point-like formation and already has a finite size ("thickness"). The size is even bigger at large enough dielectric constant that would weaken the Coulomb attraction to the R^- ion. According to numerical calculations (Scher and Zallen, 1970), this circumstance (i.e., involvement of a scale of a few lattice constants into the percolation problem) strongly decreases the value of critical concentration for percolation. It is interesting that now the critical value x_c depends only on the spatial dimension and appears to be invariant for all lattices. For the 3D case (see, e.g., Shklovskii and Efros, 1984)

$$x_c^{3D} \approx 0.16\ . \tag{3.1}$$

The "site" problem corrected by the finite hole radius, becomes similar to the "continuum" percolation. As to the continuous limit, it is only natural that independent numerical studies (Shklovskii and Efros, 1984) lead to close values for x_c. Therefore, the invariant of the percolation theory $x_c \approx 0.16$ describes the threshold, above which the formation of an infinite cluster first takes place. In its manifestation, it

corresponds to appearance of a new macroscopic state, that is, in our case, to the transition into a metallic ferromagnetic state.

It is remarkable, that the experimentally observed value of the critical concentration $x_c \approx 0.16$ corresponds, indeed, with a good accuracy, to the value obtained in framework of the percolation theory (see, e.g., Urushibara et al., 1995).

The measurements by Urushibara (1995) were performed for $La_{1-x}Sr_xMnO_3$. The analysis of the phase diagram for $La_{1-x}Ca_xMnO_3$ (Schiffer et al., 1995), see also a review (Coey et al., 1999), shows that the values of the critical concentration for different manganites are close to value (3.1).

Note, that for the three-dimensional problem there is a concentration interval in which percolation (coexistence of infinite piercing clusters) may take place simultaneously for each of two phases (insulating and conducting, for instance) though taking into account effects akin to the surface tension at the boundary between two spatially coexisting phases may impose limitations on relative thickness of one of the phases. The mixture of "two" phases, depending on the dopant concentration, x, actually looks as interweaved tiny "islands" and "layers" of different phases. Well below and well above the threshold concentration x_c, one may imagine each of the corresponding phases as a bulk formation into which the second phase is sparsely embedded.

Therefore, the percolative description means the situation when one phase manifests itself as tiny inclusions ("islands") embedded into another, the dominant macroscopic phase. Here lies difference between the percolative picture and that of the macroscopic electronic phase separation.

3.3. Large doping

The 3D metallic ferromagnetic phase of $La_{1-x}Sr_xMnO_3$ persists up to $x \cong 0.5$. Further increase in doping leads to a rather sharp transition (at low enough temperature) to the so-called metallic A-phase. This phase is also metallic, as far as the low temperature conductivity is concerned (similar to the FM phase at smaller x) but it has a different magnetic structure (cf. above, Section 3.1). Namely, it consists of metallic ferromagnetic layers with the magnetization orientation alternating in the direction perpendicular to the layers.

This metallic A-phase persists up to $x \cong 0.55$. For the compound with such a large concentration it might be more convenient to consider first the opposite end of the phase diagram, $x = 1$. The limit $x = 1$ described the compound $RMnO_3$ (e.g. $SrMnO_3$). This material is an insulator and contains only Mn^{4+} ions. Such compound does not contain e_{2g} electrons at all. Starting from this end, one can describe the phase diagram as the result of substitutions A $\rightarrow$ R (e.g., Sr $\rightarrow$ La), that is, as the electron doped compound. The composition of the sample can be written as $La_ySr_{1-y}MnO_3$. At $y = 0.45$ (it corresponds to $x = 0.55$ in the "hole-doping" picture) there is the transition to the metallic state. Because of the antiferromagnetic ordering is along the c-direction (c-axis has chosen to be perpendicular to the layers), we start dealing with almost 2D transport (hopping in the c-direction is spin-forbidden thanks to the Zener double-exchange).

It is rather temping to interpret the metal–insulator transition at $y = 0.45$ as a percolative transition in 2D model. Indeed, as was noted in the previous section, the percolation threshold depends on dimensionality of the system; for the hole doping (3D case) $x_c \cong 0.16$. According to the percolation theory, for the 2D case (see Shklovskii and Efros, 1984) $y_c = 0.45$. This value of the invariant is in a remarkable agreement with the experimentally observed value $y_c \cong 0.45$ ($x_c^{\text{large}} \cong 0.55$) for the $La_{1-x}Sr_xMnO_3$ compound. At $x > 0.55$ the compound is in the antiferromagnetic insulating state with competitive double-exchange

and superexchange contributions. This region was described by van der Brink and Khomskii (1999) and by Dagotto et al. (2001).

3.4. Percolative behavior at high temperatures (the vicinity of CMR effect)

In the previous sections we described the evolution of the phase diagram, including the metal–insulator transitions as driven by doping at low temperatures. Let us consider the compound with a fixed level of doping. For example, the manganite with $x = 0.3$ has a well established metallic ferromagnetic state in the low temperature region. An increase in temperature leads to the transition (at $T = T_C$) to the paramagnetic and low conducting state. This transition can be also treated by means of percolation theory and one can apply the ideas similar to those described above. Indeed, the high temperature resistivity, $\rho(T > T_C)$, is very large and one may approximately take the conductivity here $\sigma(T > T_C) = \rho^{-1}(T > T_C) \cong 0$. The fast increase in $\sigma(T)$ at $T < T_C$ is then expected to correspond

$$\sigma(T < T_C) \propto (T_C - T)^{\gamma} , \tag{3.2}$$

where γ is a critical index.

The statement that the transition at T_C is also of a percolative nature implies the intrinsic inhomogeneity of the sample, i.e., the phase separation, quite similar to that was discussed earlier.

An interesting phenomenological model based on this concept was developed by Weiße et al. (2003). They suggested picture of percolating phases with some added boundary conditions (equal pressure for carriers in the metallic and insulating regions) has allowed to describe the observed transport properties more quantitatively including their strong sensitivity to an external magnetic field. With use of modeling the resistivity in the presence of percolative phase, a negative magnetoresistance near T_C was obtained.

For some manganites (e.g., $Nd_{1-x}Sr_xMnO_3$) at large $x \cong 0.5$ and above, at high temperatures one can observe a transition to the charge ordered (CO) state, see e.g., Mahendiran et al. (1999). Interesting aspect of the CO for the double manganese oxide system was studied by Prodi et al. (2004). The transition between the CO and FM states was also described by the percolation theory, see e.g., Fukumoto et al. (1999), Uehara et al. (1999). However, properties of the CO state are beyond the scope of this review, in which we restrict ourselves by low temperature region, i.e., near the ground state, and the region near the CMR transition close to T_C for the ferromagnetic metallic phase.

The term "phase separation" means that even below T_C, in the ferromagnetic metallic state inclusions of low conducting paramagnetic phase persist. Presence of such regions can be detected experimentally. We will discuss these phenomena in the next section devoted to various experimental data supporting the percolation picture.

3.5. Experimental data. Discussion

The theoretical approach based on the percolation theory has, at present, the strong experimental support. To start with, we repeat that the experimentally measured critical concentration $x_c \cong 0.16$ for the $La_{1-x}Sr_xMnO_3$ compound and a close value for other manganites is in an excellent agreement with the value predicted by the 3D percolation theory (see Eq. (3.1)). This agreement is a direct quantitative indication in favor of the percolative nature of the metal–insulator transition.

As stated above, the percolation always implies some inhomogeneity of the system. Let us consider first the low temperature region and trace in more details the doping dependence. The neutron pulsed

experiments (Louca and Egami, 1997a, b, 1999a, b; Louca et al., 1997) directly indicate the presence of such local inhomogeneities. These experiments probe the local arrangements of the oxygen octahedra. With the random disorder, one may expect that the degeneracy of the e_{2g} terms would also be lifted randomly, providing a random distribution in the local Jahn–Teller deformations of the oxygen octahedra. Meanwhile, it has been shown by Louca and Egami (1999a, b) that even at $x > x_c = 0.16$ the pair distribution function (PDF) displays the well pronounced peaks at the values of Mn–O bond which are characteristic for the elongated octahedra of the parent $LaMnO_3$. The presence of such insulating inclusions in $La_{1-x}Sr_xMnO_3$ is seen up to $x \approx 0.35$, that is, well above x_c, in the metallic region.

Local Jahn–Teller distortions have also been observed with use of extended X-rays absorption fine structure spectroscopy (EXAFS), see below. The corresponding analysis of the bond length distribution for $La_{1-x}sSr_xMnO_3$ (Mannella et al., 2004; Shibata et al., 2003) demonstrated the presence of these distortions, although with smaller amplitudes than was obtained with the PDF method.

Note also that the value of magnetization M depends on the doping level: $M \equiv M(x)$. The observed dependence is close to the simple relation $M(x) = (4 - x)\mu_B$, but it is *less* than this value (see Coey et al., 1999); this indicates that admixture of "nonmetallic" (non-ferromagnetic) phase still persists at these concentrations. This fact and the concentration range agree well with the value $x \approx 0.35$ estimated from neutron experiments (Louca and Egami, 1999). The ferromagnetic phase occupies almost the whole volume (at $x > 0.3$); $M(x)$ and $D_{\text{stiff}}(x)$ (D_{stiff} is the spin waves stiffness coefficient) slowly decrease with x (Dzero et al., 2000).

At the same time, there are data which indicate the existence of the metallic ferromagnetic regions below x_c, inside of the insulating phase. The presence of such metallic islands should manifest itself in the linear (electronic) term in the heat capacity. Indeed, according to Okuda et al. (1998), the finite value of the Sommerfeld's constant at $x < 0.16$ was observed in $La_{1-x}Sr_xMnO_3$. It would be interesting to perform more systematic measurements of heat capacity at $x < x_c$. Some peculiar a.c.-conductivity caused by presence of metallic clusters is also expected.

Interesting results on the $La_{1-x}Zn_xMnO_3$ compound were reported by Felner et al. (2000). The authors measured the magnetization and magnetic susceptibility, and observed an additional ferromagnetic signal at $T = 38\,\text{K}$ for $x = 0.05$ and 0.1. More specifically, the ferromagnetic transition was inferred directly from the field-cooled curves. Typical of such transition increase of magnetic moments was observed at $T = 38\,\text{K}$ for these two samples. At the same time the magnetization curves are smooth and flat in this temperature region for the parent ($LaMnO_3$) and metallic ($x = 0.33$) samples. The samples with $x = 0.05$ and 0.1 are in the insulating state, but these interesting results described above were explained by assuming that, in accordance with percolation picture, they contain the ferromagnetic metallic (FM) clusters. The presence of such clusters leads to an additional signal.

Take the metallic manganite at some fixed concentration, e.g., $x \approx 0.3$. As was discussed above, the transition at $T = T_C$ from low conducting high temperature state to the metallic ferromagnetic state, in turn, can be treated in the percolation terms. Therefore, one should expect to observe insulating paramagnetic inclusions below T_C. The phenomenon, indeed, has been directly demonstrated in the STM experiments at the surface of $La_{1-x}Ca_xMnO_3$ ($x \approx 0.3$) compound (Fath et al., 1999). The authors have observed a spatial variation of the local electronic properties on a submicrometer scale. The STM images were taken in magnetic fields between 0 and 9 T. The insulating regions were observed at temperatures below bulk T_C(!). The results were independent on the surface topology. With the magnetic field increase insulating regions shrink and convert into metallic ones (as they should for the double exchange mechanism), although some insulating regions survive even at fields as high as 9 T.

STM spectroscopy was used also to visualize metallic and insulating regions in the thin (~ 50 nm) $La_{0.7}Sr_{0.3}MnO_3$ films (Bekker et al., 2002). The authors measured the tunneling conductance of metallic regions as a function of temperatures. To explain the data, the comparison has been done with a resistor network, created by a numerical simulation. Experiments demonstrated explicitly development of the macroscopic current channels near T_C as expected from the percolation theory.

The transport properties (resistivity, thermoelectric coefficient) can be described, with a good accuracy, by the model (Jaime et al., 1999) that takes into account persistence of insulating phase domains inside the metallic ferromagnetic phase.

A detailed analysis of the local structure can be performed with use of the X-rays adsorption fine structure spectroscopy. The new iterative method and good standards are described by Bridges et al. (1995) and Li et al. (1995). The study of $La_{1-x}A_xMnO_3$ (A ≡ Ca, Pb) by Booth et al. (1996) as well as an analysis of $La_{1-x}Ca_xMnO_3$ (Booth et al., 1998a, b; Subias et al., 1997) and $La_{1-x}Sr_xMnO_3$ (Mannella et al., 2004) samples contain a direct evidence of disorder above T_C for manganites with concentration in the region of the metal–insulator transition. According to Booth et al. (1998a), the distortion corresponds to the Jahn–Teller degrees of freedom. The linear relation between $\ln(n_{dh})$ and magnetization M (n_{dh} is the concentration of delocalized holes) was obtained (Booth et al., 1998a, b); this relation is consistent with the resistivity data (Hundley et al., 1995). The analysis which combines X-rays and photoemission spectroscopies (Mannella et al., 2004) shows that the carrier concentration along with the JT distortions is consistent with the polaronic picture. The distortions are, in a large degree ($\approx 70\%$), removed below T_C. Nevertheless, one still can observe their presence in the metallic ferromagnetic phase. According to Booth et al. (1998b), above T_C one can observe not only localized states,but also free carriers. These results strongly support the percolation picture. Note also, that hybridization between neighboring Mn ions (Bridges et al., 2000, 2001) leads to a modification of the polaronic states and possible impact of the band effects (see below, Section 5).

In the neutron experiments high real-space-resolution diffraction method used to study $La_{1-x}Ca_xMnO_3$ compound (Billinge et al., 2000) allowed to distinguish three distinct Mn–O bond length. In the ferromagnetic phase ($x = 0.33$) at low temperatures ($T \cong 20$ K), one can see a single Mn–O bond-length distribution peak which corresponds to the bulk cubic FM phase. However, the increase in temperature leads to appearance of another peak corresponding different bonds length (e.g., Mn^{3+}–O bond that are characteristic of the insulating state) even at $T < T_C$. This observation demonstrates a spatial coexistence of the extended bulk (metallic) and embedded islands of the insulating phases.

Similar conclusions follow from the muon spin relaxation study of the same compound, $La_{1-x}Ca_xMnO_3$ (Heffner et al., 1996, 2000, 2001). Single relaxation components were determined for the parent insulating compounds $x = 0$ and 1. However, for the metallic phase it was necessary to use a "two-exponent" time analysis which is consistent with two spatially distinguishable regions with very different relaxation rates. The "fast" component corresponds to metallic phase whereas the "slow" component was ascribed to coexisting insulating phases.

Another experimental support comes from the Mössbauer spectroscopy measurements (Chechersky et al., 1999). The strong paramagnetic signal has been observed at $T > T_C$. Decrease in temperature leads at $T < T_C$ to the appearance of the strong signature of the ferromagnetic state, seen as the "six-peaks" structure in the Mössbauer signal. However, even at $T < T_C$ the paramagnetic signal persists down to $T \cong 20$ K, which is much below T_C.

Correctness of the percolation theory views may be also verified by independent measurements of conductivity $\sigma(T, x)$ and magnetization, $M(T, x)$, or $D_{stiff}(T, x)$-so-called "spin-stiffness", which

determines the spectrum of the long-wave magnons:

$$\omega(k) = D_{\text{stiff}} k^2 \tag{3.3}$$

(see also Section 5.3).

The Kirkpatrick's relation (Kirkpatrick, 1973a, b) which is well-known for percolation theory, then connects the parameters together:

$$\sigma \propto DM \tag{3.4}$$

Eq. (3.4) may be verified at x close to x_{cr} or at T near T_{C}.

Since $D \propto M$, we have $\sigma \propto M^2$. Experimentally, this relation, indeed, is in agreement with the available measurements (Ghosh et al., 1998).

The Kirkpatrick relation (3.4) is expected to be approximately correct in a continuous media regime, near T_{C}, where onset of ferromagnetism may be interpreted as the simultaneous onset of a new (metallic) mechanism for conductivity. As it was pointed out, Eq. (3.4) is satisfied rather well. This means that the onset temperatures, indeed, are very close (see above, Section 3.2). Nevertheless, one should note that this factor depends on the quality of the sample. For example, in $La_{0.8}Sr_{0.2}MnO_3$ studied by Lofland et al., 1996, the peak temperature, T_{P}, and the Curie temperature, T_{C}, although being close to each other, do not coincide ($T_{\text{P}} = 318 \pm 2\,\text{K}$ and $T_{\text{C}} = 302 \pm 2\,\text{K}$). Phenomena at T_{P} are commonly considered in the literature (Millis et al., 1996) as a crossover temperature where the regime of conductivity via the thermal hopping of polarons localized by the thermal lattice disorder cedes sharply to give way to a metallic mechanism with a short mean free path. This difference between T_{C} and T_{P} shows some smearing of the above picture, and scale of this smearing depends on the sample quality.

From the above one could convince himself that the percolative approach has a very strong experimental support and provides an adequate description of the doping process in manganites at the metal–insulator transitions in these materials.

4. Main interactions. Hamiltonian

Let us enumerate the major factors which form the basis for microscopic understanding of manganites. Qualitatively, we have already mentioned some of these factors in Section 1. Here we are going to present a more elaborate analysis. At first, we will write down the Hamiltonian that allows an adequate analysis of major properties of the materials.

The parent material, $LaMnO_3$ (see Section 1) contains Mn^{3+} ions; such an ion has four d-electrons. Recall again that the d-shell in the cubic environment is split into the triple (t_{2g}) and double (e_{2g}) degenerate terms (Fig. 3). The t_{2g}-level is fully occupied by three electrons forming together the local total spin $S = 3/2$, in accordance with the Hund's rule. The e_{2g}-level in manganites may become empty (Mn^{4+}) as a result of doping by a divalent substitution.

The e_{2g}-electron is the key player in physics of manganites. Its hopping provides both the mechanism of conductivity as well as ferromagnetism (DE mechanism). If there is one electron on the e_{2g}-level, the direction of its spin is governed by the same intra-atomic Hund's interaction as for the t_{2g}-electrons:

$$\hat{H}_H = -J_H \sum_i \hat{\sigma} \cdot S_i \ , \tag{4.1}$$

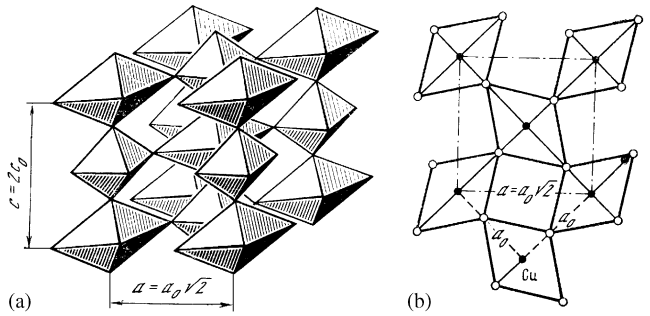

Fig. 6. JT deformation of the octahedron: (a) antiferrodistortion: 3D picture, (b) top view.

($\hat{\sigma}$ is the Pauli matrix for the e_{2g}-electron; summation is over all ionic positions). Therefore, locally spins of e_{2g} and t_{2g} electrons are ferromagnetically aligned.

The Hund's coupling is rather strong ($J_H S \approx 1$–1.5 eV) and is taken below as the largest energy scale in the theory.

As the next step we should write down the kinetic energy part of the Hamiltonian. Here it becomes essential that the e_{2g} electron finds itself in the double degenerate state. Therefore, the hopping process of an electron from a site i to its nearest neighbor $i+\delta$ in the tight-binding approximation has to be modified to account for the double degeneracy of the e_{2g}-level on each site. Hence, in the hopping Hamiltonian:

$$\hat{H}_i = \sum_{i,\delta} \hat{t}_{i,i+\delta} \ . \tag{4.2}$$

$\hat{t}_{i,i+\delta}$ becomes a two-by-two matrix. Its explicit form depends on the choice of the basis for the e_{2g}-representation (see below).

Finally, it is necessary to take into account the local Jahn–Teller (JT) term responsible for instability which is the direct consequence of the aforementioned degeneracy of the e_{2g}-term. The JT effect manifests in the spontaneous lattice distortions; the distortion serves to lift the degeneracy. On the local level we mean deformations of the oxygen octahedron (see Fig. 6) coupled with the active JT vibrational modes. The latter were introduced by Kanamori (1961) and denoted Q_2 and Q_3; their choice and the explicit form for Q_2 and Q_3 is written down below, see Section 6. The JT interaction is linear in Q_2, Q_3. A convenient "pseudospin" formalism was proposed by Kugel and Khomskii (1982), so that, the invariant form of the JT interaction is

$$H_{JT} = \sum_i g\hat{\tau}_i Q_i \ , \tag{4.3}$$

$\hat{\tau}$ is the "pseudospin" matrix. One should add however, that, because two neighboring octahedra share a common oxygen ion (along the Mn–O–Mn bond), the deformations are not independent, and speaking of the JT effect below we always mean a so-called *cooperative* Jahn–Teller effect (see, e.g., Kaplan and Vekhter, 1995), i.e., the corresponding structural change of a whole lattice.

Gathering all contributions (4.1)–(4.3) together, one can write down the total Hamiltonian as

$$\hat{H} = \sum_i \left(\sum_{i,\delta} \hat{t}_{i,i+\delta} - J_H \sigma \cdot S_i + g\hat{\tau}_i Q_i + J_{\rm el} Q_i^2 \right) . \tag{4.4}$$

The last term accounts for the "elastic" energy part of the local JT mode. The importance of the JT term was emphasized by Millis et al. (1995). They consider the high temperature region (above T_C), more specifically, where the thermally excited JT degrees of freedom move chaotically, thus tending to localize the charge carriers inside the oxygen cages. The transition to the ferromagnetic metallic state at T_C is accompanied by "turning off" the main part of this localization. Based on this picture and Hamiltonian (4.4), Millis et al. (1996a, b) calculated the magnetoresistance and their calculation reflects the essential physics of the CMR phenomenon. A detailed description of this interesting paper is beyond the scope of this paper because the main part of this review is aimed at the properties of manganites in the low temperature region, that is, close to the ground state, and their variation with composition where lattice degrees of freedom themselves may also influence its crystalline structure.

As it was mentioned above, in the described approach the largest energy scale in Hamiltonian (4.4) corresponds to the Hund's interaction ($\cong$ 1–1.5 eV). As for the hopping and the Jahn–Teller terms, they have a competitive strength, i.e., the same order of magnitude, so that $t \sim g \cong 0.1$ eV, with $t, g \ll J_H$.

The hopping term in (4.4) leads to delocalization of the e_{2g}-electron and, correspondingly, results in the band picture. The specific band approach described below (Sections 5–7) is made possible exclusively by such important features of manganites as large value of Hund's coupling constant J_H, and the double degeneracy of the e_{2g}-orbitals also plays an important role for manganites' properties. We call it below as the two-band scenario.

The fact that the band approach can capture the main physics of manganites is far from being obvious. Another approach often uses explicitly the generalized local Hubbard model to account for strong on-site electron–electron interactions. Actually, instead of a direct Hubbard on-site interaction $U > 0$ which hinders the double occupancy of a single Mn site, one may consider the local Jahn–Teller effect as alternative way to describe the same physics. Indeed, a single electron positioned on the degenerate e_g-orbital on the Mn site will cause a local lattice distortion, reducing the energy of the system. On the other hand *two* electrons on the same site *do not* lead to Jahn–Teller instability and the Jahn–Teller energy gain does not realize itself. Therefore, locally it is always more favorable energetically to have a single electron on a given site. We should also stress the large values of the Hund's coupling ($J_H \cong$ 1–1.5 eV), that is responsible for the spin alignment of all electrons on a given Mn site.

A tendency to the Jahn–Teller effect causes strong electron-phonon interaction which is thought to be the reason for occurrence of different structural transitions in manganites. The latter, in turn, may affect their electronic properties.

Based on Hamiltonian (4.4) one can find the electron energy spectrum and, afterwards, study numerous electronic properties of the system. From this point of view, the ferromagnetic metallic phase (FM) represents the simplest case. There are no collective Jahn–Teller effects for this phase that would lead to static distortions that could strongly deviate lattice from its almost cubic symmetry. The impact of the JT term on the energy spectrum for the FM phase will be omitted. The Hund's term can be easily incorporated in calculations of the energy spectrum for the ferromagnetic case. The treatment is more complicated for the antiferromagnetic metallic phase (see Section 6) and, especially, for the insulating state (Section 7). At first, we consider the electron spectrum and properties of the FM state. The analysis

of this state is important for its own sake, not to mention that it is the ferromagnetic metallic part of the manganites' phase diagram where the CMR phenomenon takes place.

5. Ferromagnetic metallic state

5.1. Two-band spectrum

Let us find out the single electron spectrum of the 3D metallic ferromagnetic manganite as it follows from the Hamiltonian (4.4); the results apply at $0.16 \leqslant x \leqslant 0.5$ (Dzero et al., 2000). We use below the tight binding approximation, assuming that the overlap of electronic wave functions for neighboring Mn ions is rather small. Hopping of electrons between the two adjacent Mn-sites takes place with the participation of the bridge oxygen, but those details are not essential for this Chapter.

As for the X-rays absorption near-edge structure (XANES) data, they have been analyzed using the tight-binding model by Bridges et al. (2001).

The Bloch electronic wave function in the tight-binding approximation, as usual, may be chosen in a form

$$\Psi = \sum_n \mathrm{e}^{i\vec{p}\vec{a}_n} \psi(\vec{r} - \bar{a}_n) \ . \tag{5.1}$$

The summation is over all lattice centers $\vec{a}_n$, $\vec{p}$ is the quasimomentum, and ψ denotes the column formed by localized (atomic) wave function (see below). This is the only difference that comes from the fact that, according to Section 2.1, the state of the e_{2g}-electron is the double degenerate one.

In order to calculate the one-electron spectrum, one should choose the local basis set. It is convenient to use the normalized basic set of the form (Gor'kov and Kresin, 1998)

$$\begin{aligned} &\psi_1 \propto z^2 + \varepsilon x^2 + \varepsilon^2 y^2 \ , \\ &\psi_2 \equiv \psi_1^* \ , \end{aligned} \tag{5.2}$$

where $\varepsilon = \exp(2\pi \mathrm{i}/3)$. This choice allows us to account for the cubic symmetry of the initial lattice.

In principle, one can pick up another basis which is often used in literature, namely, the set of real functions (see Appendix A)

$$\begin{aligned} &\varphi_1 \propto d_{z^2} \equiv 3z^2 - (x^2 + y^2) \ , \\ &\varphi_2 \propto d_{z^2 - y^2} \equiv x^2 - y^2 \ . \end{aligned} \tag{5.3}$$

There is a simple connection between these two sets:

$$\begin{aligned} &\psi_1 = (\varphi_1 + \mathrm{i}\varphi_2)/\sqrt{2} \ , \\ &\psi_2 = \psi_1^* \ . \end{aligned} \tag{5.4}$$

Of course, the expression for the energy spectrum does not depend on the choice of the local basic set.

The equation of motion for an electron determining its energy spectrum is:

$$\varepsilon \begin{Bmatrix} \psi_1(\vec{r}_i) \\ \psi_a(\vec{r}_i) \end{Bmatrix} = \sum_{\vec{a}_n} \hat{T}_{i,i+m} \begin{Bmatrix} \psi_1(\vec{r}_i + \vec{a}_n) \\ \psi_a(\vec{r}_i + \vec{a}_n) \end{Bmatrix} , \tag{5.5}$$

$$\hat{T}_{ij} = \begin{Bmatrix} T^{11} & T^{12} \\ T^{21} & T^{22} \end{Bmatrix}, \tag{5.5'}$$

the summation in (5.5) goes over the nearest neighbors. The energy is referred to the energy level of the isolated ion ε_0, $\hat{T}$ is the hopping matrix. As a result, one has

$$T_{i,i+n}^{\nu\nu'} = \int \psi^{\nu}(\vec{r}_i)(V - W_a)\psi^{\nu'}(\vec{r}_i + \vec{a}_n)\,\mathrm{d}\vec{r} \tag{5.6}$$

where $\hat{T}$ is the matrix element calculated in the tight-bonding approximation (see, e.g., Ziman, 1960, Chapter 2), V and W_a are the periodic lattice and ionic local potentials, correspondingly (any constant term for $a_n = 0$ can be included into the value ε_0). With use of the basic set (5.2), one can explicitly find the form of the hopping matrix elements for the cubic lattice. One obtains

$$\begin{aligned} T_{11} &= T_{22} = (A + B)[c_x + c_y + c_z]\ , \\ T_{12} &= T_{21}^{*} = (A - B)[c_z + \varepsilon c_x + \varepsilon^2 c_y]\ . \end{aligned} \tag{5.7}$$

Here for shortness,

$$c_i = \cos(k_i a); \quad i \equiv x, y, z \tag{5.8}$$

(a is the lattice period).

The constants A, B, are defined, in accordance with Eqs. (5.3), (5.6) as the overlap integrals (Gor'kov and Kresin, 1998):

$$A \propto \overline{\varphi_1(z; x, y)}\,\overline{\varphi_1(z + a; x, y)}\ , \tag{5.9}$$

$$B \propto \overline{\varphi_2(z; x, y)}\,\overline{\varphi_2(z + a; x, y)}\ . \tag{5.10}$$

After simple calculation, we arrive at the following energy spectrum (Dzero et al., 2000):

$$\varepsilon_{1,2} = -(|A| + |B|)(c_x + c_y + c_z) \pm (|A| - |B|)R\ , \tag{5.11}$$

where

$$R = (c_x^2 + c_y^2 + c_z^2 - c_x c_y - c_y c_z - c_z c_x)^{1/2}\ . \tag{5.12}$$

One can see from (5.11) that the spectrum consists of the two branches. The two-band structure of the spectrum is a very important feature of metallic manganites especially, because the absence of the electron–hole symmetry in the overall experimental phase diagram for the $A_{1-x}R_xMnO_3$ materials.

Generally speaking, the energy spectrum can be expressed in terms of two constants (5.9), (5.10). It is interesting that in reality the situation is even simpler. The geometrical consideration (Anderson, 1959; Goodenough, 1963) for the d-shell overlap integrals shows that $|B| \ll |A|$ ($|B| \cong (1/16)|A|$). Therefore, with a good accuracy, the spectrum can be written in the form:

$$\varepsilon_{1,2}(\vec{k}) = -|A|(c_x + c_y + c_z \pm R)\ , \tag{5.13}$$

where R is defined by Eq. (5.12).

Eq. (5.13) determines the dispersion of each band. Numerically, all the band features (the width of the band, etc.) depend only on the value of single constant, $|A|$. The latter can be determined from the experimentally measured parameters. As it turns out, it is most convenient to use for that purpose the spin wave spectrum, or, more precisely, the measured value of spin stiffness coefficient (see below, Section 5.5). From these data we obtain: $|A| \cong 0.16\,\mathrm{eV}$.

A few words regarding the Hund's term, Eq. (4.1). As we assumed above, this term is the largest one, so that in what follows we use strong inequality $J_H \gg |A|$. Therefore, all branches of the electronic spectrum are shifted up or down by the energy $\pm J_H S$, depending on the e_{2g}- and t_{2g}-mutual spin orientation. Itinerant spins for each of the branches would merely split into two by adding the $\pm J_H \langle S\rangle$ energy term.

Therefore, the lowest two bands correspond to the parallel orientation of the e_{2g}- and local t_{2g}-spins:

$$\varepsilon^{\mathrm{L}}_{1,2} = -J_H\langle S\rangle - |A|(c_x + c_y + c_z \pm R) \tag{5.14}$$

with (Dzero et al., 2000)

$$|A| \cong 0.16\,\mathrm{eV}\ , \tag{5.15}$$

c_i and R are defined by Eqs. (5.8) and (5.12).

There are also two upper bands:

$$\varepsilon^{v}_{1,2} = J_H\langle S\rangle - |A|(c_z + c_y + c_z \pm R)\ . \tag{5.16}$$

However, the ground state is always formed by making use of the two lowest bands $\varepsilon^{\mathrm{L}}_{1,2}$.

With use of (5.13), (5.15) one can estimate the total width of the spectrum ΔE:

$$W = 6|A|\ . \tag{5.17}$$

In accordance with (5.15), ΔE is of order of 1 eV. In practice, at all concentrations, the Fermi level lies at lower energies. In metallic manganites we are dealing with relatively narrow energy bands.

The two-band structure of the electron spectrum is an important feature of metallic manganites. Let us repeat that it naturally explains the observed asymmetry of the phase diagram (hole vs. electron doping). Moreover, it is essential for a detailed description of various features of the compounds and, especially, their optical properties (see Section 5.6).

It is worth noting that such important quantity as the magnetoresistance (MR) was calculated in the one-band model (Millis et al., 1996b; see discussion above Section 4). It would be interesting to perform calculations using the two-band picture. One should not expect, however, a profound impact of the two-band spectrum on MR but some deviations from the one-band picture.

Note also that the value of A, Eq. (5.15), obtained from experimental data, is relatively small and is on the scale of the ionic energy. This is due to specific polaronic effect (see below, Section 5.5).

5.2. Fermi surface and its evolution with doping

With the help of the spectrum (5.13)–(5.15), one can calculate the concentration dependence of the Fermi level, $E_{\mathrm{F}}(x)$ and reconstruct the Fermi surface. The Fermi surface topology is shown in Fig. 7. Fermi surfaces in Figs. 7a–c are for concentrations $x = 0.2$, 0.3, 0.5, respectively. An interesting fact is that $x = 0.3$ is the concentration at which a "neck" develops on the Fermi surface at the zone boundary. In other words, concentration $x = 0.3$ is the point of "2.5"—Lifshitz transition at which the change in the

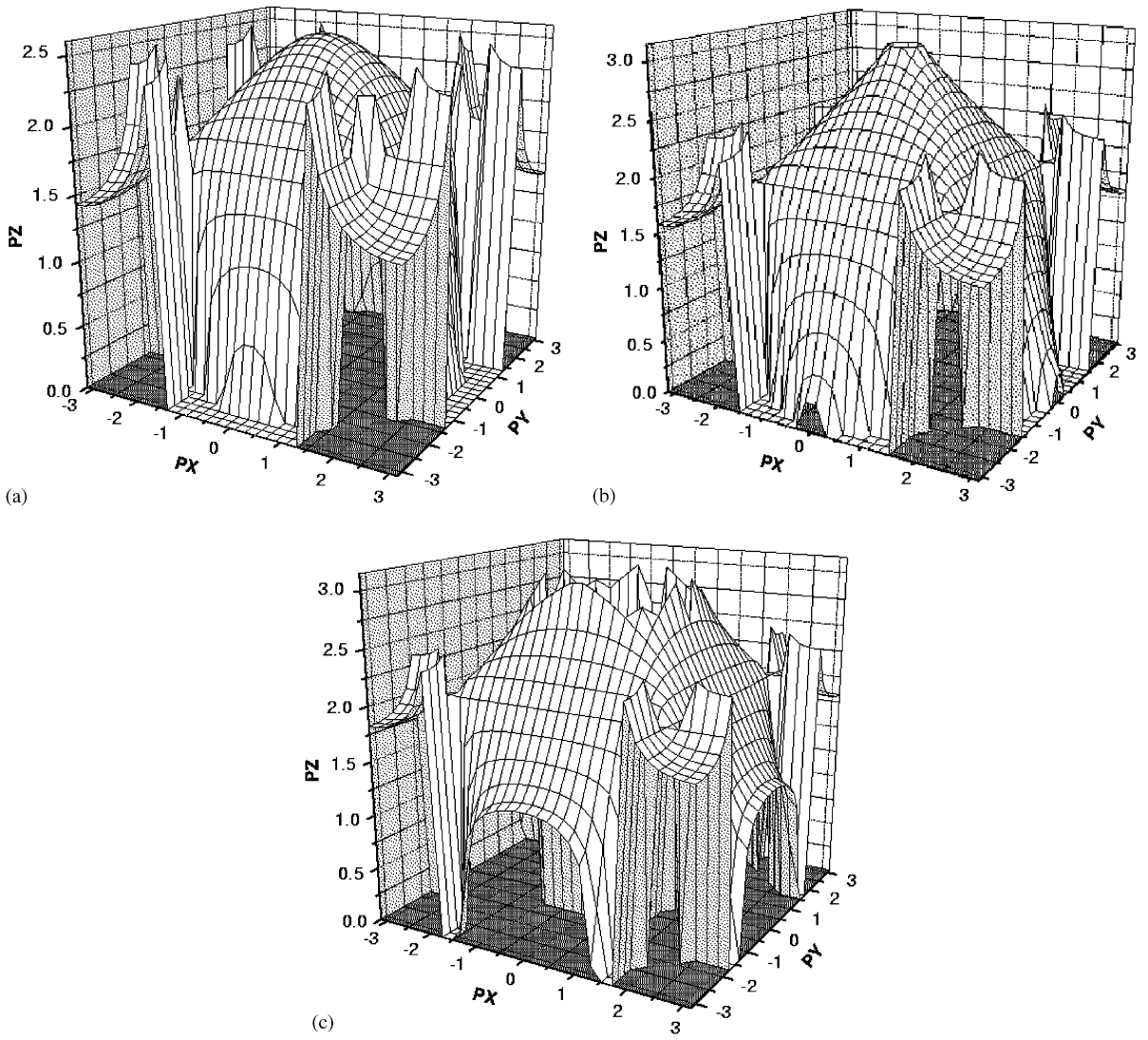

Fig. 7. Fermi surface at: (a) $x = 0.2$, (b) $x = 0.3$, (c) $x = 0.5$.

Fermi surface topology occurs (Lifshitz, 1960; see also Blanter et al., 1994). The doping level $x = 0.3$ is also interesting because it is inside the region with a maximum value of T_C and, correspondingly, with a maximum value of the temperature for the CMR phenomenon.

Fig. 8 shows the calculated dependence of the distance of the Fermi level from the band bottom on the carrier concentration. One can see that the value of the Fermi energy is indeed small (e.g., $|E_F| \cong 1.2\ |A| \cong 0.2$ eV) and is less than typical E_F-values for usual metals ($\cong$ 5–10 eV).

The concentration dependence of the density of states $\nu_F(x)$ is shown in Fig. 8. It is interesting that this function has a rather sharp peak near $x \cong 0.3$ with a jump in the derivative. This singularity corresponds

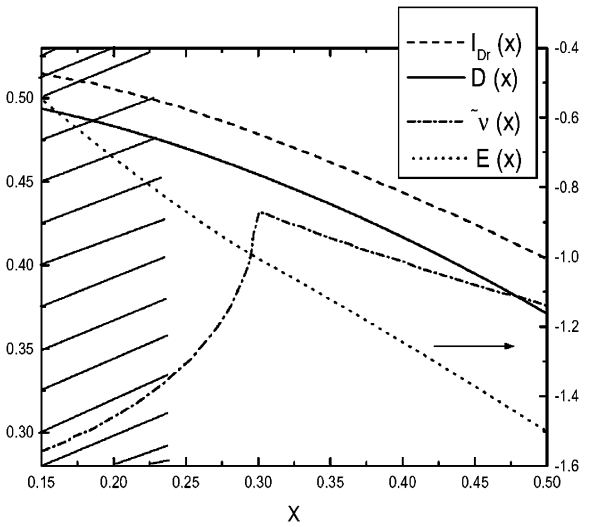

Fig. 8. The dimensionless Fermi level (in units of $|A|$), $E(x)$, density of states, $\tilde{\nu}(x)$, the spin stiffness coefficient, $D(x)$ (Eq. (5.27)), and the Drude conductivity, $I_{\mathrm{Dr.}}(x)$, (Eq. (5.44)) plotted as a function of concentration, x, for the spectrum, given by Eq. (5.13). The meaning of different lines is indicated in the onset. The shaded area shows the percolative regime.

to the above mentioned "neck" structure (Fig. 7) and closeness of the concentration to the "2.5" Lifshitz transition.

5.3. Spin waves

In addition to the one-particle energy spectrum (Section 5.1) the model also describes the collective excitations, and, first of all, the spectrum of the spin waves for the ferromagnetic metallic phase. Let us start from the Hamiltonian:

$$\hat{H} = \sum_{\vec{p}} t(\vec{p}) a^{+}_{\vec{p}\sigma} a_{\vec{p}\sigma} - J_H \sum_i a^{+}_{i\mu} \hat{\tilde{\sigma}}_{\mu v} a_{iv} \hat{S}_i \ , \tag{5.18}$$

cf. (4.4), the lattice terms are omitted.

The evaluation of the spin wave spectrum should be taken with some care, since the Hamiltonian (5.18) differs drastically from that one for usual local spins ferromagnetics. It reflects the different nature of the ferromagnetic ordering in manganites caused by the interplay of the Hund's interaction and hopping (double exchange mechanism). In addition, it is necessary to take into account the double-band structure (Eq. (5.13)) of the electronic spectrum. Note that the spin wave spectrum was written down by Furukawa for the single-band model only (1996). The paper is a part of the series of interesting publications (Furukawa, 1994, 1995a, b, 2003a, b) describing the impact of the double exchange model on various properties of manganites (e.g., dependence of T_{C} on doping level).

Below we follow the comprehensive two-band analysis (Dzero et al., 1999, 2000). The Hamiltonian (5.18) can be written in the form

$$\hat{H} = \hat{H}_o + \hat{H}_{\mathrm{int}} \ , \tag{5.19}$$

where

$$\hat{H}_o = \sum_{\vec{p}} t(\vec{p}) a^+_{\vec{p}\mu} a_{\vec{p}\mu} - J_H \langle S_z \rangle \sum_{\vec{p}} a_{\vec{p}\mu} a_{\vec{p}\mu} \hat{S}_z \ ,$$

$$\hat{H}_{\rm int} = -J_H \sum_i a^+_{i\mu} \hat{\sigma}_{z;\mu\nu} a_{i\nu} (\hat{S}_z - \langle S_z \rangle) - J_H \sum_{i,\alpha} a^+_{i\mu} \hat{\sigma}_{\alpha;\mu\nu} a_{i\nu} \hat{S}_\alpha; \quad \alpha \equiv (x, y) \ . \tag{5.20}$$

To calculate spin waves spectrum, one needs to know the energy of the system up to quadratic terms in the spin derivations from the equilibrium value.

Introducing in the usual way the Bose-amplitudes b_i, b_i^+ (see, e.g., Kittel, 1963):

$$b_i = (2\langle S \rangle)^{-1/2} S_i^+, \quad b_i^+ = (2\langle S \rangle)^{-1/2} S_i, \quad S_i^\pm = \hat{S}_{ix} \pm \hat{S}_{iy} \ ,$$

we obtain

$$\hat{H}_{\rm int} = \hat{H}^{(1)} + \hat{H}^{(2)} \ ,$$

$$\hat{H}^{(1)} = -\frac{1}{2} J_H n \sum_{\vec{q}} b^+_{\vec{q}} b_{\vec{q}} \ , \tag{5.21}$$

$$\hat{H}^{(2)} = \frac{1}{2} J_H \langle S_z \rangle \left[\sum_{\vec{p},\vec{q}} a^+_{\vec{p},\mu} \hat{\sigma}_{x;\mu\nu} a_{\vec{p}-\vec{q};\upsilon} (b^+_{\vec{q}} + b_{\vec{q}}) + i \sum_{\vec{p},\vec{q}} a^+_{\vec{p};\mu} \hat{\sigma}_{y;\mu\nu} a_{\vec{p}-\vec{q};\upsilon} (b^+_{\vec{q}} - b_{\vec{q}}) \right] \ . \tag{5.22}$$

With the Hamiltonian (5.22) the next step is to calculate the second order corrections to the energy of the ground state. For that one needs to use the matrix elements between the Bloch states (5.1). To be specific, the result contains the amplitudes of the transition between the occupied (lowest) bands, see Eq. (5.14) and the vacant (upper) bands, Eq. (5.16). These amplitudes also include the off-diagonal terms of the hopping matrix, Eqs. (5.6), (5.7). The major task is to calculate the second order contribution δE_2 which turns out to be equal to

$$\delta E_2 = 2 J_H^2 \sum_k \langle S_z \rangle \hat{b}^+(\vec{k}) \hat{b}(\vec{k}) \sum_{l,\vec{p}} \left(\sum_{l'} \frac{|\alpha^l_{\vec{p}} \alpha^{*l'}_{\vec{p}+\vec{k}} + \beta^l_{\vec{p}} \beta^{*l'}_{\vec{p}+\vec{k}}|^2}{E^l_\uparrow(\vec{p}) - E^{l'}_\downarrow(\vec{p}+\vec{k})} \right) \tag{5.23}$$

where

$$E^{l,l'}_{\uparrow,\downarrow}(p) = \mp J_H \langle S_z \rangle + \varepsilon_{l,l'}(p) \ . \tag{5.24}$$

Both sums in (5.23) run over $l, l' = \pm$, see (Eq. (5.13)). The summation over l and p is limited by the occupied states ($\uparrow$) only. The coefficients (α^l_p, β^l_p) above are calculated for the Bloch's states by using basis (5.2)

$$\alpha^{l,l'}_p = (T_{12}/2|T_{12}|)^{1/2}, \quad \beta^{l,l'}_p = \pm (T_{21}/2|T_{12}|)^{1/2} \tag{5.25}$$

(here T_{12}, T_{21} are the off-diagonal elements of the hopping matrix $\hat{t}(p)$ Eq. (5.7), in this basis). Since $J_H \gg |A|$, $J_H S_z$ is of the order of 1.5 eV, $|A| \approx 0.16$ eV. Expanding (5.21) in $(|A|/J_H)$ would result in a series of the Heisenberg spin Hamiltonians accounting for interactions with the increasing number of

neighbors. After a somewhat tedious, but straightforward calculation, the first order term in $|A|$ from (5.23) becomes ($\langle S_z\rangle = 3/2$):

$$\hbar\omega(k) = |A|(3 - c_x - c_y - c_z)D(x)/3 \ , \tag{5.26}$$

where $D(x)$ is given by the integral

$$\int \frac{\mathrm{d}^3\vec{p}}{(2\pi)^3}\left|\sum_{(+,-)}\theta(E-\varepsilon_i(\vec{p}))\left\{1 \pm \frac{2c_x - c_y - c_z}{2R(\vec{p})}\right\}\right| \ . \tag{5.27}$$

Quantity $D(x)$ depends on the carrier concentration through the Fermi level position and is plotted on Fig. 8.

Eq. (5.26) determines the spin waves spectrum. In the long-wave limit the spectrum has a form

$$\hbar\omega(\vec{k}) = D_{\text{stiff.}}k^2 \ , \tag{5.28}$$

where

$$D_{\text{stiff.}} = \frac{a^2}{6}|A|D(x) \ . \tag{5.29}$$

The spin stiffness coefficient D_{stiff} can be measured experimentally. As was stated above (see the discussion following Eq. (5.13)), data for the spin stiffness D_{stiff} can be used in order to determine the value of the single band parameter, $|A|$. The use of data for D_{stiff} looks preferential, because the coefficient being a long-wave characteristic should not be very sensitive to the defects or sample's quality. Indeed, while the measured values for D_{stiff} may differ for various compounds, the difference, indeed, is rather small. For example, according to Martin et al. (1996), the value of $D_{\text{stiff.}}$ for the compound $La_{0.7}Sr_{0.3}MnO_3$ equals $D_{\text{stiff}} \cong 188\,\text{meV}\,\mathring{A}$. The value of $D_{\text{stiff}} \cong 176$ has been reported for the same Sr-concentration compound by Vasiliu-Doloc et al. (1997). Somewhat smaller value of D_{stiff} for $La_{0.7}Sr_{0.3}MnO_3$ was reported ($170\,\text{meV}\,\mathring{A}$) by Lynn et al. (1996). Using the values of the lattice period $a \cong 3.86\,\mathring{A}$ and choosing an average value, $D_{\text{stiff}} = 180\,\text{meV}\mathring{A}$, and making use of the calculated $D(x=0.3) \cong 0.45$, see Fig. 8, we derive for $|A| \cong 0.16\,\text{eV}$, that is, the value that we have had introduced above (Eq. (5.15)).

Let us discuss briefly some other experimental data. The spin wave dispersion has also been measured along all major symmetry direction for $La_{0.7}Pb_{0.3}MnO_3$ (Perring et al., 1996). Results are in a rather good agreement with Eq. (5.26).

In principle, there might be deviations from the simple dependence, Eq. (5.26), particularly in the short-wave limit. Indeed, expression (5.26) was derived for the clean metallic band picture without taking into account quantum fluctuations, possible proximity to other phases (such as the percolation effects). Recall also that other terms of order t^2/J_H were neglected. Experimentally deviations from the simple dependence (5.26) have been observed by Hwang et al. (1998) at $\xi > 0.25(\bar{\pi}a)$ for $(0, 0, \xi)$ direction in $Pr_{0.67}Sr_{0.37}MnO_3$. We think this that fact may be also related to the tendency to the charge ordering or to the admixture of the metallic A-phase (see below, Section 6). Similar behavior, indeed, is seen in the data by Moudden et al. (1998) and Endoh and Hirota (1997) for $La_{1-x}Sr_xMnO_3$ ($x < 0.2$) where it obviously originated from the percolation effects (shadow region in Fig. 8).

Theoretically, far away from the percolation threshold, the calculated stiffness coefficient, $D(x)$, slowly decreases as a function of x, see Fig. 8. This decrease is caused by a decrease in a number of e_{2g}-electrons and, correspondingly, by a decrease in the value of the saturation moment, $M(x)$. This decrease is relatively

shallow and its experimental observation would need being more detailed on the spin wave spectrum and samples of a higher quality.

5.4. Heat capacity

As is known, there are several contributions to the low temperature heat capacity. In ferromagnetic manganites, in addition to the common electronic ($\propto T$) and phonon ($\propto T^3$) terms, there is also a contribution from spin waves (magnons, see the previous section). The dispersion law (5.26) leads to the contribution to the total energy of the form; $E \propto \int d\vec{k}\,\omega(\vec{k})[\exp(\hbar\omega/kT)-1]^{-1} \propto T^{5/2}$ (one should make the transformation $d\vec{k} \to d\omega(\vec{k})$ and take into account Eq. (5.26)). Therefore, $C_{\text{mag.}} \propto T^{3/2}$. Remember, however, that $\tilde{\nu}(x)$ has a kink at $x \approx 0.3$. That kink takes its origin from the fact that this concentration is the point of the 2.5-"Lifshitz" singularity, as it may also be clearly seen from the Fermi surface pattern in Fig. 7. As was just mentioned, the total magnon contribution into specific heat is proportional to $T^{3/2}$. The proximity to the Lifshitz "2.5" transition results in appearance of a term in the electronic specific heat term with same T-dependence. This observation makes the procedure of extracting the "pure" magnon $\propto T^{3/2}$ terms less transparent.

Spectrum (5.14), (5.15) was used in order to calculate the density of states per single spin $\nu(x)$ (see Section 5.1 and Fig. 8) and then the usual linear electronic term $C = \gamma T$ with the Sommerfeld constant $\gamma = \pi^2\nu/3$. With use of the value $\tilde{\nu}(x) = \nu(x)/|a| \cong 0.45$ at $x = 0.3$ (see Fig. 8) and the value $|A| \cong 0.16$, we obtain $\gamma \cong 6\,\text{mJ/mol K}^2$.

Speaking of the experimental specific heat data, one should note that the unambiguous determination of the electronic contribution turns out to be a difficult task (Hamilton et al., 1996; Gordon et al., 2001; see also review Coey et al., 1999). In addition, the existence of two terms with the same ($\propto T^{3/2}$) dependence makes finding the electronic component even more complicated. Probably, somewhat more reliable specific heat data would come from the measurements with the materials where the concentration x is relatively distant from the singular point $x \cong 0.3$. So far, the measurements for several manganites has resulted in γ that lies in the 3–8 mJ/mol K^2 range. For example, the value $\gamma = 5.8\,\text{mJ/mol K}^2$ was obtained by Viret et al. (1997); the value $\gamma \cong 3.5\,\text{mJ/mol K}^2$ was reported by Okuda et al. (1998), and the value $\gamma \cong 4\,\text{mJ/mol K}^2$ was measured by Gordon et al. (2001). As a whole, one could state, that there is at least qualitative agreement with the value $\gamma \cong 6\,\text{mJ/mol K}^2$ calculated for $x \approx 0.3$ with the help of density of states (Fig. 8).

5.5. Isotope substitution

The parameter A which is a single parameter of our theory describes the charge transfer between neighboring manganese ions. We did not calculate this parameter and its value was determined from the experimental data (see above, Section 5.3). This approach is consistent and allows us to describe numerous experimental data discussed in this chapter (see also Section 7). Let us repeat, that the parameter A can be determined experimentally (see Section 5.1). Up to this section it was not necessary to discuss various factors affecting its value. However, the observed effect of oxygen substitution on T_C (Zhao et al., 1996; Franck et al., 1998; see also review by Belova, 2000) requires a special analysis. It turns out that the oxygen isotope substitution ($O^{16} \Rightarrow O^{18}$) leads to a large shift in the Curie temperature, $T_C \propto M^{-\alpha}$, where, for instance, for $La_{0.8}Ca_{0.2}MnO_3$ the isotope coefficient α is quite large and equals to $\alpha \approx 0.85$. This raises the question whether one could analyze the tunneling matrix theoretically.

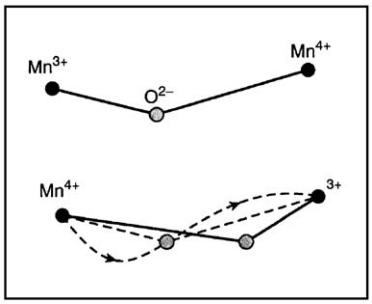

Fig. 9. Mn–O–Mn unit; two close minima for the O-ion (Sharma et al., 1996).

The oxygen ion is located between the Mn ions, and it turns out that its dynamics is directly involved in the process of a charge transfer. Seated just between two Mn-ion, the oxygen ion, in addition, is characterized by *two* minima. Rapid incoherent transitions of the oxygen between minima positions lead to a peculiar dynamic lattice effect, called the "polaronic band narrowing" (see, e.g., Bersuker and Polinger, 1989; Bersuker, 1996). One can show that this phenomenon leads to the aforementioned oxygen isotope effect (Kresin and Wolf, 1997, 1998).

Such a behavior of the Mn–O–Mn unit is most pronounced in the vibrational motion of the oxygen ion which is the lightest member of the unit. This effect has a resemblance to the ordinary JT effect in the sense that since the presence of two close minima means that these minima are in proximity to the two electronic terms crossing. In this vicinity it is impossible to separate the electronic and ionic motions. It is interesting that, indeed, such a dynamic picture of the oxygen moving between two minima has been observed by means of a novel ion channeling technique (Sharma et al., 1996), see Fig. 9. This experimental result has stressed the fact that the dynamics of the oxygen motion is drastically different from what would be seen in the harmonic approximation and is, indeed, strongly anharmonic as the result of to two close minima in the ion energy potential.

In the presence of two minima the total wave function of the electron-ion system becomes a superposition of two configurations which we denote schematically as: (α) $A^+O_\alpha A$, (β) $AO_\beta A^+$; here $A \equiv Mn^{3+}$, $A^+ \equiv Mn^{4+}$. O_α means that the oxygen ion is shifted towards the left minimum, while for the β configuration, O_β, lies closer to the right minimum. The total wave function $\Phi(\vec{r}, \vec{R})$ (for the ionic and electronic coordinates) can be expressed in the form

$$\Phi(\vec{r}, \vec{R}) = C_\alpha \varphi_\alpha(\vec{r}, \vec{R})\phi_\alpha(\vec{R}) + C_\beta \varphi_\beta(\vec{r}, \vec{R})\phi_\beta(\vec{R}) \ . \tag{5.30}$$

Here φ_i and ϕ_i ($i \equiv \alpha, \beta$) are the electronic and nuclear wavefunctions, corresponding to the two crossing left α and right β terms. Such approach is called the diabatic approximation (O'Malley, 1967; Kresin and Lester, 1984). Here one assumes that the wavefunction φ_α coincides with the eigenfunction of the total electronic Hamiltonian $H_e = \hat{T}_{\vec{r}} + V(\vec{r}, \vec{R})$ constructed for the region α; analogous behavior supposed to be true for φ_β ($\hat{T}_{\vec{r}}$ is the electronic kinetic energy operator, and $V(\vec{r}, \vec{R})$ is the total potential energy of electron at the ion position, $\vec{R}$). Hence, because of the electronic terms crossing, the total wavefunction (see Eq. (5.30)) does not have the form of a product of electronic and nuclear wavefunctions. The presence of two close minima makes it impossible to separate the electronic and nuclear motions (contrary to the usual adiabatic picture (Born–Oppenheimer approximation)).

Symmetry of the problem results in the appearance of symmetric and asymmetric coupled electron–ion energy terms. One can evaluate the energy splitting ΔE between these terms. After performing straightforward calculations, we obtain

$$\Delta E = \int L(\vec{R})\phi_\alpha(\vec{R})\phi_\beta(\vec{R})\,\mathrm{d}\vec{R}\ . \tag{5.31}$$

Unlike expressions (5.11), (5.12), this value depends on the overlap of both the electronic and ionic wavefunctions. Here, in (5.31), $L(\vec{R})$ is the electronic factor:

$$L(\vec{R}) = H_{e;ik}(\vec{R}) = \int \mathrm{d}\vec{r}\,\varphi_i^*(\vec{r},\,\vec{R})H_e(\vec{r},\,\vec{R})\varphi_k(\vec{r},\,\vec{R})\ . \tag{5.32}$$

In the diabatic representation the matrix elements $H_{\mathrm{e};ik}$ $(i \neq k)$ differ from zero (for the overlapping electron potential wells).

As before, the energy splitting corresponds to inverse time for the charge hopping between the two Mn ions ($\Delta E \propto \tau^{-1}$). Since the ferromagnetic ordering is caused by the electron hopping, the splitting provides for the estimate the value of the critical temperature for the ferromagnetic ordering; in other words, it is natural to assume that $T_\mathrm{C} \propto \Delta E$ (Millis et al., 1996a, b).

Compared to Eq. (5.11), (5.12), this splitting in (5.31) actually depends on the fact that the vibrational wavefunctions ϕ_α and ϕ_β are peaked near minima in the regions α or β, respectively. Contribution into the integrand in (5.31) mainly comes from R of order r, r is the distance between the minima. Since $r \ll L$, where L is the length of the bond, one can put $L(\vec{R}) \approx L_0 \equiv L(\vec{R}_0)$, and we obtain

$$\Delta E \approx L_0 F\ , \tag{5.33}$$

where L_0 is the electronic factor (at $\vec{R} = \vec{R}_0$), determined by Eq. (5.32), and

$$F = \int \phi_\alpha(\vec{R})\phi_\beta(\vec{R})\,\mathrm{d}\vec{R} \tag{5.34}$$

is the Franck–Condon (FC) factor.

Once again, the electronic factor L_0 determines the hopping parameter, A (and, therefore, T_C in terms of the usual double exchange model) with the *frozen* lattice. One can see from Eq. (5.33) that the account of the O ion dynamics leads to the appearance of the additional FC factor. The obvious inequality, $F < 1$, leads to a decrease in the energy splitting, and, correspondingly, results in an effective narrowing of the band. As was indicated above, this effect was not explicitly considered in our treatment, see Sections 5.1–5.3, but was taken into account in a natural way, since the value of the parameter A was determined from experimental data. The presence of the FC factor leads to the oxygen isotope effect (see below).

After the brief summary of the theoretical scheme, it is worth adding some qualitative remarks. The charge transfer for the extra-electron can be visualized as a multistep process; first the electron makes a transition from the Mn^{4+} site to the oxygen, then the oxygen goes over to another minimum, and from where the electron jumps into the other Mn ion. Therefore, actually, the charge transfer includes such an important additional step as the oxygen movement between two minima. Namely, this additional step leads to a drastic increase, described by the FC factor, in the characteristic time for the jump between two Mn ions. Naturally, this factor also decreases the strength of the ferromagnetic coupling, and, consequently, T_C. In the traditional language, charge transfer is accompanied by the transition to another electronic term; this process is similar to the Landau–Zener effect (see, e.g., Landau and Lifshitz, 1976).

Let us now return to discussion of isotopic effects in manganites. As noted above, the dependence on the mass of the oxygen isotope is brought into the problem through the appearance of the FC factor. Indeed, this factor contains overlap of the nuclear wavefunctions and, therefore, depends on the nuclear mass M (in our case the mass of the O ion). To estimate the FC factor, Eq. (5.34), we take the harmonic oscillator wavefunctions with the shift $\Delta\rho$ for the oscillators equilibrium positions. For simplicity, consider a one-dimensional model. We obtain: $F = \exp(-\kappa^2)$, $\kappa = (\Delta\rho/2\rho)$, where $\rho = (\hbar/M\Omega)^{1/2}$ is the vibration amplitude. If we take the value $\kappa \approx 1.25$–1.5 (this is consistent with the data by Sharma et al., 1996), we obtain $F \approx 0.18$–0.2. The value of the isotope coefficient appears to be in good agreement with the data (Zhao et al., 1996). Indeed, defining the isotope coefficient α by the relation $T_C \propto M^{-\alpha}$ one re-writes it as $\alpha = -(M/\Delta M)(\Delta T_C/T_C)$; with $T_C \propto \Delta E$, we obtain

$$\alpha = (M/\Delta M)(\Delta T_C/T_C) = -(M/\Delta M)(\Delta F/F) \tag{5.35}$$

where $\Delta M = M - M^*$; we used the relation $T_C \propto \Delta E$ and Eq. (5.33). Based on the expression for the FC factor (see Eq. (5.34)), we obtain $\alpha = 0.5\kappa^2$. Using the value $\kappa \approx 1.25$–1.5, we obtain the values in the range of 0.8–1, in good agreement with the value obtained by Zhao et al. (1996).

It is worth noting that the expression $T_C \propto \Delta E$ does not determine explicitly the value of T_C. This value is affected also by the loss of the coherence inside of a whole Mn–O network. However, Eq. (5.35) allows us to analyze the isotope effect.

To conclude this section, the charge transfer in the metallic manganites not merely goes through tunneling across the oxygen ions. It is accompanied by the motion of the O ion between two minima. The electron becomes "dressed" by this motion. It is obvious that in any band calculations one must take into account the existence of such a dynamic polaronic effect.

5.6. Optical properties

Study of optical properties of metallic manganites is of the special interest, because it is necessary to take into consideration the two-band structure of the spectrum. For manganites, the interband transitions appear to be the key factor in the IR region (see below).

The a.c. conductivity is described by a well-known Kubo–Grinwood expression:

$$\sigma_{ij} = -\frac{e^2\hbar^2}{V\omega}\sum_{k,k'} f_0(\vec{k})[1 - f_0(\vec{k}')]\langle \Psi(\vec{k}')|\hat{\vec{v}}_i|\Psi(\vec{k}')\rangle\langle\Psi(\vec{k}')|\hat{\vec{v}}_i\Psi(\vec{k})\rangle \times [\delta(\varepsilon(\vec{k}') - \varepsilon(\vec{k}) - \omega) - \delta(\varepsilon(\vec{k}') - \varepsilon(\vec{k}) + \omega)] , \tag{5.36}$$

where $f_0(k)$ is the Fermi distribution function, $\vec{k}$ is a quasi-momentum, $\vec{v}_i$ is a velocity operator, and $\Psi(\vec{k})$ is the two-column electron wave functions (5.1). For the cubic crystal $\sigma_{ij} = \sigma_{ij}$.

To start with, we determine the velocity operator, $\hat{\vec{v}} = \hat{r}'$ (see Lifshitz and Pitaevskii, 1989)

$$\hat{\vec{v}}(\vec{k}) = \frac{1}{\hbar}\frac{\partial\varepsilon_l(\vec{k})}{\partial\vec{k}} + \frac{\mathrm{i}}{\hbar}[\varepsilon_l(\vec{k}) - \varepsilon_i(\vec{k})]\langle l\vec{k}|\hat{\vec{\Omega}}|l'\vec{k}\rangle . \tag{5.37}$$

The off-diagonal operator $\hat{\Omega}$ is defined by the relation:

$$\langle l\vec{k}|\hat{\vec{\Omega}}|l'\vec{k}\rangle = \mathrm{i}\int u^{*l'}_{\vec{k}}(\vec{r})\frac{\partial u^{l}_{\vec{k}}}{\partial\vec{k}}\,\mathrm{d}^3\vec{r} \tag{5.38}$$

and $u^l_k(r)$, the periodic Bloch functions.

$$u^l_{\vec{k}}(\vec{r}) = \Psi^l_{\vec{k}}(\vec{r})\mathrm{e}^{-\mathrm{i}\vec{k}\vec{r}} \ , \tag{5.39}$$

where $\Psi^l_{\vec{k}}(\vec{r})$ is defined by Eq. (5.1).

Since l, l' are the band indexes, the second term in (5.37) explicitly includes the interband transitions. The light absorption comes about due to these contributions. These are the direct transitions and their importance of these transitions for the light absorption is simply due to negligibly small value of the photon's momentum. As a result, a conservations of energy and momentum can be simultaneously satisfied (in the clean limit) only for the interband transitions.

Based on Eqs. (5.1) and (5.39) one can write

$$u^l_{\vec{k}}(\vec{r}) = \frac{1}{\sqrt{N}} \sum_{\vec{n}} \exp\left[\mathrm{i}\vec{k}(a\vec{n} - \vec{r})\right] \left\{\alpha^l_{\vec{k}}\psi_1(\vec{r} - \vec{n}a) + \beta^l_{\vec{k}}\psi_2(\vec{r} - \vec{n}a)\right\} \ . \tag{5.40}$$

The functions ϕ_1 and ϕ_2 are the two component basic set (see Eq. (5.2)), and the coefficients α^l_k and β^l_k are determined by Eqs. (5.7), (5.25).

With the use of Eqs. (5.2), (5.7), (5.25) and (5.40), one can evaluate the matrix elements (5.38) responsible for the interband transitions. Performing the integration in (5.38) we neglect by the other small overlapping terms (one-site approximation). After straightforward calculations, it follows:

$$\langle l\vec{k}|\hat{\tilde{\Omega}}|l'\vec{k}\rangle = \mathrm{i}\,\frac{a}{\hbar}\,\frac{\sqrt{3}}{4}\,\frac{(-\sin k_x)(c_y - c_z)}{|t_{12}|^2} \ . \tag{5.41}$$

As a result (see Eqs. (5.36), (5.37), (5.41)), one arrives to the following expression for the "optical" (interband) contribution (Takahashi and Shiba, 1998; Dzero et al., 2000)

$$\sigma_{\mathrm{opt}}(\omega, x) = \frac{3\pi e^2}{a\hbar}\frac{1}{\tilde{\omega}^3}\int \frac{\mathrm{d}^3\vec{p}}{(2\pi)^3}\sin^2 p_x(c_y - c_x)^2 \times n(\varepsilon_+(\vec{p}))[1 - n(\varepsilon_-(\vec{p}))]\delta(\tilde{\omega} - 2R(\vec{p})) \ . \tag{5.42}$$

The first term in Eq. (5.37) leads to the intraband (Drude) term

$$\sigma_{\mathrm{Drude}}(\omega, x) = 2\pi\,\frac{e^2|A|}{3a\hbar^2}\delta(\omega) I_{\mathrm{Dr}}(x) \ , \tag{5.43}$$

$$I_{\mathrm{Dr}}(x) = \frac{1}{2(2\pi)^3}\sum_l \int \mathrm{d}S^l_{\vec{p}}|\nabla_{\vec{p}}\varepsilon(\vec{p})| \ . \tag{5.44}$$

Eq. (5.43) is written down for the "clean" case. As is known, the presence of impurities leads to possibility to satisfy both conservation laws for the intraband transitions. Instead (5.43), we obtain for the Drude "tail" the dependence

$$\mathrm{Re}\,\sigma_{\mathrm{Drude}}(\omega, x) \equiv \frac{\sigma_0(x)}{\omega^2 + \tau^2} \ , \tag{5.45}$$

where τ is the relaxation time.

Integration in $I_{\rm Dr}(x)$, Eq. (5.44) goes over the Fermi surfaces. As for the parameter $|A|$, we estimated above its value $|A| \cong 0.16\,\text{eV}$, see Eq. (5.15). The dependence $I_{\rm Dr}(x)$ is plotted in Fig. 8.

Therefore, the general expression for conductivity contains two contributions: the Drude (intraband) term (Eqs. (5.43)–(5.45) and the interband term (Eq. (5.42)). For the low temperature spectral weight

$$N_{\rm eff} = \frac{2m}{\pi e^2} a^3 \int_0^\infty \sigma(\omega)\,\mathrm{d}\omega \tag{5.46}$$

one obtains both the Drude and the interband contributions, respectively:

$$N_{\rm eff}^{\rm Drude} = \frac{ma^2}{3\hbar^2}\,|A| I_{\rm Dr}(x) \tag{5.47}$$

$$N_{\rm eff}^{\rm opt} = \frac{ma^2}{\hbar^2}\,|A| \frac{3}{4}\, I_{\rm opt}(x) \tag{5.48}$$

(the expression for $I_{\rm opt}(x)$ can be directly obtained from (5.42)).

Turning now to the discussion of experimental data, one should mention that the temperature dependence of the optical conductivity, $\sigma(\omega)$, has attracted recently much attention (Okuda et al., 1998; Quijada et al., 1998; Okimoto and Tokura, 2000) as a way to keep track of changes in the conductivity mechanism from a metallic conductivity at low temperatures to conductivity of localized polarons at elevated temperatures. We mention here only a few results pertinent to the low temperature band mechanisms. First note, that the temperature dependence in $\sigma(\omega)$ at $T < 100\,\text{K}$ for the low frequency peak is, indeed, most pronounced below 1 eV (Quijada et al., 1998). This agrees well with our estimates for the bandwidths, $W < 1\,\text{eV}$. Moreover, if we calculate the spectral weight and assuming that both the Drude and optical contributions are approximately equal, we obtain $N_{\rm eff} \approx 0.25$ which is reasonably close to the value measured by Quijada et al. (1998). At the same time one should keep in mind that there is a noticeable difference between the data obtained by different groups. Probably, this difference is due to difficulty in separating of purely electronic part of conductivity, and/or difference in the samples quality, that is especially important in the "Drude-tail" frequency range.

5.7. Disorder. d.c. conductivity

The metallic manganites are not ordinary metals. Their carriers and, hence, conductivity are exclusively due to doping. This process (substitutional doping) leads to the lattice deformation. Mismatch between the sizes of different ions is expressed by the value of the tolerance factor, t (Goldschmidt, 1958)

$$t = \frac{1}{\sqrt{2}} \cdot \frac{R_{\rm B} + R_{\rm O}}{R_{\rm A} + R_{\rm O}}\ , \tag{5.49}$$

where R_i $(i = \text{A, B, O})$ are the ionic radii of each element in ABO_3.

For example, the ionic radii for Mn^{3+} is equal to 0.0645 nm, for La^{3+} is 0.136 nm. For the ideal seized ions the tolerance factor is equal to $t \approx 1$ (see Coey, 1999). The substitution of La by divalent ion leads to some change in the value of t. For example, for Sr^{2+} the ionic radii is equal to 0.144 nm, and the deviation of t from unity is relatively small. Doping results in an average change of the lattice parameters, which may be described by the average $\langle t \rangle_{\rm av}$. When the value of $\langle t \rangle_{\rm av}$ is close to one, the "cubic" perovskite structure is realized as a whole. At the same time, one must distinguish $\langle t \rangle_{\rm av}$ from its "local" value: two

materials may have close $\langle t\rangle_{\rm av}$, i.e. close lattice parameters, but the local distortions that are responsible for disorder, may differ strongly from one site to another.

Local disorder manifests itself in the value of residual resistance ρ_0. Experimentally, the residual resistances obtained for nominally the same compositions, may vary significantly for different samples. So, it is clear, that to some extent, the best values of $\rho_0(x)$ are still to be determined. As usual, the value of $\rho_0(x)$ also characterizes the sample's quality. This suggestion is supported by experiments performed by Quijada et al. (1998). They reported data for $La_{1-x}Sr_xMnO_3$ in crystalline films which give the value for $\rho_0(x)$ as low as $10^{-5}\,\Omega\,$cm. This is a typical metallic conductivity range. Making a substitution in Eq. (5.43) for $\pi\delta(\omega)\to\tau/(1+(\omega\tau)^2)$, we obtain in this case for the inverse life time $\hbar/\tau\sim 3\times 10^{-3}$ eV (~ 30 K). These findings become more transparent being expressed in terms of the mean free path. With the average velocity of an electron on the Fermi surface

$$\bar{u}=\langle v^2\rangle^{1/2}=(|A|a/\hbar)(2I_{\rm Dr}(x)/\tilde{v}(x))^{1/2}\ , \tag{5.50}$$

the mean free path, $l=\bar{u}\tau$ is typically $\sim$ 3a for materials with $\rho_0\sim 10^{-4}\,\Omega\,$cm, while in the best LSMO samples it is around $80a$ ($a\approx 3.8$ Å is the cubic lattice period). Whether the values of ρ_0 mentioned above may be or may be not improved by a more careful sample preparation process, remains to be seen. To the best of the authors knowledge, there was no systematic efforts specially aimed at this question. The band physics described above suggests an unifying view where materials may go from the metallic regime to the mobility edge and further with increase in disorder. For some current materials the conductivity regime seems to be close to the mobility edge. It is worth to repeat that if the short mean free path in these materials is an intrinsic feature, it may be related to the local fluctuations in the tolerance factor (5.49) caused by the difference in ionic radii at the Sr-doping.

5.8. Discussion

One concludes from the above that at least the low temperature properties of metallic ferromagnetic manganites can be adequately described by the two-band model. Of course, such two-band approach implies the validity of the Fermi liquid description of the metallic manganites. Some further evidences in favor of this suggestion follow from the analysis of the temperature dependent part of the resistivity. In ordinary metals, the resistivity behaves like $\rho(T)=\rho_0+AT^\alpha$, where ρ_0, the residual resistivity, is due to structure defects or impurities, while the T-dependence comes up either from scattering on thermal phonons or from electron–electron interactions. In the second case, the electronic relaxation rate $1/\tau_{\rm ee}\sim T^2/E_{\rm F}$, while the phonon mechanism with $1/\tau_{\rm ph}\sim T^3/\theta^2$ prevails ($1/\tau_{\rm ph}>1/\tau_{\rm ee}$) at $T>\theta(\theta/E_{\rm F})$ where θ is the characteristic phonon frequency. The latter in manganites is about 400 K, while $E_{\rm F}\approx 0.1$ eV. Hence, the electron mechanism of scattering might remain important up to rather high temperatures. At elevated temperatures a lot of new effects, related to the colossal magnetoresistance phenomenon, may start to play the dominating role, but at low temperatures the electron–electron channel should prevail.

The Fermi liquid description corresponds to the case when interactions are supposed not to be remarkably strong. The strength of interactions is characterized by the value of the T^2-term in resistivity, in which electron interactions come from $\hbar/\tau_{\rm ee}^{\rm tr}=\lambda'(\hbar/\tau_{\rm ee})$ where $\tau_{\rm ee}$ is the total quasiparticle relaxation time and $\lambda'<1$ gives the fraction of the Umklapp processes. One can write

$$\hbar/\tau_{\rm ee}\cong\lambda\pi^3\nu(x)T^2 \tag{5.51}$$

(see, e.g., in Gantmakher and Levinson, 1987). In (5.51) λ is a value of the interaction strength in terms of E_F, $\nu(x)$ is the density of states which depends on the doping level x. Using the data by Lofland et al., 1996, Quijada et al. (1998) and taking $\nu(x)$ from Fig. 8, one obtains for LSMO: $\lambda\lambda' \cong 0.3$, typical for most metals.

Note that Quijada et al. (1998) have also studied two other materials $Nd_{0.7}Sr_{0.3}MnO_3$ and $La_{0.7}Ca_{0.3}$-MnO_3. It turns out that the T-dependent part of resistivity scales in the magnitude with the residual resistivities of the compounds. Such a correlation, most probably, is caused by the very fact that the doping process itself creates defects (we will come back to it later again).

Indeed, as was noted above, the substitutional doping inevitable leads to a local structural disorder which can be described by the tolerance factor (5.49). The local disorder (local fluctuations in values of the tolerance factor) affect strongly the value of the residual resistance $\rho_o(x)$, see above, Section 5.6. It is remarkable, nevertheless, that in most cases the average value $\langle t \rangle_{av}$ remains reasonably close to one, so that the "cubic", perovskite structure is realized for the lattice as a whole and the above band picture is thus relevant. This is also confirmed by the fact the bandwidth $W = 6|A|$, see Eq. (5.18) does not vary significantly for various compositions. Indeed, for different compounds it lies in the range $W \cong 0.7$–1.0 eV as estimated from the experimental data on $D_{\text{stiff.}}$, the spin stiffness coefficient. This is in favor of the view that while the tolerance factor itself determines variations in the Mn–O–Mn bonds angle for different materials, the latter is not of much importance for the conduction network.

6. Metallic A-phase

6.1. Magnetic structure

In the previous chapter we discussed properties of the ferromagnetic metallic phase of manganites $A_{1-x}R_xMnO_3$. Such phase occupies the doping region $0.16 < x < 0.4$–0.5. The further increase in the carriers concentration leads to a noticeable change. As usual, we focus,mainly, on the $La_{1-x}Sr_xMnO_3$-materials (unless is specified otherwise). Analysis of the $La_{1-x}Sr_xMnO_3$ is simpler, because for this compound there are no complications related to the so-called "charge" ordering (see, e.g., Tokura, 2003; Cheong et al., 1994; Tokura et al., 1996; Ramirez et al., 1996; Tokunaga et al., 1998; Casa et al., 1999; Fukumoto et al., 1999). As usual, we concentrate on the low temperature region.

The study of $La_{1-x}Sr_xMnO_3$ (Akimoto et al., 1998; Tokura and Tomioka, 1999; Izumi et al., 2000) has led to a remarkable observation that the larger doping ($0.5 < x < 0.55$) gives rise to appearance of a metallic antiferromagnetic phase, the so-called A-phase. It was already mentioned in Section 2, that for the A-phase the core (t_{2g}) spins are aligned ferromagnetically in each MnO-plane (for example, ab-plane) and antiferromagnetically along the axis perpendicular to the planes (c-axis; Fig. 5). In the ferromagnetic phase all electrons including the e_{2g}-ones are fully polarized ("half-metallic" state). Now the "half-metallic" state is realized only inside of the each ab-plane of the A-phase.

Therefore, the magnetic A-structure combines the ferromagnetic order in the layers with antiferromagnetism in the c-direction. Such magnetic order leads to highly anisotropic transport, because the charge transfer in the c-direction is spin forbidden.

Note in passing that antiferromagnetism in the form of alternating ferromagnetically ordered planes is not specific for only the metallic phase with $0.5 < x < 0.55$. It turns out that the parent compound, $AMnO_3$, also has a similar magnetic structure. The parent material is an insulator, though, and we will

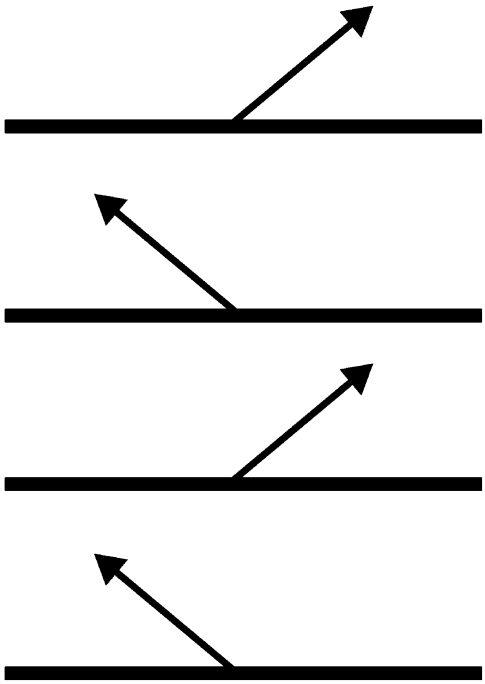

Fig. 10. Canted A-phase.

discuss its properties later, Section 7. It will be seen that the analysis of the insulating phase should be based on using the full Hamiltonian (4.4) and is comparatively more complicated than the one of the metallic phases. On that reason we postpone its discussion to the one of the last chapters.

6.2. *Energy spectrum of canted A-phase*

We start with the electronic energy spectrum for the A-phase. While in the A-phase itself the magnetization of neighboring ferromagnetic layers point out in the opposite directions, it turns out that the electronic energy spectrum can be found (in the double exchange approximation) for a more general and rather interesting case of the canted A-phase (Fig. 10). The band Hamiltonian describing the system with an antiferromagnetic ordering and ferromagnetic canting has a more complicated form than that one for the metallic ferromagnetic phase (Section 5). Namely

$$\begin{aligned}\hat{H} = &\sum_{\vec{p}} T^{\alpha\beta}(\vec{p})\hat{a}^{+}_{\alpha\sigma}(\vec{p})\hat{a}_{\beta\sigma}(\vec{p}) + J_H \sum_{\vec{p},\vec{Q}} S(\vec{Q})\hat{a}^{+}_{\alpha\sigma'}(\hat{\sigma}_z)_{\sigma'\sigma''}\hat{a}_{\alpha\sigma''}(\vec{p}-\vec{Q})\\ &+ J_H \sum_{\vec{p},\vec{Q}} S(-\vec{Q})\hat{a}^{+}_{\alpha\sigma'}(\vec{p})(\hat{\sigma}_z)_{\sigma'\sigma''}\hat{a}_{\alpha\sigma''}(\vec{p}+\vec{Q})\\ &+ J_H M \sum_{\vec{p}} \hat{a}^{+}_{\alpha\sigma'}(\vec{p})(\hat{\sigma}_x)_{\sigma'\sigma''}\hat{a}_{\alpha\sigma''}(\vec{p})\ . \end{aligned} \tag{6.1}$$

Here $T^{\alpha\beta}(p)$ is again the two-band electron hopping matrix, J_H is the Hund's coupling constant on the Mn sites, and S(Q) is the Fourier component of the AF parameter (staggered magnetization) along the c direction, $S_z(i) = \langle S_z\rangle(-1)^i$. The magnetic structural vector $Q = (0, 0, \pi/a)$ doubles the periodicity in the c-direction and, correspondingly, reduces the Brillouin zone (a is the cubic lattice constant); M is the canted magnetic moment per site, so that at each site i:

$$S(i) = (M_x, \pm\langle S_z\rangle), \quad S_z^2 + M_x^2 \approx S^2 \tag{6.2}$$

(when $S_z(Q) \equiv 0$ we restore the ferromagnetic phase). The orientations of M and S_z are fixed by magnetic anisotropy (easy plane) and/or by an external field. As before, the matrix elements $T^{\alpha\beta}(p)$ in (6.1) are calculated with the basis functions in the form (5.2). The hopping matrix is given by Eq. (5.7) with $|A| \cong 0.16$ eV being the hopping amplitude (see Eq. (5.14)).

From (6.1) we obtain the following equation of motion:

$$\begin{aligned}(E\delta_{\alpha\beta} - T^{\alpha\beta}(\vec{p}))\hat{a}_{\beta\sigma}(\vec{p}) \\ = J_H S(\vec{Q})(\hat{\sigma}_z)_{\sigma,\sigma'}\hat{a}_{\alpha\sigma'}(\vec{p} - \vec{Q}) + J_H M S(\hat{\sigma}_x)_{\sigma,\sigma'}\hat{a}_{\alpha\sigma'}(\vec{p})\end{aligned} \tag{6.3}$$

and a similar equation with $\vec{p} \to \vec{p} + \vec{Q}$. Thus, the secular equation is now an 8×8 determinant from which one must calculate not only eigenvalues but also the eigenvectors to be able to evaluate various physical properties. Recall (Section 3) that the double exchange (DE) mechanism for manganites exploits the large value of the Hund interaction, $J_H \approx 1$–1.5 eV, assuming $J_H/|A| \gg 1$.

Using this approximation, one can solve Eq. (6.3) up to the terms of order A^2/J_H. Because of the large J_H value, electrons can occupy only four lowest bands:

$$\begin{aligned}E_{1,2}(\vec{p}; M/S) &= -J_H S - |A| \cdot [c_x + c_y + (M/S)c_z \pm R_{12}(\vec{p}; M/S)] \ , \\ E_{3,4}(\vec{p}; M/S) &= -J_H S - |A| \cdot [c_x + c_y - (M/S)c_z \pm R_{34}(\vec{p}; M/S)] \ ,\end{aligned} \tag{6.4}$$

where

$$\begin{aligned}R_{12}(\vec{p}; M/S) &= \sqrt{c_x^2 + c_y^2 + (M/S)^2 c_x^2 - (M/S)c_z(c_x + c_y) - c_x c_y} \ , \\ R_{34}(\vec{p}; M/S) &= R_{12}(\vec{p}; -M/S)\end{aligned} \tag{6.5}$$

(we used notations (5.8)).Therefore, the spectrum described by Eqs. (6.4) contains several branches.

We have demonstrated that it is possible to write down the analytical expression (Eqs. (6.4), (6.5)) for the spectrum of such a complex system as the canted A-structure of manganites. Based on this expression, one can calculate conductivity and magneto-transport (see below, Section 6.3).

In the absence of canting ($M = 0$) the general expression (6.4) becomes 2D, i.e. depends on (x, y) only and simplifies significantly. Indeed, because the number of carriers is less than one per unit, the electrons can occupy only two lowest bands:

$$E_{1,2} = -J_H - |A|(c_x + c_y \pm R) \ , \tag{6.6}$$

$$R = (c_x^2 + c_y^2 - c_x c_y)^{1/2} \ . \tag{6.7}$$

In the presence of canting Eqs. (6.4), (6.5) lead to a much more complicated structure of the spectrum. Let us remind here that in Eqs. (6.4)–(6.7), small terms of order $\approx t^2/J_H$ are neglected.

As a next step, one should construct the eigenstate vectors which correspond to the eigenvalues (6.4). Performing the canonical transformation while making use of eigenvalues of (6.4), it is straightforward to express the operators in (6.1) in terms of new eigenfunctions. Quite generally, the canonical transformation has the form

$$\hat{\alpha}_{\alpha\sigma}(\vec{p}) = \sum_{l=1}^{\infty} K_{\alpha\sigma}^{(l)}(\vec{p}) \cdot \hat{\varsigma}_l(\vec{p}) \ , \tag{6.8}$$

where $\hat{\varsigma}_l^+(p), \hat{\varsigma}_l(p)$ are the creation and annihilation operators for the true energy branches (6.4) and $\sigma \equiv (\uparrow\downarrow)$. Below we write down explicitly the expressions for $K_{\alpha\sigma}^{(t)}$ for the four lowest bands:

$$\begin{aligned}
K_{1\sigma}^{(1)}(\vec{p}) &= K_{1\sigma}^{(2)}(\vec{p}) = \frac{1}{2}\left(1+\frac{M}{S}\right)^{1/2}\left(\frac{\sum_{12}(\vec{p})}{2R_{12}(\vec{p})}\right)^{1/2} \ , \\
K_{2\sigma}^{(1)}(\vec{p}) &= -K_{2\sigma}^{(2)}(\vec{p}) = \frac{1}{2}\left(1+\frac{M}{S}\right)^{1/2}\left(\frac{\sum_{12}^{*}(\vec{p})}{2R_{12}(\vec{p})}\right)^{1/2} \ , \\
K_{1\uparrow}^{(3,4)}(\vec{p}) &= -K_{1\downarrow}^{(3,4)}(\vec{p}) = \frac{1}{2}\left(1-\frac{M}{S}\right)^{1/2}\left(\frac{\sum_{34}(\vec{p})}{2R_{34}(\vec{p})}\right)^{1/2} \ , \\
K_{2\uparrow}^{(3,4)}(\vec{p}) &= -K_{2\downarrow}^{(3,4)}(\vec{p}) = \pm\frac{1}{2}\left(1-\frac{M}{S}\right)^{1/2}\left(\frac{\sum_{34}^{*}(\vec{p})}{2R_{34}(\vec{p})}\right)^{1/2} \ ,
\end{aligned} \tag{6.9}$$

where the following notations have been used:

$$\begin{aligned}
\sum\nolimits_{12}(\vec{p}) &= (M/S)c_z - \frac{1}{2}(c_x + c_y) + \mathrm{i}\,\frac{\sqrt{3}}{2}(c_y - c_x) \ , \\
\sum\nolimits_{34}(\vec{p}) &= -(M/S)c_z - \frac{1}{2}(c_x + c_y) + \mathrm{i}\,\frac{\sqrt{3}}{2}(c_y - c_x) \ .
\end{aligned} \tag{6.10}$$

6.3. *Conductivity and magneto-conductivity of canted A-phase*

The compounds under discussion display anisotropic metallic conductivity, and this metallic behavior has been observed experimentally in the best LaSrMnO samples (see, e.g., Tokura and Tomioka, 1999). At the same time, and this was already stressed above, the conductivity in manganites manifests that peculiar feature which makes manganites somewhat different from usual metals, namely a tight correlation between disorder and the carrier concentration. In manganites, although they may possess a typical metallic behavior, the carrier concentration is determined by doping. This correlation especially affects these transport properties, that in the low temperature region are determined, mainly, by scattering on defects.

The conductivity in metals due to scattering on defects is usually calculated with use of the "cross" technique (Abrikosov et al., 1975). One can extend the technique to include static defects in the two-band model. As for the nature of the defects, note when an ion R is substituted for an ion A in the unit formula $A_{1-x}R_xMnO_3$, this immediately lifts the cubic symmetry at the Mn-sites. The e_{2g}-doublets get split and the oxygen octahedron becomes distorted (with the Jahn–Teller type of distortions playing the major role). Since this effect is of prime importance for the Mn–O–Mn conduction network, disorder in manganites

to a large extent comes about through a variation in the doping. In the application of diagrammatic cross-technique below, however, we consider "scattering" centers as point "impurities" (i.e., of the R ions) with random positions, neglecting correlation between the scattering processes stemming from forming oxygens' clusters. The specifics of defects in manganites is partially accounted for by the form of the "impurity" potential $U_{\alpha\beta}(r - R_i)$

$$\hat{H}_{\rm imp} = \sum_i \int {\rm d}^3\vec{r}\, \Psi^+_{\alpha\sigma}(\vec{r}) U_{\alpha\beta}(\vec{r} - \vec{R}_i)\Psi_{\beta\sigma}(\vec{r}) \tag{6.11}$$

(where the summation runs over all random realizations of the "impurities"). However, one assumes the Jahn–Teller form for the defect potential. Using the basis given by (5.2), the expression for $U_{\alpha\beta}$ is

$$U_{\alpha\beta}(\vec{r} - \vec{R}_i) = g\,Q(\vec{R}_i)\cdot \begin{pmatrix} 0 & {\rm e}^{{\rm i}\theta_i} \\ -{\rm e}^{{\rm i}\theta_i} & 0 \end{pmatrix}_{\alpha\beta} \cdot \delta(\vec{r} - \vec{R}_i)\ , \tag{6.12}$$

where $Q(R_i)$ is an amplitude of the Jahn–Teller distortion at site i. Here g is an electron–lattice coupling constant and the angle θ_i specifies the shape of the distorted octahedron at a given Mn site. For instance, the angle $\theta_i = 0$ corresponds to elongation of the octahedron along the z-axis (see below, Section 7.2). In the momentum representation, the expression for $\hat{H}_{\rm imp}$ is

$$\hat{H}_{\rm imp} = \sum_i \int\int \frac{{\rm d}^3\vec{p}}{(2\pi)^3}\frac{{\rm d}^3\vec{p}'}{(2\pi)^3}\,\hat{a}^+_{\alpha\sigma}(\vec{p}) U_{\alpha\beta}(\vec{p} - \vec{p}')\hat{a}_{\beta\sigma}(\vec{p}')\cdot {\rm e}^{{\rm i}(\vec{p}-\vec{p}')\cdot\vec{R}_i}\ , \tag{6.13}$$

with

$$U_{\alpha\beta}(\vec{p}) = \int {\rm d}^3\vec{r} U_{\alpha\beta}(\vec{r})\cdot {\rm e}^{-{\rm i}(\vec{p}-\vec{r})}\ .$$

Keeping in mind the energy spectrum obtained in the preceding section it is helpful to re-write expression (6.13) in terms of the new variables defined by (6.8):

$$\begin{aligned}\hat{H}_{\rm imp} = {} & \sum_i g\,Q(\vec{R}_i)\int\int \frac{{\rm d}^3\vec{p}}{(2\pi)^3}\frac{{\rm d}^3\vec{p}'}{(2\pi)^3}\sum_{l_1,l_2=1}^{4} M^{(l_1,l_2)}(\vec{p},\vec{p}',i) \\ & \times \hat{\varsigma}^+_{l_1}(\vec{p}) u(\vec{p} - \vec{p}')\hat{\varsigma}_{l_2}(\vec{p}')\,{\rm e}^{{\rm i}(\vec{p}-\vec{p}')\cdot\vec{R}_i} \\ M^{(l_1 l_2)}(\vec{p},\vec{p}';i) \equiv {} & \sum_{\sigma=(\uparrow\downarrow)} \left\{ K^{(l_1)^*}_{1\sigma}(\vec{p})\cdot K^{(l_2)}_{2\sigma}(\vec{p}')\,{\rm e}^{{\rm i}\theta_i} + K^{(l_1)^*}_{2\sigma}(\vec{p})\cdot K^{(l_2)}_{1\sigma}(\vec{p}')\,{\rm e}^{-{\rm i}\theta_i}\right\}\ . \end{aligned} \tag{6.14}$$

The so-called "cross-technique" can now be straightforwardly applied to the calculation of the average of new band Green function given by

$$G_l(\vec{p},\vec{p}';t) = -{\rm i}\langle \hat{T}\{\hat{\varsigma}_l(\vec{p};0)\hat{\varsigma}^+_l(\vec{p}'t)\}\rangle. \tag{6.15}$$

In the absence of the defects, the Green function (6.15) is

$$G^{(0)}_l(\vec{p};\varepsilon) = \frac{1}{\varepsilon - \xi_l(\vec{p}) + {\rm i}\,{\rm sign}(\varepsilon)}\ , \tag{6.16}$$

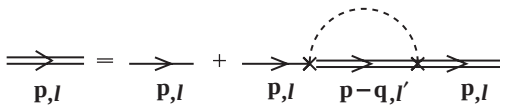

Fig. 11. The diagrammatic equation for an averaged over defect Green's function (6.15). Summation over l' and integration over $\vec{q}$ are assumed.

where $\xi_l(p) = E_l(p) - E_F$ (again we can leave only four essential bands, since $J_H \gg |A|$). For the Green function averaged over defect's positions:

$$\langle G(\vec{p};\vec{p}';\varepsilon)\rangle_{\rm dis} = G(\vec{p};\varepsilon)\cdot\delta(\vec{p}-\vec{p}')\ , \tag{6.17}$$

we obtain the well-known form of the Dyson equation. The self-energy part $\hat{\sum}_l(\varepsilon)(\vec{p}-\vec{q};\varepsilon)$ in Fig. 11 may be again expressed in terms of the corresponding relaxation times as

$$\hat{\sum}_l(\varepsilon) = -{\rm i}\,{\rm sign}\,\varepsilon\left\langle\frac{\hbar}{2\tau_l(\vec{p})}\right\rangle_{\rm F.S.} \tag{6.18}$$

where $\langle\ldots\rangle_{\rm F.S.}$ denotes an average over the Fermi surface. Let us emphasize that the attenuation τ_l^{-1} in (6.18) contains contributions from scattering between different bands (6.4). In the representation (6.14), the expressions for relaxation times $\hbar/2\tau_l$ are

$$\begin{aligned}\frac{\hbar}{2\tau_l} &= \pi\frac{|gQ|^2}{2v_l(E_F)}n_{\rm imp}\int\frac{{\rm d}^3\vec{p}}{(2\pi)^3}\int\frac{{\rm d}^3\vec{p}'}{(2\pi)^3}\sum_{l_1=1}^{4}M^{(ll_1)}(\vec{p},\vec{p}')\\ &\quad\times\ \delta(E_F-E_{l_1}(\vec{p}'))M^{(l_1l)}(\vec{p}',\vec{p})\delta(E_F-E_l(\vec{p}))\ ,\\ M^{(l_1l_2)}(\vec{p},\vec{p}') &\equiv \sum_{\sigma=(\uparrow,\downarrow)}\left\{K_{1\sigma}^{(l_1)*}(\vec{p})K_{2\sigma}^{(l_2)}(\vec{p}')+K_{2\sigma}^{(l_1)*}(\vec{p})K_{1\sigma}^{(l_2)*}(\vec{p}')\right\}\ ,\end{aligned} \tag{6.19}$$

where $n_{\rm imp}$ is the concentration of "impurities"; $v_l(E_F)$ is the density of states at the Fermi level for the lth band. In the process of deriving (6.19), we took into account the fact that the main contribution to the integrals (6.19) comes from the region close to the Fermi surface. We also used the following averages over disorder:

$$\langle(gQ(\vec{R}_i))^2\rangle_{\rm dis} = |gQ|^2,\quad \langle{\rm e}^{2{\rm i}\theta_i}\rangle_{\rm dis} = 1\ ,$$

where the second expression means averaging over all local orientations of distorted octahedra.

With the use of (6.18) and (6.19), the expression for the averaged Green function (6.17) can be written in the form

$$\langle G_l(\vec{p};\vec{p}';\varepsilon)\rangle_{\rm dis} = \delta(\vec{p}-\vec{p}')\cdot\frac{1}{\varepsilon-\xi_l(\vec{p})+{\rm i}(\hbar/2\tau_l)\,{\rm sign}\,\varepsilon}\ . \tag{6.20}$$

The DC-conductivity can be calculated from the Kubo formula

$$\theta_{\alpha\alpha}(0) = \lim_{\omega\to0}\frac{R_{\alpha\alpha}(\omega)}{{\rm i}\omega}\ , \tag{6.21}$$

where $R_{\alpha\alpha}(\omega)(a = x, y, z)$, can be obtained with the help of the corresponding product of retarded Green functions, averaged over impurities:

$$(R_{\alpha\alpha}(\omega))_{\rm dis} = \frac{-{\rm i}e^2\hbar}{(2\pi)} \int_{-\infty}^{\infty} {\rm d}\varepsilon \sum_l \int\int \frac{{\rm d}^3\vec{p}}{(2\pi)^3} \frac{{\rm d}^3\vec{p}'}{(2\pi)^3} \times l\langle(\hat{v}_\alpha^{(l)}\hat{G}_l(\vec{p}, \vec{p}'; \varepsilon + \omega))(\hat{G}_l(\vec{p}', \vec{p}; \varepsilon)\hat{v}_\alpha'^{(l)})\rangle_{\rm dis} , \tag{6.22}$$

via analytic continuation $R_{\alpha\alpha}({\rm i}\omega_n) \to R_{\alpha\alpha}(\omega + {\rm i}\delta)$. In (6.22), $\hat{v}_\alpha^{(l)}$ is the velocity operator defined as a derivative of energy with respect to the momentum for each band given by (6.4). With the impurity potential given by (6.12) and (6.13), the average of product in expression (6.22) can be re-written as

$$\langle\hat{v}_\alpha^{(l)}\hat{G}_l(\vec{p}, \vec{p}'; \varepsilon + \omega) \cdot \hat{G}_l(\vec{p}', \vec{p}; \varepsilon)\hat{v}_\alpha'^{(l)}\rangle_{\rm dis} = \hat{v}_\alpha^{(l)}\langle\hat{G}_l(\vec{p}, \vec{p}'; \varepsilon + \omega)\rangle_{\rm dis}\langle\hat{G}_l(\vec{p}', \vec{p}; \varepsilon)\rangle_{\rm dis}\hat{v}_\alpha'^{(l)} . \tag{6.23}$$

Now, taking into account Eqs. (6.17)–(6.23) and performing the integration in (6.22) with respect to ε, we finally obtain the following expression for the in-plane and out-of-plane DC-conductivities:

$$\sigma_{xx} = \sigma_{xx}^{(+)} + \sigma_{xx}^{(-)} ,$$
$$\sigma_{zz} = \sigma_{zz}^{(+)} + \sigma_{zz}^{(-)} , \tag{6.24}$$

where

$$\sigma_{\alpha\alpha}^{(+)} = (1 + M/S)^2 \cdot \frac{e^2}{\hbar} \int_{\rm F.S.} \sum_{l=1}^{2} \frac{\tau_l}{\hbar} \cdot \frac{{\rm d}S_{\vec{p}}^l}{|\nabla_{\vec{p}} E_l|} \left(\frac{\partial E_l(\vec{p})}{\partial \vec{p}_\alpha}\right) ,$$

$$\sigma_{\alpha\alpha}^{(-)} = (1 - M/S)^2 \cdot \frac{e^2}{\hbar} \int_{\rm F.S.} \sum_{l=1}^{2} \frac{\tau_l}{\hbar} \cdot \frac{{\rm d}S_{\vec{p}}^l}{|\nabla_{\vec{p}} E_l|} \left(\frac{\partial E_l(\vec{p})}{\partial \vec{p}_\alpha}\right) , \tag{6.25}$$

and $\hbar/\tau_l$ $(l = 1, 2, 3, 4)$ are defined by (6.19), $\alpha = (x, z)$ and integration runs over each sheet of the Fermi surface.

Expressions (6.25) for both in-plane and out-of-plane conductivities are rather complicated and the procedure of evaluating the conductivity by using them deserves a further explanation. Parameters of the electronic spectrum are chosen to be the same as in the two-band "cubic" phase which, as we believe, realizes itself in the ferromagnetic state. Let us also recall that the disorder in the calculations presented above expresses itself through the local octahedra distortions which, in turn, are a result of the substitutional disorder, i.e. non-stoichiometry of $A_{1-x}R_xMnO_3$. Therefore, in (6.25) the "concentration" of "impurities" is the concentration of R atoms, while the amplitude of the disorder potential is given by the value of $|gQ|$ in (6.19). A change in the composition by increasing x decreases the number of carriers, $1 - x$, at the same time, while increasing simultaneously the number of defects. The most significant oversimplification above was that distortions of the oxygen octahedra caging a Mn-ion were treated independently. This looks as a reasonable good approximation, because two octahedra surrounding two neighboring Mn atoms share one oxygen atom only. If octahedra were fully independent, the values of resistivity would depend on the B atom concentration only. In reality a sample's quality also depends on how distorted octahedra adjust themselves on neighboring sites. Therefore, the factor $n_{\rm imp}$ in (6.19) is,

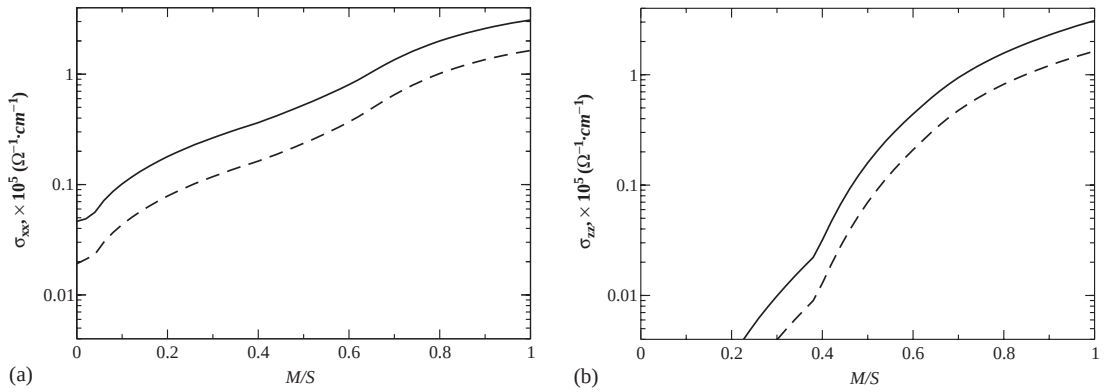

Fig. 12. (a) In-plane and (b) out-of-plane conductivities in the canted A-phase as a function of M/S. Solid line corresponds to $\Delta = 0.45$; dashed line corresponds to $\Delta = 0.75$; $\Delta = |gQ|/|A|$. Dopant concentration $x = 0.55$, $a = 3.9$ Å.

strictly speaking, not the only way for the conductivity to depend on x in (6.25). In addition, a change in carrier concentration results in a shift of the chemical potential relative to the bottom of the bands which reflects itself in an immediate change in the occupation number in each of the four active energy bands (6.4). Such a non-trivial intimate dependence between the number of carriers and the number of defects presents itself as a new feature for conductivity behavior in manganites. It would be of great interest to investigate significance of each of those trends experimentally. Currently a shortage of experimental data for LSMO compounds for large enough Sr concentrations deprives us the possibility to trace the x-dependence of conductivity in more details. Some estimates have been done for the FM-phase above, Section 6, for $x \approx 0.3$–0.4. Here we focus on the calculations of the conductivity tensor for canted A-phase at $x \approx 0.55$. The results are plotted in Fig. 12.

Energy spectrum of the A-phase itself, in the double exchange approximation ($J_H \gg |A|$), would not allow current to flow in the perpendicular to-plane direction: the dispersion $t(p_z) \infty \cos(p_z)$ drops out from the electron spectrum (6.4) at $M = 0$. Therefore Fig. 12 describes, as expected, a dramatic magneto-resistance effect inherent to the canted A-phase for the perpendicular-to-the-plane conductivity (σ_{zz}). Surprisingly, it turned out that even the in-plane (σ_{xx}) components of conductivity display considerable change in its value at the transition from the 3D conductivity regime in the ferromagnetic state (i.e. at $M/S = 1$) to the 2D one for the pure A-phase ($M = 0$). The origin of such a rapid change comes about from the re-distribution of carriers between the energy bands with variation in the value of M/S. The effect of carrier re-distribution between the bands is seen in Fig. 13 which shows the calculated position of the Fermi level as a function of M/S for doping concentration $x \approx 0.55$. With a variation of M/S the system undergoes dimensional transition between the 2D and 3D conductivity regimes.

In Figs. 12(a) and (b), it seemed more convenient to present our results for the chosen concentration as a function of M/S in accordance with (6.25). We remind that M is a ferromagnetic component of the core spins only. In order to find the values of conductivity as a function of the total magnetization induced by an external magnetic field, $M_{\text{tot.}}$, which also includes the "half-metallic" electronic component, one may use the following simple relation

$$M_{\text{t}} = \mu_{\text{B}}(4 - x)(M/S) \ . \tag{6.26}$$

Eq. (6.26) expresses the value of the full magnetic moment.

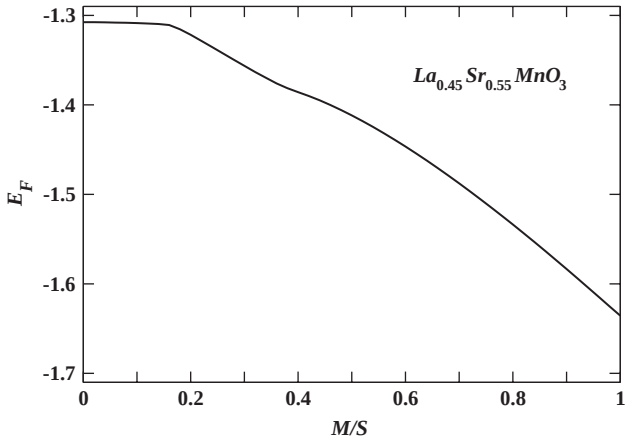

Fig. 13. The dependence of E_F on M/S for a given concentration. $x = 0.55$ based on band structure described by (6.4). E_F is given in the units of the hopping amplitude $|A|$. The reference point for the Fermi level is taken at the bottom of the lowest band.

At low temperature $M_{\text{tot.}} = \chi B$, in units of Bohr magneton per Mn ion, and χ is the magnetic susceptibility in these units. Everywhere above we neglected relatively small terms responsible for the magnetic anisotropy in manganites.

7. Insulating phase

7.1. Parent compound

The parent compound $AMnO_3$, e.g., $LaMnO_3$ is an insulator and antiferromagnet. In addition, it has magnetic A-structure (see above, Section 2 and Fig. 5) with relatively low Neel temperature ($T_N \approx 140$ K). All these properties (insulating behavior, A-structure, small value of T_N) demand for an explanation. It turns out, as shown below, that even the properties of parent manganite can be understood in the framework of the two-band picture (Gor'kov and Kresin, 1998; Dzero et al., 2000). Therefore, the band approach represents an unified description of the low temperature properties of manganites, applicable to all phases (metallic and insulating).

Let us, first, make several preliminary remarks. The "right" stoichiometric end ($x = 1$) of the phase diagram for the $A_{1-x}R_xMnO_3$ compound, that is, e.g., for $SrMnO_3$, is also an insulator, and this is not surprising. Indeed, in this case all manganese ions are Mn^{4+}, the itinerant e_{2g} electrons are absent, and the ions contain only the strongly bound t_{2g} groups. The magnetic properties are then determined by an effective Heisenberg Hamiltonian commonly attributed to the superexchange mechanisms along the Mn–O–Mn bonds (the Hamiltonian itself may be constructed following by the so-called Anderson–Goodenough–Kanamori rules" (see, e.g., Goodenough, 1963).

The situation with the parent compound, $AMnO_3$ (the "left" side of the phase diagram, $x = 0$) is entirely different, because of presence of loosely bound e_{2g}-electrons. These electrons are responsible for metallic conductivity in the doped manganites; this was discussed briefly in Section 2 and in more detail in Section 4. Nevertheless, despite of the presence of such electrons, the parent material behaves

as an insulator. One can show (see below) that the two-band picture introduced above (Section 4) but extended to incorporate the complete Hamiltonian (4.4), i.e., including the Jahn–Teller effect, allows us fully understand the insulating ground state.

One remark more. One might think that this limiting case ($x=0$) should be treated also, like $x=1$, in the framework of localized picture; this would mean that the Mn^{3+} e_{2g}-shells should behave as localized e_{2g}-orbitals. And, indeed, the pertinent properties of manganites are often interpreted in terms of generalized microscopic Hubbard model (see, e.g., Kugel and Khomskii, 1973). The key feature of the Hubbard model is the assertion that for two electrons to be placed on the same site the energy cost is very high (the famous Hubbard "U">0 due to the on-site Coulomb repulsion!). The Hubbard Hamiltonian approach has been challenged by Gor'kov and Kresin (1998), see also Dzero et al. (2000). First, there are experimental motivations for such challenge. For instance, it was shown experimentally that in doped manganites, $La_{1-x}Sr_xMnO_3$, at rather low concentrations, say, $x=0.2$, the system may display excellent metallic behavior at low temperatures (Urushibara et al., 1995). Meanwhile, the nominal number of e_{2g}-electrons per Mn site, $N=1-x<1$, was changed only by one fifth in this study. In addition, from the theoretical view, it is, of course, clear that dealing with the strictly atomic d-orbitals would be a strong oversimplification. If a Mn ion is placed into the oxygen octahedron environment, the e_{2g}-terms are formed by the whole ligand, so that the "pure" d-functions become considerably hybridized with the surrounding oxygen states (e.g., see the discussion by Anderson, 1959, and by Pickett and Singh, 1996). Hence the electronic polarization would undoubtedly reduce the magnitude of the "Hubbard"-like (on-site) interactions. Recall also, and this was stated above (Section 4) that the Jahn–Teller instability also makes unfavorable the situation when two electrons occupy the same site. Finally, for the Jahn–Teller effect (which itself is nothing but another form of the Coulomb interaction) to come up there is no need to use the Mn^{3+} localized states picture as it will be seen from what is done below. The JT effect in manganites may result into the new collective ground state, though.

Therefore, in what follows, we adopt the band approach to describe the ground state of $LaMnO_3$. This approach rationalizes the major features of an insulating state in $LaMnO_3$ very well and merges into metallic state of "doped" manganites (see Section 5).

7.2. Insulating state; qualitative picture

Let us describe initially the band insulator qualitatively. The parent compound, $AMnO_3$, has magnetically the A-structure (Fig. 5), that is, the neighboring layers have an opposite magnetization. As a result, the transport would have a 2D nature, since the hopping in the c-direction is spin-forbidden. Each 2D unit cell contains one delocalized electron. In the usual one-band picture such system would stay metallic, since at the Pauli band filling the electrons will occupy a half of the band. However, the double exchange mechanism in cooperation with large value of J_H makes all electrons have only one spin direction. Therefore, a single band in a "half-metallic" picture would be fully occupied. However, in manganites e_{2g}-electrons occupy not one, but two bands. If we neglect the JT term, the spectrum will be described by Eq. (5.14) and this should lead again to a metallic, not insulating state. Therefore, the analysis, based on the Hund's (DE) and hopping terms only, is not sufficient, since it would produce the metallic state. Things get different if one takes into account static deformations, caused by the JT interaction. Indeed, as the result, the "superstructure" imposed by the JT deformations, as shown in Fig. 6, makes the 2D Brillouin zone now be double-folded, i.e., reduced by a factor of two. After superlattice is imposed at the JT collective transition, the same number of electrons may completely fill up the reduced Brillouin

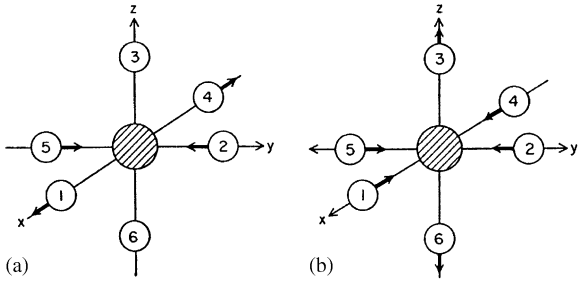

Fig. 14. (a), (b) The normal modes Q_2 and Q_3.

zone, producing an insulator *provided new sub-bands are separated from each other by proper gaps in the energy spectrum.*

7.3. Parent compound. Band structure

Let us derive the band energy spectrum of the parent manganite. The approach below (Gor'kov and Kresin, 1998) is based on the full Hamiltonian (4.4) where, in addition to the part that was analyzed for metallic phases (Sections 5 and 6), the JT term is explicitly included in the treatment to account for the presence of the static JT distortion (cooperative JT effect).

The JT term (Eq. (4.3)) contains the active JT normal modes for deformation of the surrounding oxygen octahedron. These modes are denoted in literature (Kanamori, 1961; Kugel and Khomskii, 1982) as Q_2 and Q_3 (Fig. 14) and can be expressed in terms of the Cartesian displacements of oxygen ions:

$$Q_2 = \frac{1}{\sqrt{2}}\,(x_1 - x_4 + y_5 - y_2)\ ,$$

$$Q_3 = \frac{1}{\sqrt{6}}\,(2z_2 - 2z_6 - x_1 - x_4 - y_2 + y_5)\ . \tag{7.1}$$

Another way is to use the basic set (5.2) and to write the JT term down in the following convenient form:

$$-\frac{g}{2}\,Q_0 \begin{pmatrix} 0 & \exp(\mathrm{i}\theta) \\ \exp(-\mathrm{i}\theta) & 0 \end{pmatrix}\ , \tag{7.2}$$

where in the standard notations:

$$Q_2 = Q_0 \sin\theta;\quad Q_3 = Q_0 \cos\theta \tag{7.3}$$

with Q_0 being the magnitude of the JT-distortions. The "angle", θ, specifies the shape of the octahedrons distortion (Fig. 15). Thus, the angles $\theta = 0;\ \pm 2\pi/3$ correspond to elongation of the octahedron along the *z*, *x* and *y* axes, respectively. The JT-term (4.3) is linear in *Q*, while the elastic energy is quadratic in *Q*. Therefore, if one electron is placed on the JT-level, the site energy always decreases with non-zero lattice deformations. Note, however, that deformations, Q_i, on the two adjacent manganese sites are not independent because the two sites share one oxygen along the Mn–O–Mn bond. The local distortions on neighboring sites must, therefore, be properly adjusted. In other words, in a lattice only cooperative JT distortions are possible.

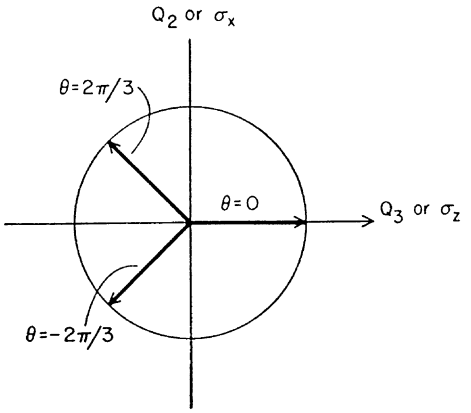

Fig. 15. The $Q_2 Q_3$ plane.

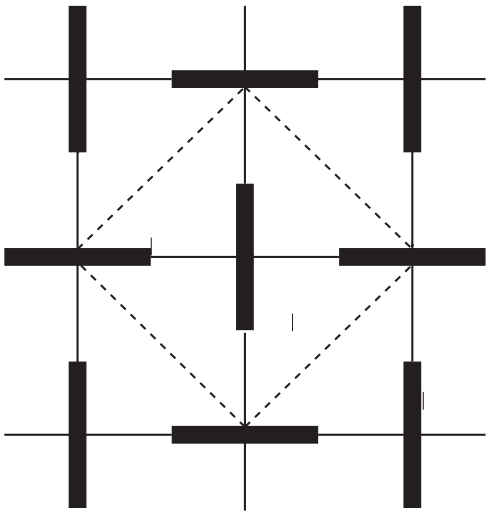

Fig. 16. In-plane staggered distortion inside the ferromagnetic layer. Solid segments represent the elongation of octahedra. The new unit cell is shown as the dashed square.

To calculate the electronic spectrum of our model in the presence of such "antiferrodistortive" JT collective deformations as shown in Fig. 16, see also Fig. 6; note that the 2D structure vector of the superlattice is $\vec{q} = (\pi/a)(1; 1)$. The superstructure modulation shows up through the JT-term (7.2) and depends on which of the two modes $(Q_2; Q_3)$ (or even their superposition) is chosen for the JT local deformations on each of the two sublattices. Experimentally, the arrangement in Fig. 16 is close to the one in which octahedra are elongated alternatively along each *x*- or *y*-axis preserving the overall tetragonal symmetry in the perpendicular plane (Coey et al., 1999; Ramirez, 1997). For that mode the number of "short legs" Mn–O per each octahedron equals four and the "long" ones equals two (these deformations were also seen even above percolative threshold in doped materials; see, e.g., Lousa and Egami, 1999a, b). Alterations in the octahedra orientations of that specific type would be reflected in expression

(7.3) as changes from $\theta = 2\pi/3$ to $-2\pi/3$ between the two sublattices. In such most general terms the secular equation for the new band structure cannot be solved in the analytic form. However, to describe the experiment it is enough to consider the energy contribution, which comes from the Q_2 mode only; these deformations are the ones shown in Fig. 14. For that pattern the Hamiltonian $H_{\rm JT}$ can be written as

$$\hat{H}_{\rm JT}(q) = -\frac{gQ_0}{2}\,\exp(\mathrm{i}\vec{q}\vec{r})\begin{pmatrix}0 & 1\\ 1 & 0\end{pmatrix} = -\frac{gQ_0}{2}\,\exp(\mathrm{i}\vec{q}\vec{r})\hat{\tau}_x\ , \tag{7.4}$$

($\hat{\tau}_x$ is a "pseudospin" Pauli matrix defined on basis (5.2)).

As was explained above, due to the magnetic A-structure and prevailing role of DE mechanism, the problem of finding the energy spectrum becomes two-dimensional. Writing explicitly

$$[\hat{\varepsilon} - \hat{t}(\vec{p})]\psi_{\vec{p}} = -\frac{gQ_0}{2}\,\hat{\tau}_x\psi_{\vec{p}+\vec{q}}\ ,$$

$$[\hat{\varepsilon} + \hat{t}(\vec{p})]\psi_{\vec{p}+\vec{q}} = -\frac{gQ_0}{2}\,\hat{\tau}_x\psi_{\vec{p}} \tag{7.5}$$

(the vector $\vec{q} = \pi/2(1,1)$; $\vec{p}$ is a vector in the new 2D Brillouin zone; by definition $t(\vec{p}+\vec{q}) = -t(\vec{p})$), $\varepsilon = E + J_H S$. After eliminating ψ_{p+q} from Eqs. (7.5), one obtains

$$[\varepsilon\hat{\tau}_x + \hat{\tilde{t}}(\vec{p})][\varepsilon\hat{\tau}_x - \hat{\tilde{t}}(\vec{p})](\hat{\tau}_x\psi_{\vec{p}}) = \left(\frac{gQ_0}{2}\right)^2\hat{\tau}_x\psi_{\vec{p}}\ . \tag{7.6}$$

The spectrum branches are then obtained from the zeroes of the two-by-two determinant:

$$\det|[\hat{e}^2 - (gQ_0/2)^2]\hat{e} - \hat{\tilde{t}}(p)^2 + \varepsilon[\hat{\tilde{t}}(p), \hat{\tau}_x]| = 0\ , \tag{7.6$'$}$$

where $\hat{e}$ is the unit matrix, $\hat{\tilde{t}}(p) = t(\vec{p})\hat{\tau}_x$, and

$$[\hat{\tilde{t}}(p), \hat{\tau}_x] = \hat{t}(\vec{p}) - \hat{\tau}_x t(\vec{p})\hat{\tau}_x\ .$$

With $\hat{t}(\vec{p})$ expressed in terms of the "pseudospin" Pauli matrices:

$$\hat{t}(\vec{p}) = -f_+(\vec{p})\hat{e} + \frac{1}{2}\,f_+(\vec{p})\hat{\tau}_x + \frac{\sqrt{3}}{2}\,f_-(\vec{p})\hat{\tau}_y\ , \tag{7.7}$$

where

$$f_+(\vec{p}) = |A|(c_x + c_y); \quad f_-(\vec{p}) = |A|(c_x - c_y)\ ,$$

after simple calculations, determinant (7.6) transforms to the form

$$\begin{vmatrix} \varepsilon^2 - (gQ_0/2)^2 - (5/4)f_+^2 + (3/4)f_-^2 + \mathrm{i}(\sqrt{3}/2)f_+f_-;\ f_+^2 - \mathrm{i}\varepsilon\sqrt{3}f_- \\ f_+^2 + \mathrm{i}\varepsilon\sqrt{3}f_-;\ \varepsilon^2 - (gQ_0/2)^2 - (5/4)f_+^2 + (3/4)f_-^2 - \mathrm{i}\varepsilon(\sqrt{3}/2)f_+f_- \end{vmatrix} = 0\ .$$

The resulting bi-quadratic equation produces the following four branches, $\varepsilon_i(\vec{p})$ $i = 1 \ldots 4$):

$$\varepsilon_{1;2}(\vec{p}) = \left\{(gQ_0/2)^2 + (5/4)f_+^2 + (3/4)f_-^2 \pm \square 3f_-^2((gQ_0/2)^2 + f_+^2) + f_+^4]^{1/2}\right\}^{1/2} ,$$
$$\varepsilon_{3;4}(\vec{p}) = -\varepsilon_{1;2}(\vec{p}) . \tag{7.9}$$

Recall that each of these four branches is determined in the reduced Brillouin zone.

At large enough $gQ_0/2$ the branches $\varepsilon_{1;2}(\vec{p})$ are separated in energy from the two other branches, $\varepsilon_{3;4}(\vec{p})$. Filling them up by the two polarized electrons per the new unit cell doubled in real space, completes the proof that, indeed, insulating $LaMnO_3$ *may* be considered as a band insulator.

For example, two sets of the spectrum branches (7.8), $\varepsilon_{1;2}(\vec{p})$ and $\varepsilon_{3;4}(\vec{p})$ may start first to overlap at $p_x = p_y = \pi/2$, for $\varepsilon_{j=1}(\vec{p})$ and $\varepsilon_{j=3}(\vec{p})$. The overlap is direct which imposes some limit on the value of the JT mode needed to ensure $LaMnO_3$ to behave as an insulator:

$$gQ_0 > 0.1|A| . \tag{7.10}$$

The optical gap, hence, corresponds to the excitation of an electron from the $\varepsilon_{j=1(2)}(\vec{p})$ band into the $\varepsilon_{j=3(4)}(\vec{p})$.

Let us make one more comment. Namely, while in the case of an isolated ion with one electron on the local degenerate e_{2g}-level, it inevitably leads to the local distortions, as follows from the JT effect itself, the ferromagnetic state with the band spectrum (5.14), filled up to some level, would remain stable with respect to small enough JT distortions. There is a threshold value for the magnitude of the JT deformations, before the new symmetry state may set in. In the cooperative JT effect, this threshold is determined from competition between the electronic kinetic energy gain and the elastic lattice energy. In case of $LaMnO_3$ the existence of the cooperative JT deformations is confirmed experimentally.

7.4. Antiferromagnetic ordering along the c-direction

Let us discuss factors that may lead to the antiferromagnetic ordering in the *c*-direction (A-phase). The related question concerns the low value of the Neel temperature ($T_N \approx 140$ K). This value corresponds to an energy scale that seems to be smaller than the scales introduced so far ($J_H \approx 1$ eV, $t \approx g_{JT} \approx 0.1$ eV).

In all derivations described above, including the energy spectrum (7.9), we assumed a strong inequality $J_H \gg t$, g_{JT}. As a result, the corrections of order t^2/J_H have been neglected so far. Nevertheless, these terms may be important for answering the question why the A-structure is favorable one. In other words, these small corrections still may determine the mutual spin orientation along the c-axis in the A-phase. For this, one needs estimate the contribution of these small terms into the total energy (Gor'kov and Kresin, 1998; Dzero et al., 2000). To simplify the problem, lets omit the JT terms and consider the one-band case. The equation of motion can be reduced to the form:

$$[E^2 - 2\hat{t}_{p_x,p_y}E + 2J_H\hat{\sigma}_x M\hat{t}_{p_z} + \hat{t}^2_{p_x,p_y}]\Psi_p = J_H^2 S^2 \Psi_p , \tag{7.11}$$

where, unlike in Eq. (7.13), we have preserved in the *t*-matrix its dependence on the moment perpendicular to the direction of the $\vec{q}$-vector ($\vec{q} \equiv (\pi/a)(0, 0, 1)$):

$$\hat{t} = \hat{t}_{p_x;p_y} + \hat{t}_{p_z}$$

and we also used that $t_{p_z+q_z} = -t_{p_z}$. Take in Eq. (7.11) $E = -J_H S + \varepsilon$. Eq. (7.11) gives $E_0 = +J_H S$, as expected. Eq. (7.11) leads to the generalized Anderson–Hasegawa term (1955);

$$\hat{\varepsilon}_+^{(1)} = \hat{t}_{p_x,p_y} + \cos(\theta/2)\hat{t}_{p_z} \ . \tag{7.12}$$

At the electron filling the linear in hopping term is averaged out, and for the total energy we obtain

$$E_{\rm el}^A = -\int \sqrt{(J_H S)^2 + t_{\vec{p}}^2}\, \frac{{\rm d}^3\vec{p}}{(2\pi h)^3} \cong -J_H S - \frac{t^2}{4J_H S} \ . \tag{7.13}$$

From (7.13) one may conclude first, that terms of the order of t^2/J_H in the electronic kinetic energy along the *c*-direction make the AF state (the A-phase) energetically more favorable.

Note also that, as it is well known, two-dimensional ferromagnetic state is never stable being destroyed by spin fluctuations. Stabilization of the A-phase must come up due to small terms in energy, which are responsible for remnant interactions between layers. Our estimates below for $A \approx 0.16\,$eV and $J_H S \approx 1.5\,$eV would place the terms t^2/J_H on the scale of $\approx 100\,$K which agrees well with the low value of the Neel temperature, $T_{\rm N} \approx 150\,$K.

Note, however, that the so-called "superexchange" interactions, $J S_i S_j$, with J, being on the same scale as t^2/J_H, may also become important (van der Brink and Khomskii, 1999) at the AF transition.

For the two-band case, generally speaking, terms linear in t, may remain after integration in (7.13). However, the JT splitting is more important as an additional factor in order to decrease the ground state energy below the energy of the ferromagnetic state. Large enough JT splitting reduced the problem of calculating terms of order of t^2/J_H to the one-band scenario.

In short, we suggest, that the lowest energy scale which determines the low value of the Neel temperature, $T_{\rm N}$, corresponds to the small parameter t^2/J_H, so that $T_{\rm N} \approx t^2/J_H$. This, indeed, corresponds to the experimentally observed value of $T_{\rm N}$.

7.5. Insulating state. Polarons

In our discussion of the insulating state above, we restricted ourselves by the parent compound, that is by the undoped manganites. Recall now (Sections 2,3) that the chemical substitution (e.g., La $\rightarrow$ Sr) of La^{+3} by the divalent ion leads to formation of "hole" in the unit cell. Experimentally, at the low doping level the material remains an insulator. This fact that at small concentration doped manganites preserve the insulating state raises an interesting problem.

The insulating behavior at light doping means that the introduced "holes" remain localized. One obvious reason for this is certainly the Coulomb attraction to the doping ion (Sr^{2+}) that prevents hole from immediately joining top of the one of the conduction bands (7.9). However, even if the Coulomb forces were screened on large distances in the presence of a finite hole concentration, strong electron–phonon interaction originated from the local JT term may significantly change the band characteristic. Local distortions may result in forming self-consistent trapping centers for hole/electron, i.e., creating a new type of a "carrier", the so-called "polaron". In the 3D case for a band carrier to become trapped into the polaronic state (usually with a much heavier effective mass), an energy is needed to overcome the energy barrier separating band and the trapped polaronic states. With the polaron density increase the latter should merge gradually into the band spectrum. Situation is more interesting and less trivial in case of the 2D electronic spectrum. It is worth saying a few words in this regard, since, as we have just

discussed, for the parent $LaMnO_3$ with it's A-type magnetic structure, the conducting network of the MnO-planes bears two-dimensional features.

In the 2D case the energy barrier for polaron formation may be equal to zero. Correspondingly, carriers may be either itinerant, or localized (having heavy masses) depending on numerical value of some parameter, C. This parameter characterizes competition for the energy gain between the gain in elastic energy (see linear and quadratic terms in Eq. (5.4)) due to the JT distortion, $\propto g^2 J_{\mathrm{el.}}$, and the kinetic energy gain due to the finite band width which is proportional to t. If the value

$$C \approx g^2/J_{\mathrm{el}}t \tag{7.14}$$

exceeds a threshold, usually of order of unity, the doped hole would inevitable go into a trapped state (Rashba, 1982; Toyozawa and Shinozuka, 1983).

In simple terms, Eq. (7.14) tells us whether, due to lattice deformation, the hole energy goes below the bottom of the band and, thus, remains "localized". Recall again that for the A-structure (see above, Section 7.3) the transport has mainly a 2D nature. Since experimentally, at low doping manganites first remain in insulating state, we conclude that criterion (7.14) favor absence of the potential barrier for localization of introduced holes, or, in other words, holes are trapped into "heavy" polarons.

The polaronic picture and criterion (7.14) makes sense in the limit of low enough carrier concentration only. Increase in doping leads, eventually, to percolation and the phase separation picture described in Sections 3, 4.

The superlattice of the parent $LaMnO_3$ rapidly becomes irrelevant with disorder and we are entering into the percolation regime (see above, Section 3). At the percolation threshold, $x_c \approx 0.16$, an itinerant conduction network develops leading to the transition into metallic (and ferromagnetic) ground state. As we have shown before, somewhat above the percolative concentration threshold the formed macroscopic metallic phase can be again described in terms of the band theory.

8. Interface and tunneling phenomena

8.1. Charges and spins near interface

Possibility to use manganites with their rich phase diagram in some practical applications has been already discussed in a number of papers (see, e.g., Tokura, 2003; Gor'kov and Kresin, 2001). In this connection, we address below some problems which involve artificial contacts of manganites with different magnetic ground states or just two manganites having the same ground states but different doping concentrations. We will discuss both charge and magnetic structure in the vicinity of the boundary. Below we consider the plane geometry, so that all quantities depend on one coordinate only. In addition we simplify our discussion by restricting ourselves by choosing the single band DE model.

We first consider two ferromagnetic manganites with different doping concentrations brought into contact with each other with the parallel orientations of the local moments. Some pronounced effects come about due to the Schottky layers formed at the contact. A difference in doping concentrations produces a difference in the chemical potentials on both sides away from the contact, $E_{\mathrm{F}}^{\mathrm{left}}$ and $E_{\mathrm{F}}^{\mathrm{right}}$, i.e. a difference in the "work functions" of two components.

As usual, that leads to a redistribution of carriers near the contact plane. This effect is general and well-known for contacts between metals or semiconductors. A simplifying feature for contacts of two

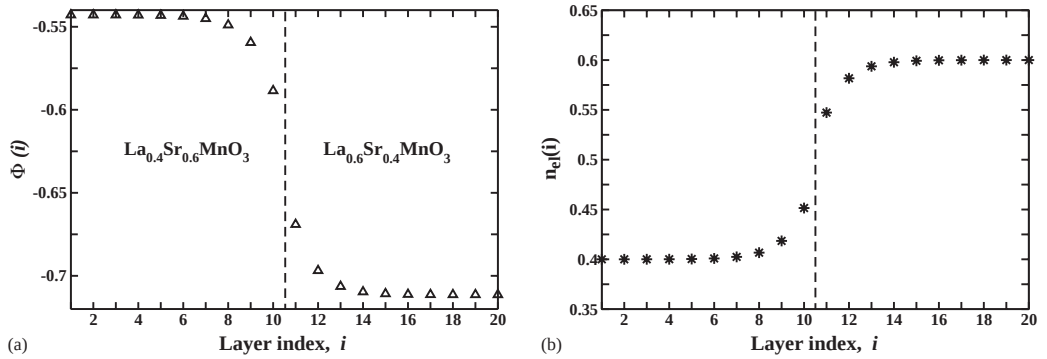

Fig. 17. Contact of two metallic ferromagnetic phases with different Sr concentrations in the one band DE model. The numerical solution of Kohn–Sham equations is shown for the structure with number of layers being equal to 20. The dashed line shows the position of the (La,Sr) plane, where the abrupt change in Sr concentrations takes place: (a) Potential $\phi(t)$ is given in dimensionless units $4\pi e^2/(\mathrm{at})$: (b) $n_{\mathrm{el}}(i)$ is the concentration of electrons in the layer i in units of a^{-2}, where a is a lattice constant.

manganites is the similarity of the underlying band structures on both sides of a contact. At the same time all major changes still take place on the atomic scale so that one needs to apply the Kohn–Sham scheme to solve for potential and charge distributions self-consistently.

We proceed as follows. Let $N_{\mathrm{L(R)}}$ be the concentration (i.e. the number per cm^2) of positive charges in the (LaSr) plane on the left (right) side far away from the contact. These planes are chosen as basic elements of our analysis because in the process of preparation of the heterostructure (film deposition; Izumi et al., 2000), the Sr concentration N_{Sr} changes sharply from N_{L} to N_{R} at the contact. The system of Kohn–Sham equations (the discretized equations for Poisson potential distribution and the Schrodinger equation for the in-plane wave function, correspondingly) is

$$\Phi(i+1) - 2\Phi(i) + \Phi(i-1) = (4\pi e/t)[N_{\mathrm{Sr}}(i) - n_{\mathrm{el}}(i)] \ ,$$
$$\Psi_\lambda(i+1) + 2\Psi_\lambda(i) - \Psi_\lambda(i-1) + \Phi(i)\Psi_\lambda(i) = E_\lambda \Psi_\lambda(i) \ ; \tag{8.1}$$

where i is an index which runs through the Mn-planes, λ is an eigenvalue index, E_λ is the 2D-energy in units of t, Φ is a dimensionless potential defined through electrostatic potential $\varphi(i)$ as

$$\Phi(i) = -|\mathrm{e}|\varphi(i)/t \tag{8.2}$$

$n_{\mathrm{el}}(i) = \Sigma_{\lambda<\lambda}|\Psi_\lambda(i)|$ is a concentration of electrons on a plane i and $N_{\mathrm{Sr}}(i)$ is a Sr concentration, which depends on which side of the contact one considers, and $E_{\lambda\mathrm{f}} = E_{\mathrm{F}}(i)$ with $E_{\mathrm{F}}(i)$ being equal to the local Fermi level in the units of t. We have obtained a numerical solution of (8.1) with the boundary conditions providing the equality of the electrochemical potentials across the contact. In the calculations below the total number of layers was equal to twenty (ten on each side of the contact) with

$$N_{\mathrm{Sr}}(i) = \begin{cases} 0.6, & i \leqslant 10 \ , \\ 0.4, & i \geqslant 11 \ . \end{cases} \tag{8.3}$$

The solution for the potential and electron distribution is shown on Fig. 17. The consistency of our numerical results have been verified by comparing them with the analytical ones obtained from the solution of the same problem in its continuous form (see Appendix B).

The significance of these calculations is as follows. First of all, one sees that the electron screening (the "Thomas–Fermi" length) extends over four–five atomic distances implying that the sharpness of the contact is smoothed out considerably. Secondly, there is a redistribution of charge between phases: repletion and depletion regions form close to the interface.

We now turn to a qualitative discussion of contacts between two manganites belonging to the ferromagnetic and antiferromagnetic A-phase, correspondingly. The results of the previous section have demonstrated existence of the pronounced magneto-resistance effects in the canted A-phase for both in-plane and out-of-plane current directions. This justifies an interest and the need for a better understanding of the F/A contact properties. Stacks of manganite films of different thickness with abrupt change in Sr concentration in the (LaSr) planes in order to stabilize FM- or A-phase, can be made using the state of the art deposition techniques (Izumi et al., 2000). However contacts between the FM state and the A-phase are more complicated than the preceding example of the contact between the two unequally doped ferromagnetic metallic manganites. First of all, one should expect that the charge effects discussed above for a contact between the two FM phases exists at present case as well. Redistribution of the carriers may shift the boundary position between the magnetic phases. Even less clear is the magnetic structure of such a transitional layer: whether there is a sharp boundary for change of spins orientations on both sides of a contact or the direction of spins may rotate at going through the interface from left to right, needs further study. In particular, since the energy of magnetic anisotropy in manganites is rather weak (magnetization of ferromagnetic manganites is saturated at external fields of the order of 100 Oe, see Coey et al., 1999) orientation of moments may even change gradually forming a structure similar to the one in the Bloch or Neel domain wall. The transitional region between the two phases may include a canted A-phase, magneto-conductivity of which has been studied above. It is highly desirable to further address these issues experimentally.

As far as an interface is concerned, the complications that lie on the theory part are as follows. The DE mechanism that played such an important role in exploring the properties of the half-metallic magnetic ground state, bears a non-local character. Therefore it is not straightforward to account for physics in an inhomogeneous problem with a spatial dependence near the interface. Secondly, diminishing the number of band electrons, the anti-ferromagnetic super-exchange interaction between the t_{2g} spins becomes comparable with the DE interaction. The task of combining these two mechanisms to study an inhomogeneous problem is already a serious problem.

The A-phase ground state has been found in a number of other compounds, such as $Pr_{0.5}Sr_{0.5}MnO_3$ and $Nd_{0.45}Sr_{0.55}MnO_3$ (Kuwahara et al., 1999; Tomioka et al., 1995). The transition into the A-phase along the temperature axis is of the first order as it is expected from symmetry considerations. It is accompanied by a change in the c/a ratio (Izumi et al., 2000; Tokura et al., 1994). Such a transition is often described in the literature in terms of the "orbital ordering" (Kugel and Khomskii, 1973). We suggest that this transition is nothing but as a cooperative Jahn–Teller effect involving the proper lattice distortion, namely, compression of the oxygen octahedra along the *c*-axis. Indeed, so far we have discussed changes in the electronic band structure caused by spin re-arrangements only. Meanwhile, the lattice effects may also play an important role in the energetics of the transition into the A-phase. Judging from various experimental results (for a review, see Tokura and Tomioka, 1999), the importance of the lattice effects may vary and depend on a specific compound. For example, the lattice deformations strongly prevail in $Nd_{0.45}Sr_{0.55}MnO_3$ compound. Its ground state shows huge anisotropy in resistivity ($\rho_c/\rho_{ab} \approx 10^4$) and much lower in-plane conductivity compared to other members of the A-phase family. As it was shown by Gor'kov and Kresin (1998), Dzero et al. (2000), the strong enough shear deformation of the

oxygen octahedra ($c/a < 1$) alone may lead to a practically two-dimensional electronic spectrum. We suppose that $Nd_{0.45}Sr_{0.55}MnO_3$ is such an extreme case ($t \approx 0.95$), see Tokura and Tomioka (1999). After carriers are added to the 2D bands, both spins of the carriers and the core spins adjust themselves via DE and super-exchange mechanisms. It may happen that in other A-phase compounds the tetragonal deformations of the lattice $c/a < 1$, is less pronounced. In such a case one may neglect it as we have done above for $La_{0.45}Sr_{0.55}MnO_3$. The phase diagram for the $La_{1-x}Sr_xMnO_3$ as a function of Sr doping x has been theoretically studied by Fang et al. (2000). We note, that the Jahn–Teller interaction has not been considered in that paper and the electronic band structure was obtained for a fixed values of c/a.

In Izumi et al. much attention was also given to characterization of properties of the heterostructures consisting of mixed phases [F_n, A_m] (n and m are the number of unit cells per period of the structure; Izumi et al., 2000). Major conclusion drawn by the authors from data on magnetization, structural characterization of the modulated films and their in-plane conductivity have led them to the notion of stable FM and A-phase single layers, which preserve their integrity and stability even in very thin intervening structures such as n; $m = 2$–5. This result is in favor of the view that the stability of the A-phase layers is mainly due to the coherent octahedra shrinkage, $c/a < 1$, in the planes. Such a notion still leaves enough room for speculation regarding possible spin arrangements in the heterostructures. It is interesting that the conductivity measurements for the samples with composition [F_{10}, A_{10}] gave lower values of the in-plane conductivity as if conductivity were due to the FM layers alone. We ascribe this to the effect of charge re-distribution shown in Fig. 17: ferromagnetic layers having more carriers supply part of them into the A-phase layers (10 layers of each phase is already a good approximation for the homogeneous picture of a single interface). For compositions [F_n, A_m] with n and m decreased, the role of Coulomb effects becomes weaker and each layer preserves its nominal composition and hence, the in-plane conductivity.

One more comment we would like to add to the latter point concerns a pronounced increase in magneto-conductivity toward the [F_3, A_3] samples. If the number of electrons on each FM- and A-phase planes does not change, the positive magneto-conductivity effect is an indication of stronger canting of the moments in these samples. (Recall that large values of in-plane magneto-conductivity on Fig. 12 is a result of changing Fermi level at the transition between the 2D and 3D regimes). Data provided by Izumi et al. (2000) qualitatively agree with the theoretical results (Dzero et al., 2003) for the values of in-plane conductivity for the canted A-phase.

8.2. *Josephson contact with the A-phase barrier*

As is known, the superconducting state is characterized by macroscopic phase coherence. The Josephson effect (Josephson, 1962; see Barone and Paterno, 1982; Tinkham, 1996) represents the most remarkable manifestation of this coherence. The Josephson contact is comprised of superconducting electrodes separated by a tunneling barrier. The d.c. current flows through the contact without any external voltage and is described by the equation:

$$J = j_0 \cos\varphi \ , \tag{8.4}$$

where $\varphi = \varphi_1 - \varphi_2$ is the phase difference of the superconducting order parameters on each side of the barriers. The most common case is the S–I–S Josephson junction, where I denotes a thin insulating barrier. Another well-known case is the S–N–S junction; here N is a normal metal. The amplitude of the superconducting current for such a junction (see, e.g., Barone and Paterno, 1982; Kresin, 1986) is

proportional to

$$j_0 \propto \exp(-L_N/\xi_N) \ , \tag{8.5}$$

if $L_N > \xi_N$, and $j_0 \propto (\xi_N/L_N)$ if $L_N \ll \xi_N$. Here ξ_N is the normal coherence length defined as ("clean" case; Clarke, 1969)

$$\xi_N = \hbar v_F/2\pi T \ . \tag{8.6}$$

One can see from Eq. (8.5) that for effect to be observable the thickness of the barrier L_N should not exceed noticeably the coherence length ξ_N.

Let us consider the barrier formed by a magnetic metal. It is well understood that for two superconductors with singlet (s- or d-waves) pairing a ferromagnetic barrier (S–F–S junction) would present a strong obstacle. Indeed, the Josephson current is a transfer of a Cooper pair with its spins of the two electrons in opposite directions. The exchange field in the ferromagnetic is trying to align the spins in the same direction, and this leads to the pair breaking effect. The situation is entirely different for the tunneling through antiferromagnetic metallic (S–AFM–S) system (Gor'kov and Kresin, 2001). Contrary to the pair-breaking F case, superconducting currents might penetrate through an AFM barrier much easier. This process reveals rather non-trivial aspects in case of the A-phase taken the barrier which deserve special treatment.

We consider the junction in such geometry, that the Josephson current would flow along ferromagnetic layers. The layers are weakly coupled electronically. It is important, because the Josephson current is a transfer of *correlated* electrons. Below we keep in mind the manganite is in the metallic A-phase (Section 6) for such a barrier. The A-phase manganite is a natural spin–valve system (see, e.g., Kawano et al., 1997), unlike an artificial GMR multilayer system (Parkin, 1995).

To demonstrate the effect, we assume that the barrier is thick enough to neglect phenomena taking place in the immediate proximity to the boundary, i.e., $L \gg \xi_0$; where L is the width of the barrier, $\xi_0 = \hbar v_f/2\pi T_C$ is a coherence length. Then one can use the interface Hamiltonian in the form

$$H = V\Delta^{(i)}\psi^+(i)\psi(i) \ . \tag{8.7}$$

Here $\Delta^{(i)}$ are superconducting order parameters on each side, i, ψ^+, ψ are the field operators for the carriers inside the barrier, and V is a tunneling matrix element at the boundary of the barrier; integration along the contact surface is assumed.

As a next step it is practical to evaluate not the current itself directly, but find, instead, the "surface" contribution to the thermodynamic potential, $\delta\Omega$, caused by the presence of the barrier separating two bulk superconductors. The current is then determined as a derivative $\delta\Omega/\delta\varphi$, where $\varphi = \varphi_1 - \varphi_2$ is the phase difference between the two superconductors, so that $\Delta^{(1)} = |\Delta^{(1)}| \exp(i\varphi_1)$, $\Delta^{(2)} = |\Delta^{(2)}| \exp(i\varphi_2)$. The amplitude of the Josephson current, j_m, turns out to be proportional to the matrix element of the Cooper diagram

$$K(1,2) = |V|^2 \sum_{\omega_n} \Delta^{(1)}_{\sigma\sigma'} G_{\sigma\sigma''}(1,2;\omega_n) G_{\sigma'\sigma'''}(1,2;-\omega_n) \Delta^{*(2)}_{\sigma''\sigma'''} \ . \tag{8.8}$$

Recall that for a singlet superconductor $\hat{\Delta}$ is the matrix of the form $\Delta^{(i)}_{\sigma\sigma'} = \Delta^{(i)}(i\sigma_y)_{\sigma\sigma'}$. A method of thermodynamic Green's function is employed (see, e.g., Abrikosov et al., 1975); a summation over repeating spin indexes is assumed. To properly evaluate the current through the magnetic barrier, one

should pay special attention to the spin structure of Eq. (8.8), because the Green's functions, $G_{\sigma\sigma''}$ and $G_{\sigma'\sigma'''}$, inside the barrier are not diagonal in spin indices. After straightforward calculations (Gor'kov and Kresin, 2001), one can obtain the kernel $K(1,2)$:

$$K(1,2) = 2\pi T|V|^2 \sum_{\omega_n} \Delta^{(1)}\Delta^{(2)} \int \mathrm{d}\vec{p}\,\mathrm{d}\vec{q}\,\exp(\mathrm{i}\vec{q}\,\vec{L})\Pi_{12}(\omega_n;\vec{q}) \ , \tag{8.9}$$

where

$$\Pi_{12}(\omega_n;\vec{q}) = [G_{\downarrow\uparrow}(\omega_n;\vec{p})G_{\uparrow\downarrow}(-\omega_n;\vec{q}-\vec{p}) - G_{\downarrow\downarrow}(\omega_n;\vec{p})G_{\uparrow\uparrow}(-\omega_n;\vec{q}-\vec{p})] \ . \tag{8.10}$$

One can use the following energy spectrum:

$$\varepsilon = \pm\Big[J_H^2 S^2 \pm 2J_H M t_{||} + t_{||}^2\Big]^{1/2} \ . \tag{8.11}$$

The Green's functions appearing in Eq. (8.10) could be expressed in terms of new Fermi amplitudes which correspond to the four energy branches (8.11). The transformation to the new amplitudes, as usual can be described by the canonical transformation $a_{p\sigma} = \Sigma_i K_{\sigma i}\alpha_{ip}$. The calculation leads to the following general expression for the amplitude of the Josephson current:

$$j_m = r\gamma T \sum_{\omega_n>0} \int \mathrm{d}p_z \exp(-\omega_n L/v_\mathrm{F}) \cos(Lt_{||}M/Sv_\perp) \ ,$$

$$\gamma = [1-(M/S)^2]; \quad r \propto |V|^2|\Delta_1|^2|\Delta_2|^2 \ . \tag{8.12}$$

Eq. (8.12) contains the integration over the transverse cross-section of the Fermi surface (over ℓ). Assume that the width of the barrier $L \gg \xi_\mathrm{N}$, ξ_N is the coherence length for the normal layer, Eq. (8.6). Then one can keep only the first term of sum in (8.12). In the tight-binding approximation $t_{||}(p_z) = t_0\ \cos(p_z d)$ (d is the interlayer distance). Integrating over p_z, we arrive at the following expression:

$$j_m = j_m^0 \mathrm{e}^{-L/\xi_N(T)} J_0(\beta M/S) \ . \tag{8.13}$$

Here $\xi_\mathrm{N}(T)$ is the coherence length inside the barrier (see above), $j_m^0 = [1-(M/S)^2]\mathrm{Tr}$, $\beta = (t_0/T_\mathrm{C})(L/\xi_0)$; $\xi_0 = \hbar v_\mathrm{F}/2\pi T_\mathrm{C}$; $v_\mathrm{F} = v_\mathrm{F}^0$ is the maximum value of the component of the Fermi velocity along L. It is essential that $\beta \gg 1$; indeed for manganites $t_0 \gg T_\mathrm{C}$ and $L \gg \xi_0$. If the canting M/S is not negligibly small then one can use an asymptotic form of the Bessel function, $J_0(x)$, and we obtain

$$j_m \approx (\pi\beta M/2S)^{-1/2} j_m^0 \mathrm{e}^{-L/\xi_N(T)} \mathrm{Cos}(\beta M/S - \pi/4) \ . \tag{8.14}$$

Eq. (8.14) above is valid if $L \gg \xi_N(T) = \hbar v_\mathrm{F}/2\pi T$. Near $T = 0\,\mathrm{K}$ this condition is not satisfied. In this region one can replace the summation in Eq. (8.12) by integration, and we obtain

$$j_m = j_m^0 \xi_0 J_0(\beta M/S) \ . \tag{8.15}$$

Again at $\beta \gg 1$, if M/S is not close to zero, one can use the asymptotic expression for $J_0(x)$ (cf. Eq. (8.14)).

Therefore, the antiferromagnetic barrier in accordance with Eqs. (8.12)–(8.15) does transfer the Josephson current; in this case the exchange field does not break the Cooper pairs. In principle, however, the mutual magnetic orientations of layers can be controlled by an external magnetic field. Thus, the AFM

structure can be transformed into the ferromagnetic configuration (AFM → FM). The complete AFM → FM reorientation would result in a drastic impact forbidding the Josephson current for the FM case $j_m = 0$. This follows from our result in Eq. (8.12); indeed, then $M = S$ and $j_m = 0$.

It is very interesting, that, according to (8.14), one observes the oscillatory dependence of the amplitude of the Josephson current on an external magnetic field: $j_0 \propto \cos(\beta M/S - \pi/4)$. Canted moments may be induced by even a week field and would result at $\beta \gg 1$ in rapid and large ("Giant") changes in the Josephson current ("Giant" magnetooscillations for the Josephson contact with the presence of A-structure as a weak link). The oscillating dependence was theoretically obtained by Buzdin et al. (1982) for the ferromagnetic barrier who considered the oscillations caused by *change in the barrier* thickness. As was described above, for the antiferromagnetic barrier, one can observe this effect as due to *slight variations in the external magnetic field* value.

Speaking of the manganite-superconductor systems, one should mention also interesting study (Habermeier, 2004) of the S_h-M superlattices ($S_h \equiv YBa_2Cu_3O_{7-x}$ is the high temperature superconducting oxide, and $M \equiv La_{2/3}Ca_{1/3}MnO_3$ is the manganite in the ferromagnetic metallic state). As is known, the high temperature superconducting compounds are layered compounds which can be treated as 2D systems (CuO planes) connected by intrinsic Josephson coupling (Kleiner et al., 1992; Scheekga et al., 1998). Various properties of this multilayer system have been studied. By changing the parameters of each component, one can strongly affect the values of the superconducting critical temperature and $T_C \equiv T_{curie}$. It was shown also that the opening of the pseudogap in $YBa_2Cu_3O_{7-x}$ (the pseudogap phenomenon is usually observed in the underdoped cuprates and manifests itself in the existence of the energy gap structure above the superconducting critical temperature) leads to weakening of the interlayer ferromagnetic coupling and to the reduction of $T_{curie.}$ This system is an artificial structure analogous to the natural S-FM superlattice, realized by the family of ruthenates $RuSr_2RECu_2O_8$ and $RuSr_2RE_{2-y}Ce_yCu_2O_{10}$ with RE = Gd, Eu (Felner et al., 1997; Chu et al., 2000).

9. Conclusion

Manganites display the very rich phase diagram. The phases differ in their conductivity (metallic vs. insulating), anisotropy of their properties (layered vs. 3D), magnetic structure (ferromagnetic vs. antiferromagnetic), appearing in countless combinations. Research in the area was re-energized after the discovery of the colossal magnetoresistance (CMR). However, our understanding of manganites still remains not complete. Many interesting questions, such, for instance, as the role of the JT effects and competing interactions for numerous symmetry structures, competition between DE and superexchange, and magnetic terms must be resolved on a more quantitative level.

In this Review we were mainly interested in the low temperature properties of manganites, that is, first of all, in the nature of the ground state and its dependence on doping. It was demonstrated (Section 3) that the metal–insulator transition at the doping level $x_c \approx 0.17$ realizes itself as a percolation phenomenon and the value x_c is the universal percolation threshold. The percolative character of the metal–insulator transition with doping resulting in such non-trivial and uncommon features as coexistence and interweaving of the phases with different properties, singles out manganites between many other materials. For example, for $x < x_c$ (insulating state) the material has tiny metallic inclusions. At $x > x_c$ (or $T < T_C$) the compound, however, contains inclusions of the insulating phase, or penetrating antiferromagnetic islands.

It turns out that one can built up a sensible quantitative theory that explains self-consistently main peculiarities in these materials by using a relatively simple Hamiltonian (Section 4) which contains, as the key ingredients, hopping term, Hund's and Jahn–Teller interactions. One sees that the band approach utilizing all these interactions, provides an adequate and unifying approach even to a phase diagram as a whole, and properties of materials with different compositions.

Note also that this review contains many results obtained analytically. It is clear that such an approach has a serious advantage not only because it allows one to gain an additional insight, but also because the calculations are tractable, whereas the numerical results are sometimes contradictory (cf., Dagotto et al., 2001; Furukawa, 2003b).

The study of manganites continues to undergo an intensive experimental and theoretical development. Unfortunately, sample's quality remains a major obstacle for experimental study so far and, subsequently, for various applications. It is not accidentally that there many contradictory reports for samples with the same nominal composition. However, recent progress with sample preparation looks very promising.

There are, of course, still many interesting theoretical challenges that we have been mentioning in our review. Among them: a detailed analysis of the polaronic states occurring at $x < x_c$ and above the Curie temperature for the metallic ferromagnetic phase, conductivity mechanisms, calculation of magnetoresistance with use of the two-band model, quantitative understanding of the interplay between the double exchange and superexchange spin interactions, evaluation of a whole class of fundamental properties (e.g., spin waves spectrum for the insulating phase), etc.

In summary, this paper contains a description of main experimental facts and new basic ideas that allow the transparent interpretation of manganites' properties as a whole. We discuss transition to the ferromagnetic and metallic state at finite doping and demonstrate that in these materials such an insulator-to-metal transition represents a fundamentally new type of the transition that must be described in the percolation terms. The same approach turns out to be applicable for the transition at the Curie temperature. As a result of the percolation theory approach, the view of these materials, both above and below the transition point, is that of inhomogeneous media consisting of tiny islands of interweaving sub-phases, thus, realizing a special case of phase separation. These basic new ideas have been now verified experimentally with the use of various experimental techniques (neutron data, Mossbauer spectroscopy, heat capacity and magnetization measurements, etc.).

We have also shown that even the quantitative understanding of numerous manganites' properties can be achieved by making use of a generalized two-band model that takes into account of the crystal-field-split d-shell of the Mn^{3+} ions, the Zener's double exchange interaction and strong electron-phonon interaction due to the cooperative JT effect. We have traced changes in the ground state with doping, describe various manganites' low temperature properties, both thermodynamic and kinetic ones, and compared the theoretical predictions with experimental data. As a result, one arrives to the self-consistent and quantitative understanding of main physics in the metallic manganites. With the theoretical expressions in hands some other effects are discussed. Thus, an attention was given to phenomena taking place in the contact area of two manganites' phases. A giant oscillations in the Josephson current of a S–AFM–S junction using as a barrier the antiferromagnetic metallic A-phase are predicted as a function of weak applied magnetic fields. The experimentally observed strong isotope effect is explained.

We think that the study of these remarkable materials is far from being complete, and we hope that the description of various properties of manganites and challenges, presented in this article, will be useful for future research in this area.

Acknowledgements

The authors are grateful to DARPA for the support. We greatly benefited from fruitful discussions with I. Bozovic, H. Drew, T. Egami, Y. Tokura, J. Lynn, B. Raveau and S. von Molnar. We are grateful also to M. Dzero who was our co-author on several papers.

Appendix A. Basis set: real functions

Here we address some details regarding the energy spectrum. The explicit calculations for the electronic spectrum were performed with use of complex basis set (5.2) which emphasizes the cubic symmetry. As was noted above (Section 5.1) one can also use the set of real functions (5.3), or, more exactly:

$$\varphi_1 = d_{z^2=}(5/16\pi)^{1/2} f(r) r^{-2}(2z^2 - x^2 - y^2) \propto 3\,\mathrm{Cos}^2\,\vartheta - 1\ , \tag{A.1}$$

$$\varphi_2 = d_{x^2-y^2=}(5/16\pi)^{1/2} f(r) r^{-2}(x^2 - y^2) \propto \mathrm{Sin}^2\,\vartheta\,\mathrm{Cos}^2\,\vartheta\ . \tag{A.2}$$

There is a simple connection between the two sets, Eq. (5.4). The basis set of real functions is more commonly used in literature. In addition, unlike (5.2) their use allows better qualitative "visualization" of the relevant charge distribution on orbitals. Of course, the energy spectrum and the values of measured quantities do not depend on the choice of the basis set, even though various matrix elements are different.

The periodic Bloch wave function can be constructed as the superposition:

$$\Psi(\vec{r}) = \sum_n \mathrm{e}^{\mathrm{i}\vec{k}\vec{a}_n}\{\alpha\psi_1(\vec{r} - \vec{a}_n) + \beta\psi_2(\vec{r} - \vec{a}_n)\}\ . \tag{A.3}$$

With use of the stationary Schrödinger equation, one can obtain the following secular equation for the energy, ε:

$$\begin{vmatrix} \sum\limits_i I^i_{11}\cos k_i - \varepsilon & \sum\limits_i I^i_{12}\cos k_i \\ \sum\limits_i I^i_{21}\cos k_i & \sum\limits_i I^i_{22}\cos k_i - \varepsilon \end{vmatrix} = 0\ . \tag{A.4}$$

Here $i = \{x, y, z\}$, $I^i_{kl} = \int \varphi^{(r)}_k T \varphi_e(\vec{r} - \vec{a}_{ni})\,\mathrm{d}\tau$, $k, l = \{1, 2\}$, T describes the hopping (cf. Eq. (5.6′)).

Introducing the constants $A \propto \int \varphi_1\varphi_{1z}\,\mathrm{d}\tau$ and $\beta \propto \int \varphi_2\varphi_{2z}\,\mathrm{d}\tau$; $\varphi_{iz} = \varphi_{i,z+a}$, we obtain, after straightforward calculations, spectrum (5.8).

With use of the basis set (A.1), (A.2) one can calculate various properties. For example, the analysis of optical properties (Section 5.6) requires the calculation of the matrix elements of the off-diagonal operator $\hat{\Omega}$ (see Eq. (5.38)). The calculation utilizing real functions as a basis set, leads to the expression for the interband matrix element

$$\langle 1\vec{k}|\hat{\Omega}|2\vec{k}\rangle = 0.5[(\partial S^+/\partial\vec{k})S^- - (\partial S^-/\partial\vec{k})S^+]\ , \tag{A.5}$$

$$S^{\pm} = (1 \pm \gamma/\tau)\ ,$$

$$\gamma = 2\,\cos k_z - f^+\ ,$$

where

$$f^{+} = \sum_i \cos\, k_i \ ;$$

$$\tau = 2\left[\sum_i \cos\, k_i - \sum_{i\neq m} \cos\, k_i \cos\, k_m\right] \ ,$$

Eq. (5.42) then follows from Eq. (A.5).

Appendix B. Analysis of the interface problem in the continuous model

One can obtain a general solution of Eq. (8.1) in continuous limit. In that case, one can solve the Poisson equation on each side of the contact and, after using the boundary conditions, obtain a general solution.

If the plane of the interface coincides with *yz* plane, the potential will depend on *x* only. We assume the spectrum of the electrons to have a parabolic form: $\varepsilon(k) = k^2/2m$. The concentration of electrons is given by

$$n_{\rm el}(x) = \frac{(2m)^{3/2}}{3\pi^2\hbar^3}\,[\mu(x)]^{3/2} \ , \tag{B.1}$$

where $\mu(x)$ is a local chemical potential. Taking into account (B.1), we have to solve the Poisson equation

$$\frac{{\rm d}^2\Phi}{{\rm d}x^2} = \frac{4\pi e^2}{t}\,[N_{\rm Sr}(x) - n_{\rm el}(x)] \ , \tag{B.2}$$

where $N_{\rm Sr}$ is a Sr concentration defined by

$$N_{\rm Sr}(x) = \begin{cases} N_{\rm L}, & x \leqslant 0 \ , \\ N_{\rm R}, & x \geqslant 0 \ . \end{cases} \tag{B.3}$$

We introduce the following notations: $\mu(x) + \Phi(x) = \varsigma = \text{const}$, where ζ is an electrochemical potential and $\phi(x)$ is

$$\Phi(x) = \begin{cases} \Phi_{\rm L}(x), & x \leqslant 0 \ , \\ \Phi_{\rm R}(x), & x \geqslant 0 \ . \end{cases} \tag{B.4}$$

The boundary conditions for the potential preserving the charge conservation are

$$\Phi_{\rm L}(0) = \Phi_{\rm R}(0), \quad \frac{{\rm d}\Phi_{\rm L}}{{\rm d}x} = \left.\frac{{\rm d}\Phi_{\rm R}}{{\rm d}x}\right|_{x=0} \ . \tag{B.5}$$

Afterwards, one can obtain numerically solution of Eq. (B.2), see Fig. 14 (Dzero et al., 2003). It is useful to obtain the solution of the Poisson equation (B.2) in the linear approximation, assuming $\Phi(x)$ is small compared to ζ. After a very simple algebra, (B.2) takes the following form:

$$\frac{{\rm d}^2\Phi(x)}{{\rm d}x^2} = \frac{1}{\lambda^2}\,[\Phi(x) - \Phi(\pm)] \ , \tag{B.6}$$

where

$$\frac{1}{\lambda^2} = \left(\frac{2e^2(2m)^{3/2}}{\pi\hbar^3}\right)\varsigma^{1/2} ,$$

$$\Phi(\pm\infty) = \frac{(2m)^{3/2}/(3\pi^2\hbar^3)\varsigma^{3/2} - N_{\mathrm{L(R)}}}{2(2m)^{3/2}/(2\pi^2\hbar^3)\varsigma^{1/2}} . \tag{B.7}$$

Taking into account the boundary conditions (B.5), the integration of (B.7) is straightforward. Thus the solution of (B.7) reads

$$\Phi(x) = \begin{cases} \Phi(+\infty) + \delta\Phi \mathrm{e}^{-x/\lambda}, & x \geqslant 0 , \\ \Phi(-\infty) - \delta\Phi \mathrm{e}^{-x/\lambda}, & x < 0 , \end{cases} \tag{B.8}$$

where $\delta\Phi = 0.5(\Phi(-\infty) - \Phi(+\infty))$. As it is easy to see, the result given by (B.8) reproduces all the features of our numerical solution shown in Figs. 14(a) and (b).

References

Abrikosov, A., Gorkov, L., Dzyaloshinski, I., 1975. Methods of Quantum Field Theory in Statistical Physics, Dover, NY.
Akimoto, T., Maruyama, Y., Maritomo, Y., Nakamura, A., 1998. Phys. Rev. B 55, R5594.
Anderson, P., 1959. Phys. Rev. 115, 2.
Anderson, P., Hasegawa, H., 1955. Phys. Rev. 100, 675.
Barone, A., Paterno, G., 1982. Physics and Applications of the Josephson Effect, Wiley, NY.
Bednorz, J., Mueller, K., 1986. Z. Phys. B 64, 189.
Bekker, T., Streng, C., Luo, Y., Moshngaga, V., Damasschke, B., Shannon, N., Samwer, K., 2002. Phys. Rev. Lett. 89, 237203.
Belova, L., 2000. J. Supercond. Novel Magn. 13, 305.
Bersuker, I., 1996. Electronic Structure and properties of Transition Metals Compounds; Introduction to the Theory, Wiley, NY.
Bersuker, I., Polinger, V., 1989. Vibronic Interactions in Molecules and Crystals, Springer, NY.
Billinge, S., Proffen, T., Petkov, V., Sarrao, J., Kycia, S., 2000. Phys. Rev. B 62, 1203.
Blanter, Y., Kaganov, M., Pantsulaja, A., Varlamov, A., 1994. Phys. Rep. 245, 161.
Booth, C., Bridges, F., Snyder, G., Geballe, T., 1996. Phys. Rev. B 54, 15606.
Booth, C., Bridges, F., Kwei, G., Lawrence, J., Cornelius, A., Neumeier, J., 1998a. Phys. Rev. Lett. 80, 853.
Booth, C., Bridges, F., Kwei, G., Lawrence, J., Cornelius, A., Neumeier, J., 1998b. Phys. Rev. B 57, 10440.
Bridges, F., Booth, C., Li, G., 1995. Physica B 208 & 209, 121.
Bridges, F., Booth, C., Kwei, G., Neumeier, J., Sawatzky, G., 2000. Phys. Rev. B 61, 9237.
Bridges, F., Booth, C., Anderson, M., Kwei, G., Neumeier, J., Snyder, J., Mitchell, J., Gardner, J., Brosha, E., 2001. Phys. Rev. B 63, 214405.
Burgy, J., Mayr, M., Martin-Mayor, V., Moreo, A., Dagotto, E., 2001. Phys. Rev. Lett. 87, 277202.
Buzdin, A., Bulaevskii, L., Panyukov, S., 1982. JETP Lett. 35, 178.
Casa, D., Kiryukin, V., Salen, O., Keimer, B., Hill, J., Tomioka, Y., Tokura, Y., 1999. Europhys. Lett. 47, 90.
Chahara, K., Ohno, M., Kasai, M., Kosono, Y., 1993. Appl. Phys. Lett. 63, 1990.
Chechersky, V., Nath, A., Isaak, I., Franek, K., Ghosh, K., Jeu, H., Greene, R., 1999. Phys. Rev. B 59, 497.
Cheong, S., Hwang, H., Chen, C., Batlogg, B., Rupp Jr., L., Carter, S., 1994. Phys. Rev. B 49, 7088.
Chu, C., Xue, Y., Wang, Y., Hellman, A., Lorenz, B., Meng, R., Cmaidalka, J., Dezaneti, L., 2000. J. Supercond. Novel Magn. 13, 679.
Clarke, J., 1969. Proc. R. Soc. Ser. A 308, 447.
Coey, J., Viret, M., von Molnar, S., 1999. Adv. Phys. 48, 167.
Dagotto, E., Yunoki, S., Malvezzi, A., Moreo, A., Hu, J., Capponi, S., Poilblanc, D., Furukawa, N., 1998. Phys. Rev. B 58, 6414.
Dagotto, E., Hotta, T., Moreo, A., 2001. Phys. Rep. 344, 1.

de Gennes, P., 1960. Phys. Rev. 118, 141.
Deutcher, G., 1987. In: Souletie, J., Vannimenus, J., Stora, R. (Eds.), Chance and Matter. Elsevier, Amsterdam.
Dzero, M., Gor'kov, L., Kresin, V., 1999. Solid State Commun. 112, 707.
Dzero, M., Gor'kov, L., Kresin, V., 2000. Eur. Phys. B 14, 459.
Endoh, Y., Hirota, K., 1997. J. Phys. Soc. Japan 66, 2264.
Fath, M., Freisem, S., Menovsky, A., Tomioka, Y., Aarts, J., Mydosh, J., 1999. Science 285, 1540.
Fang, Z., Solovyev, I., Terakura, K., 2000. Phys. Rev. Lett. 84, 3169.
Felner, I., Asaf, U., Levy, Y., Millo, O., 1997. Phys. Rev. B 55, 3374.
Felner, I., Tsindllkht, M., Gorodetsky, G., Rosenberg, F., 2000. J. Supercond. Novel Magn. 13, 659.
Franck, J., Isaak, I., Chen, W., Chrzanowski, J., Irwin, J., 1998. Phys. Rev. B 58, 5189.
Fukumoto, N., Mori, S., Yamamoto, N., Moritomo, Y., Katsufuji, T., Chen, C., Cheong, S., 1999. Phys. Rev. 60, 12963.
Furukawa, N., 1994. J. Phys. Soc. Japan 63, 2734.
Furukawa, N., 1995a. J. Phys. Soc. Japan 64, 1174.
Furukawa, N., 1995b. J. Phys. Soc. Japan 64, 2754.
Furukawa, N., 1996. J. Phys. Soc. Japan 65, 1174.
Gantmakher, V., Levinson, Y., 1987. Carrier Scattering in Metals and Semiconductors. North-Holland, Amsterdam, p. 139.
Ghosh, K., Lobb, C., Greene, R., Karabashev, S., Shulyater, D., Arsenov, A., Mukovskii, Y., 1998. Phys. Rev. Lett. 81, 4740.
Goldschmidt, 1958. Geochemistry, Oxford University Press, Oxford.
Goodenough, J., 1963. Magnetism and the Chemical Bond. N.Y.
Gordon, J., Marsenat, C., Franck, J., Isaak, I., Zhang, G., Lortz, R., Meingast, C., Bouquet, F., Fisher, R., Phillips, N., 2001. Phys. Rev. B 65, 024441.
Gor'kov, L., 1998. Soviet Phys. (Uspekhi) 41, 589.
Gor'kov, L., Kresin, 1998. JETP Lett. 67, 985.
Gor'kov, L., Kresin, V., 1999. Proc. Int. Conf., J. Supercond. Novel Magn. 12, 243.
Gor'kov, L., Kresin, V., 2000. J. Supercond. Novel Magn. 13, 39.
Gor'kov, L., Kresin, 2001. Appl. Phys. Lett. 78, 3657.
Gor'kov, L., Sokol, A., 1987. JETP Lett. 46, 429.
Habermeier, H., 2004. J. Supercond. Novel Magn. 17, 15.
Hamilton, J., Ktating, E., Ju, H., Raychaudhari, A., Smolyaninova, N., Greene, R., 1996. Phys. Rev. B 54, 14926.
Heffner, R., Le, P., Hundley, M., Neumeier, J., Luke, G., Kojima, K., Nachumi, B., Uemura, Y., MacLaughlin, D., Cheong, S., 1996. Phys. Rev. Lett. 77, 1869.
Heffner, R., Sonier, J., MacLauchlin, D., Nieuwenhaus, G., Ehlers, G., Mezei, F., Cheong, S., Gardner, J., Roder, H., 2000. Phys. Rev. Lett. 85, 3285.
Heffner, R., Sonier, J., MacLauchlin, D., Nieuwenhaus, Luke, G., Uemura, Y., Ratdiff, W., Cheong, S., Balakrishnan, G., 2001. Phys. Rev. B 62, 1203.
Hundley, M., Hawley, M., Heffner, R., Jia, Q., Neumeier, J., Tesmer, J., Thompson, J., Wu, X., 1995. Appl. Phys. Lett. 67, 860.
Hwang, H., Dai, P., Cheong, S., Aeppli, G., Tennant, D., Mook, H., 1998. Phys. Rev. Lett. 80, 1316.
Izumi, M., Manako, T., Konishi, Y., Kawasaki, M., Tokura, Y., 2000. Phys. Rev. B 61, 18187.
Jaime, M., Lin, P., Chun, S., Salamon, M., Dorsey, P., Rubinstein, M., 1999. Phys. Rev. 60, 1028.
Jin, S., Tiefel, T., McCormack, M., Fastnacht, R., Ramesh, R., Chen, L., 1994. Science 264, 413.
Jonner, G., Van Santen, J., 1950. Physica 16, 337.
Josephson, B., 1962. Phys. Lett. 1, 251.
Kanamori, J., 1961. J. Appl. Phys. 31 (Suppl.), 145.
Kaplan, M., Vekhter, B., 1995. Cooperative Phenomena in Jahn–Teller Crystals, Plenum Press, London.
Kawano, H., Kajimoto, R., Yoshizawa, H., Tomioka, Y., Kuwahara, H., Tokura, Y., 1997. Phys. Rev. Lett. 78, 4253.
Kirkpatrick, S., 1973a. Rev. Modern Phys. 45, 574.
Kirkpatrick, S., 1973b. Solid State Commun. 12, 1279.
Kittel, C., 1963. Quantum Theory of Solids, Wiley, NY (Chapter 4).
Kresin, V., 1986. Phys. Rev. 34, 7587.
Kresin, V., Lester Jr., W., 1984. Chem. Phys. 90, 935.
Kresin, V., Wolf, S., 1998. J. Appl. Phys. 63, 7357.
Kresin, V., Wolf, S., 1997. Philos. Mag. 76, 241.

Kugel, K., Khomskii, D., 1973. Sov. Phys. JETP 37, 725.
Kugel, K., Khomskii, D., 1982. Sov. Phys. (Usp.) 25, 231.
Kuwahara, H., Okuda, T., Tomioka, Y., Asamutsi, Y., Tokura, Y., 1999. Phys. Rev. Lett. 82, 416.
Landau, L., Lifshitz, E., 1976. Quantum Mechanics, Pergamon, NY.
Li, G., Bridges, F., Booth, C., 1995. Phys. Rev. B 52, 6332.
Lifshitz, E., Pitaevskii, L., 1989. Statistical Physics, Part 2. Pergamon Press, Oxford, p. 227.
Lifshitz, I., 1960. JETP 11, 1130.
Lofland, S., Bhagat, S., Ju, H., Xiong, G., Venkatesan, T., Green, R., 1996. J. Appl. Phys. 79, 5166.
Louca, D., Egami, T., 1997a. J. Appl. Phys. 81, 5484(1997).
Louca, D., Egami, T., 1997b. Physica B 241, 842(1997).
Louca, D., Egami, T., 1999a. Phys. Rev. B 59, 6193.
Louca, D., Egami, T., 1999b. J. Supercond. 12, 23.
Lynn, J., Erwin, R., Borchers, J., Santoro, A., Huang, Q., 1996. Phys. Rev. Lett. 76, 4046.
Mahendiran, R., Ibarra, M., Maignan, A., Millange, F., Arulraj, A., Mahesh, R., Raveau, B., Rao, C., 1999. Phys. Rev. Lett. 82, 2191.
Mannella, N., Rosenhahn, A., Booth, C., Marchesini, S., Mun, B., Yang, S., Ibrahim, K., Tomioka, Y., Fadley, C., 2004. Phys. Rev. Lett. 92, 166401.
Martin, M., Shirane, G., Endoh, Y., Hirota, K., Marimoto, Y., Tokura, Y., 1996. Phys. Rev. B 53, 14285.
Millis, A., Littlewood, P., Shraiman, B., 1995. Phys. Rev. Lett. 74, 5144.
Millis, A., Shraiman, B., Mueller, R., 1996a. Phys. Rev. Lett. 77, 175.
Millis, A., Shraiman, B., Mueller, R., 1996b. Phys. Rev. B 54, 5389.
Millis, A., 1998. Nature 392, 147.
Moreo, A., Yunoki, S., Dagotto, E., 1999. Science 283, 2034.
Mori, S., Chen, C., Cheong, S., 1998. Phys. Rev. Lett. 81, 3972.
Moudden, A., Vasiliu-Doloc, L., Pinsard, L., Revcolevschi, A., 1998. Physica B 241–243, 276.
Nagaev, E., 1994. Phys. Stat. Sol. B 186, 9.
Nagaev, E., 1996. Phys. (Uspechi) 39, 781.
O'Malley, T., 1967. Phys. Rev. 152, 98.
Okimoto, Y., Tokura, Y., 2000. J. Supercond. Novel Magn. 13 (Special issue), 271.
Okuda, T., Asamitsu, A., Tomioka, Y., Kimura, T., Taguchi, Y., Tokura, Y., 1998. Phys. Rev. Lett. 81, 3203.
Parkin, P., 1995. Annu. Rev. Mater. Sci. 25, 357.
Perring, T., Aeppli, G., Hayden, S., Carter, S., Remeika, J., Cheong, S., 1996. Phys. Rev. Lett. 77, 711.
Pickett, W., Singh, S., 1996. Phys. Rev. B 53, 1146.
Prodi, A., Giliali, A., Gauzzi, A., Licei, F., Marezio, M., Bolzoni, F., Huang, Q., Santovo, A., Lynn, J., 2004. Nature Mat. 3, 48.
Quijada, M., Cerne, J., Simpson, J., Drew, H., Ahn, K., Millis, A., Shreekala, R., Ramesh, R., Rajeswari, M., Venkatesan, T., 1998. Phys. Rev. B 58, 16093.
Ramirez, A., 1997. J. Phys. Cond. Matter 9, 8171.
Ramirez, A., Schiffer, P., Cheong, S., Chen, C., Bao, W., Palstra, T., Gammel, P., Bishop, D., Zegarski, B., 1996. Phys. Rev. Lett. 76, 3188.
Rashba, E., 1982. In: Rashba, E., Sturge, M. (Eds.), Excitons. North-Holland, Amsterdam, p. 473.
Scher, H., Zallen, R., 1970. J. Chem. Phys. 53, 3759.
Schiffer, P., Ramirez, A., Bao, W., Cheong, S., 1995. Phys. Rev. Lett. 75, 1995.
Shibata, T., Bunker, B., Mitchell, J., 2003. Phys. Rev. B 68, 024103.
Shklovskii, B., Efros, A., 1984. Electronic Properties of Doped Semiconductors, Springer, Berlin.
Sigmund, E., Mueller, K. (Eds.), 1994. Phase Separation in Cuprate Superconductors. Springer-Verlag, Berlin.
Stuffer, D., Aharony, A., 1992. Introduction to Percolation Theory, Taylor and Francis, London.
Subias, G., Garsia, J., Proietti, M., Blasko, J., 1997. Phys. Rev. B 36, 8183.
Takahashi, A., Shiba, H., 1998. Eur. Phys. J. B 5, 413.
Tinkham, M., 1996. Introduction to Superconductivity, McGraw-Hill, NY.
Tokunaga, M., Miura, N., Tomioka, Y., Tokura, Y., 1998. Phys. Rev. B 57, 5259.
Tokura, Y., Kuwahara, H., Moritomo, Y., Tomioka, Y., Asamutsu, A., 1996. Phys. Rev. Lett. 76, 3184.
Tokura, Y., Tomioka, Y., 1999. J. Magn. Magn. Mater. 200, 1.

Tokura, Y., Urushibara, A., Moritomo, Y., Arima, T., Asamitsu, A., Kido, G., Furukawa, N., 1994. J. Phys. Soc. Japan 63, 3931.
Tokura, Y., 2003. Phys. Today 56, 50.
Tomioka, Y., Asamitsu, A., Moritomo, Y., Kuwahara, H., Tokura, Y., 1995. Phys. Rev. Lett. 74, 5108.
Toyozawa, Y., Shinozuka, Y., 1983. J. Phys. Soc. Japan 52, 1446.
Uehara, M., Mori, S., Chen, S., Cheong, S., 1999. Nature 399, 560.
Urushibara, A., Moritomo, Y., Arima, T., Asamitsu, A., Kido, G., Tokura, Y., 1995. Phys. Rev. B 51, 14103.
van der Brink, J., Khomskii, D., 1999. Phys. Rev. Lett. 82, 1018.
Vasiliu-Doloc, L., Lynn, J., Mukovskii, Y., Arsenov, A., Shulyatev, D., 1997. J. Appl. Phys. 81, 5491.
Viret, D.M., Ranno, L., Coey, J., 1997. Phys. Rev. B 55, 8067.
Volger, J., 1954. Physica 20, 49.
von Helmholt, R., Wecker, J., Holzarefl, B., Schultz, L., Samwer, K., 1993.
Weiße, A., Jan Loos, T., Fehske, H., 2003. Phys. Rev. B 68, 024402.
Yunoki, S., Moreo, A., Dagotto, E., 1998a. Phys. Rev. Lett. 81, 5612.
Yunoki, S., Hu, J., Malvezzi, A., Moreo, A., Furukawa, N., Dagotto, E., 1998b. Phys. Rev. Lett. 80, 845.
Yunoki, S., Moreo, A., 1998. Phys. Rev. B 58, 6403.
Zener, C., 1951a. Phys. Rev. 81, 440.
Zener, C., 1951b. Phys. Rev. 82, 403.
Ziman, J., 1960. Electrons and Phonons, Oxford University Press, Oxford.